UNIVERSITÀ DEGLI STUDI DI TRIESTE

XXIX CICLO DEL DOTTORATO DI RICERCA IN FISICA

Probing the physical and chemical state of the Intergalactic Medium with hydrodynamical simulations

SETTORE SCIENTIFICO-DISCIPLINARE: FIS/05

Coordinatore:

PROF. LIVIO LANCERI

Supervisore:

DR. MATTEO VIEL

Dottoranda:

CHIARA MONGARDI

Co-Supervisore:

DR. VALENTINA D'ODORICO

Co-Supervisore:

PROF. STEFANO BORGANI

Anno Accademico 2015/16

Contents

Chapter 1

Introduction

The currently accepted cosmological theory is the ΛCDM model. Λ is the cosmological constant, associated with dark energy, that represents ∼70 % of the estimated mass/energy density of the Universe and that was introduced in order to explain the accelerated expansion of the Universe, as first probed by observations of high-z SNIa. Dark energy is one of the most interesting issues in modern physics; its nature is still obscure and a deep revision of the laws of physics could be needed to explain it. CDM stands for "Cold Dark Matter ", a form of matter necessary to account for observed gravitational effects (e.g., galaxy's rotation curves, gravitational lensing in galaxy clusters), that is a fundamental ingredient in the formation of large-scale structures, as we observe them today. It is described as being cold, meaning that its velocity is non-relativistic at the epoch of radiation-matter equality, dissipationless and collisionless and it forms ∼25 % of the cosmic mass/energy density. Despite the nature of this component remains unclear and experiments are still going on for its detection, its existence is generally accepted by most of the astronomical community. The budget of the cosmic mass/energy density is completed by a ∼5 % of baryonic matter, which forms the "visible"Universe.
The ΛCDM model is based upon the cosmological principle, that states that the Universe is spatially homogeneous and isotropic and so our position is not special or different from any other, and upon the Einstein's theory of General Relativity. The cosmological principle is considered to be valid on large scales ($\gtrsim$ 100 Mpc), while at small scales the Universe is strongly inhomogeneous, formed by stars, planets, galaxies, etc., which are not uniformly distributed.
The formation of structures is due to gravitational instability of primordial density fluctuations which grow through Jeans instability. These primordial fluctuations are the results of quantuum fluctuations which were magnified to cosmic scales during

the epoch of inflation. In our expanding Universe, overdensity perturbations initially grow in size with time, as the Universe expands. When an overdensity exceeds a given threshold ($\delta\rho/\rho \sim 1$) with respect to the background, the region within the density peak decouples from the expanding flow and starts to collapse, becoming a gravitationally self-bound structure.

Dark matter drives the perturbation growth and after the baryonic matter decouples from radiation, baryons start to fall into the growing potential wells of dark matter. A fundamental ingredient for galaxy formation is, then, gas cooling. Once the gas has virialized in dark matter halos, it starts to cool and to collapse and, at this point, star formation begins and the first stars and protogalaxies form. The gas that fills the space between galaxies, instead, is the so-called Intergalactic Medium (IGM), which results as a "Cosmic Web"of filaments and sheets, as derived from numerical simulations. This component has too low densities to be probed in emission, but it can be observed through absorption lines in the spectra of luminous background sources.

The described model is widely accepted as it can explain many properties of the Universe, such as its expansion, the distribution of large-scales structures, the primordial abundance of light elements and the Cosmic Microwave Background (CMB). The latter was a prediction of the model and its accidental discovery in 1965 by Penzias and Wilson (1965) was a key confirmation of its validity.

The fundamental parameters of the ΛCDM model (Ω_m,Ω_Λ,Ω_k,$w(z)$,h,σ_8,n_s)[1] are constrained by observations with great accuracy (e.g., Planck Collaboration). On the other hand, there are still significant uncertainties related to galaxy formation and evolution and to the modeling of the baryon's physical processes. In this context, the study of the IGM and of its evolution is of great relevance. First of all, the IGM is the reservoir of baryons from which galaxies form and it is the fuel necessary for sustaining star formation, while at the same time it is being replenished with both newly accreted intergalactic gas and chemically enriched materials from galaxies, carrying the imprints of galactic feedback. Therefore, intergalactic space provides a critical laboratory to investigate the baryon cycle that regulates star formation and galaxy growth.

In particular, IGM metal enrichment has gained a lot of interest after the second half of the '90s. In fact, it was originally thought that the gas infalling onto galaxies had a primordial composition, as heavy elements can be produced only inside stars

[1]They represent the matter density parameter, dark energy density parameter, curvature density parameter,equation of state parameter, Hubble parameter in units of 100 km s^{-1} Mpc^{-1},density perturbation amplitude on 8 h^{-1} Mpc scales, density perturbation spectral index, respectively.

and star formation is not present in the low-density and high-temperature IGM. With the advent of high-resolution spectroscopy around 1995, the first metal absorption lines were observed in Quasars (QSOs) spectra, leading to the question of the mechanisms polluting the IGM.
In order to study the baryon cycle in galaxies several observational studies have been carried out correlating absorption lines in QSO spectra with the position and redshift of galaxies in the same field both at high (e.g. Adelberger et al., 2005; Steidel et al., 2010; Turner et al., 2014) and low redshift (e.g. Prochaska et al. 2011; Tumlinson et al. 2011; Werk et al 2013; Bordoloi et al. 2014; Liang & Chen 2014). In particular at high redshift, this approach is limited by the difficulties in detecting and characterizing all the galaxies closer to the line of sight, resulting in a sparse picture of the circumgalactic medium (CGM) and of the true origin of absorbers.

In this thesis work, I tried to characterise the properties of the IGM around galaxies at high redshift using hydrodynamical simulations compared with observational data taken from the literature. In particular, with my research I have shed some light on the nature of the environment that give rise to the observed metal systems (in particular systems identified by the C IV and Si IV transitions) and at the same time I have found that some of the subgrid physical processes implemented in simulations do not have a substantial influence on the characteristics of the IGM.
In the following I give a summary of the content of the different chapters of my thesis:

- **Chapter 2**: in this Chapter, I review some of the theory behind line formation and its structure, given by the Voigt profile. As the IGM is probed by absorption features, I describe also some of the observational techniques used to derive physical gas parameters, such as its density or temperature, from line profiles. In particular, I describe the methods of the curve of growth, Voigt Profile Fitting and Apparent Optical Depth. I give also a brief summary of the classification of QSO absorption lines.

- **Chapter 3**: in this Chapter, the main characteristics of the IGM are introduced. First, some observational features are described, such as the Gunn-Peterson test, the column density or Doppler parameter b distributions of absorption feature and their number evolution. Also physical sizes and clustering of the absorbers are discussed. Then, I discuss the early models of the IGM and how the Lyα forest is described in hierarchical models. Then, I talk

about the statistics of the transmitted flux, the UV Background, responsible of ionizing the IGM, and, finally, I face the problem of the IGM metal enrichment.

- **Chapter 4**: in this Chapter, I introduce cosmological simulations and describe the principal methods and recipes used in N-body and hydrodynamic simulations for the modeling of dark matter and baryon evolution. Then, I describe the simulations used in this thesis work, which are characterized by two different subresolution model, the MUPPI model and the Effective model.

- **Chapter 5**: in this Chapter, I report the results of this thesis work, concerning a study of a sample of simulated galaxies and the gas environments around them, taken from the two different simulations, and also a sample of selected near-filament environments, in order to probe the low density gas. Using lines of sight, obtained by piercing through the cosmological box lines around each object, I studied the N_{HI} vs N_{CIV} relation at different distances from galaxies, which I compared to observational data. Furthermore, I also analysed the covering fractions as a function of the equivalent width for the sample of lines of sight around galaxies, which I compared with data taken from the literature, and I constructed new covering fractions as a function of column density of the absorption systems, which can be used to compare with future high-resolution data. I also tried to better investigate the differences in the two simulations by analysing other chemical elements, such as O VI and Si IV. Finally, I performed a comparison between column densities derived with Voigt Profile Fitting codes, the standard observational procedure for deriving physical gas quantities in a regime of high resolution spectroscopy, and the ones derived directly from the simulation and I addressed some considerations about the best method to use when comparing with observational data.

- **Chapter 6**: in this Chapter, I summarize the main results of this work, draw some conclusions and give some future perspectives.

Chapter 2

Quasar Absorption Lines

The intergalactic medium is typically probed through absorption features observed in the spectra of background luminous sources, mainly QSOs. In fact, its very low densities make it extremely difficult to detect it in emission.
In Fig. 2.1, a typical QSO spectrum is shown. The strong emission line at $\lambda \sim 4900$ Å is the H I Lyman-α (Lyα) emission line redshifted at the systemic redshift of the QSO. The absorption lines blueward of the Lyα emission line are absorption features due mainly to Hydrogen atoms in the ground state in intervening gas clouds along the line of sight (Gunn and Peterson, 1965; Bahcall and Salpeter, 1965; Burbidge et al., 1966; Lynds, 1971; Oemler and Lynds, 1975; Young et al., 1979). In fact, as the QSO light travels towards the observer, high energies photons are redshifted to the resonance energy of the Lyα and are absorbed by intervening gas clouds leaving their fingerprints at different positions in the QSO spectrum and resulting as a $forest$ of lines (Lynds, 1971).
The number of lines increases going to higher redshifts, as the light of the QSO has to pass through denser and more neutral gas. The intergalactic medium is considered to be clumpy; the absence of a spatially smooth component is proved by the absence of a Gunn-Peterson effect (Gunn and Peterson, 1965, see Section 3.1) at least at z <6 when the Universe is considered to be fully ionized.
Absorption lines redward of the Lyα QSO emission line are due to transitions in heavier chemical elements (dubbed metals) and their abundances in the clouds can also be studied.

Studying these absorption features can provide a lot of information regarding the physical and chemical state of the gas that produced the absorption. They can also be used as cosmological probes (Ostriker and Vishniac, 1986; Rees, 1986; Efstathiou, 1992; Thoul and Weinberg, 1996; Hu, 2000; Viel et al., 2005; Seljak et al., 2005; Kereš

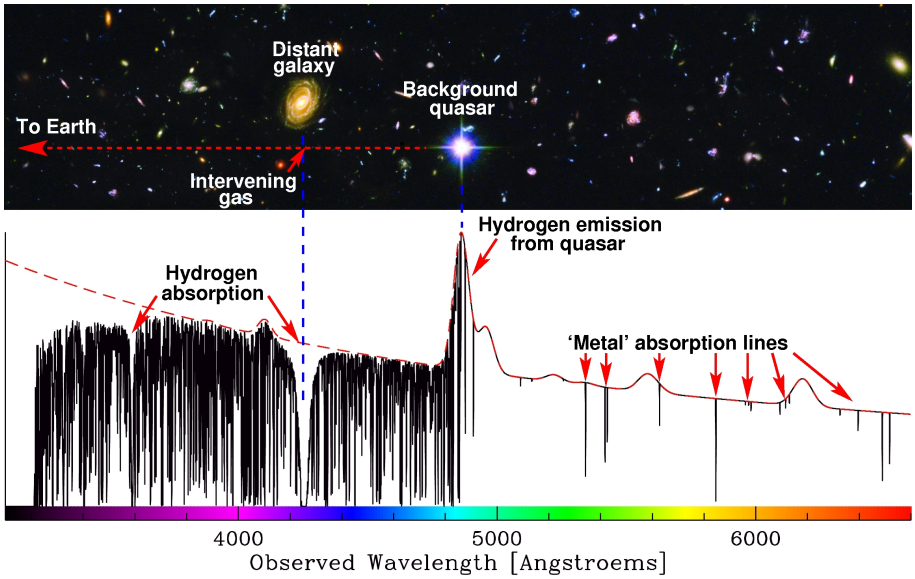

Figure 2.1: Qualitative representation of a typical QSO spectrum. At $\sim$ 4900 Å, the Lyα emission line of the QSO is represented. Blueward and redward of this emission line, absorption lines due to intervening gas clouds are superimposed to the QSO continuum (red line). Figure taken from http://www.hs.uni-hamburg.de/jliske/qsoal/.

et al., 2005; Pritchard et al., 2007; Wyithe and Dijkstra, 2011).
The production of absorption features is governed by the equations of radiative transfer.
In this chapter, I will describe the theory behind the formation of absorption lines and their structure and I will review some of the observational techniques, used to derive physical parameters from the observed features.

2.1 Radiative Transfer

In this Section, I will recall some of the general definitions and equations related to the propagation of electromagnetic radiation in a medium, which for simplicity I will generally refer to as a "cloud ".
If we define:
- ε_ν: the emissivity coefficient;
-I_ν: the radiation intensity;
-k_ν: the absorption coefficient;
then, the intensity of the radiation within a solid angle $d\omega$ will change by an amount dI_ν along the spatial distance ds given by the formula:

$$dI_\nu d\omega = \varepsilon_\nu d\omega ds - k_\nu I_\nu d\omega ds \tag{2.1}$$

The equation can be rewritten as:

$$\frac{dI_\nu}{d\tau_\nu} = -I_\nu + \frac{\varepsilon_\nu}{k_\nu} \tag{2.2}$$

$$\frac{dI_\nu}{d\tau_\nu} = -I_\nu + S_\nu \tag{2.3}$$

where $d\tau_\nu = k_\nu ds$ is the optical depth and $S_\nu = \frac{\varepsilon_\nu}{k_\nu}$ is the source function, which is characteristic of the cloud.
Integrating Eq.2.3, we obtain:

$$I_\nu = S_\nu[1 - e^{-\tau_\nu}] + I_{\nu,0}e^{-\tau_\nu} \tag{2.4}$$

where $\tau_\nu = k_\nu L$ is the optical depth of the entire cloud, having a spatial length L, and $I_{\nu,0}$ is the background radiation before passing through the cloud.
The limiting cases are:

$$\begin{aligned} I_\nu &= \tau_\nu(S_\nu - I_{\nu,0}) + I_{\nu,0} \quad , for \quad \tau_\nu \ll 1 \\ &= S_\nu \quad , for \quad \tau_\nu \gg 1 \end{aligned} \tag{2.5}$$

When $\tau_\nu \ll 1$, we observe the intensity of the background source of radiation attenuated $[I_{\nu,0}(1 - \tau_\nu)]$, plus the contribution of the cloud itself ($\tau_\nu S_\nu = \varepsilon_\nu L$); when $\tau_\nu \gg 1$, we do not receive anything from the background source and we observe only the intrinsic emission of the cloud.
I discuss now the particular case of emission/absorption in a line, meaning that the cloud has emission/absorption only at a given frequency ν_0. Consequently, the photons of a background source will be absorbed only at ν_0, while for $\nu \neq \nu_0$ the cloud is completely transparent to them.
The condition for having an emission line is $I_\nu - I_{\nu,0} > 0$ (where we assume $\nu = \nu_0$); the opposite for an absorption line. Thus the condition can be expressed as:

$$[I_{\nu,0}e^{-\tau_\nu}] + [S_\nu(1 - e^{-\tau_\nu})] - I_{\nu,0} = (S_\nu - I_{\nu,0})(1 - e^{-\tau_\nu}) \lessgtr 0 \tag{2.6}$$

For $\tau_\nu = 0$ there is no line. From Eq.2.6 we can conclude that, even if τ_ν is very small, if $I_{\nu,0}$ is sufficiently strong, the absorption can be measured, while having a strong emission line requires high values of S_ν. For this reason, in the case of a tenuous medium the observation of absorption lines is much easier than in emission: it is sufficient that the cloud is projected on a very bright source, while for the emission,

the source function must be greater than the intensity of the background source. As previously said, the densities of the intergalactic medium are so low ($\sim 10^{-4}$ cm^{-3}), that the term S_ν can actually be neglected and Eq.2.4 becomes:

$$I_\nu = I_{\nu,0} e^{-\tau_\nu} \tag{2.7}$$

More precisely, we integrate the radiation of a source using a telescope with an aperture A, so the quantity that we actually measure is the flux density F_ν:

$$F_\nu = F_{\nu,0} e^{-\tau_\nu} \tag{2.8}$$

2.2 Line Broadening and Voigt Profile

Spectral lines are not infinitely sharp and narrow, but they are somewhat broadened. There are different processes that contribute to the observed line profile.

Natural broadening. Spectral lines have a *natural* width, which is generally very small, due to the Heisenberg uncertainty principle. According to quantum mechanics, the energy of an atomic level and its lifetime cannot be measured with great accuracy simultaneously:

$$\Delta E \Delta t \approx \hbar \tag{2.9}$$

Short-lived states have relatively larger uncertainties in the energy. If the average lifetime of an excitation state is T, the frequency of the emitted photon will be:

$$\Delta\nu \sim \frac{\Delta E}{h} \sim \frac{1}{2\pi T} \tag{2.10}$$

If the spontaneous decay of an atomic state n proceeds with a probability given by $\gamma = \sum_{m<n} A_{nm}$, where A_{nm} are the Einstein coefficients, then it can be shown that the emitted photons will not have a monochromatic frequency ν_{nm}, like a Dirac delta function, but a distribution of frequencies that can be described by a function $\phi(\nu)$, peaked at the frequency ν_{nm}, given by this formula:

$$\phi(\nu) = \frac{\gamma/4\pi^2}{(\nu - \nu_{nm})^2 + (\gamma/4\pi)^2} \tag{2.11}$$

This is called a *Lorentzian* or natural line profile.
Other processes broaden the line profile more than the natural width, such as the collisional and the thermal broadening, and which have a greater importance on the

final resulting line profile.

Collisional broadening. The collisional decay is caused by collisions with other particles (electrons, atoms, molecules,...). The importance of this effect depends on the frequency of collisions ν_{col} and on the gas density. The effect of collision is to shorten the lifetime of an atomic state to a value smaller than the natural quantum mechanical lifetime.
The profile of the broadened line is still a *Lorentzian* profile:

$$\phi(\nu) = \frac{\Gamma/4\pi^2}{(\nu - \nu_{nm})^2 + (\Gamma/4\pi)^2} \tag{2.12}$$

but with:

$$\Gamma = \gamma + 2\nu_{col} \tag{2.13}$$

Thermal broadening. Atoms in a gas have random motions which depend on the gas temperature. For particles with mass m and a gas temperature T, the most probable speed is given by:

$$\frac{1}{2}mv^2 = k_B T \tag{2.14}$$

with k_B being the Boltzmann constant. The velocity distribution of the gas particles is generally assumed to be described by a Maxwellian law. Each atom produces its line profile which is Doppler shifted according to its velocity. The resulting line profile is the collection of different line profiles with different Doppler shifts.
If the velocity of a particle is $v^2 = v_x^2 + v_y^2 + v_z^2$, we are interested in the velocity distribution of only one component, as random motions along the line of sight are relevant.
For one component, the number of atoms dN within a velocity interval dv_x is:

$$dN(v_x) \propto e^{-\frac{mv_x^2}{2k_B T}} dv_x \tag{2.15}$$

peaked at the value $v_{\text{peak}} = \sqrt{2k_B T/m}$. The 3D velocity distribution has an extra factor v^2.
Combining the velocity distribution of Eq.2.15 with the Doppler shift formula $(\nu - \nu_0)/(\nu_0) = v_x/c$, the line profile is given by:

$$\phi(\nu) = \frac{1}{\Delta\nu_D\sqrt{\pi}} e^{-\frac{(\nu-\nu_0)^2}{(\Delta\nu_D)^2}} \tag{2.16}$$

$\Delta\nu_D$ is the Doppler width of the line and is defined as:

$$\Delta\nu_D = \frac{\nu_0}{c}\sqrt{\frac{2k_BT}{m}} = \frac{\nu_0}{c}b_{\rm th} \tag{2.17}$$

where ν_0 is the frequency of the line center and $b_{\rm th}$ is the so-called Doppler parameter.
In some physical situations, the gas can experience also bulk motions due to turbulence, which are described by the same velocity distribution. This can be taken into account by adding a term $v_{\rm turb}$ to the thermal velocity and define an $effective\ Doppler\ width$:

$$\Delta\nu_D = \frac{\nu_0}{c}\sqrt{\frac{2k_BT}{m} + v_{\rm turb}^2} \tag{2.18}$$

The thermal line profile is described by a *Gaussian* function, which falls off very rapidly from the line center.

The three broadening mechanisms affect the line shape simultaneously, so the resulting line is a combination of the different profiles. The convolution of a Lorentzian profile with a Gaussian one is called the ***Voigt profile***:

$$\phi(\nu) = \frac{\Gamma}{4\pi^2}\sqrt{\frac{m}{2\pi k_BT}}\int_{-\infty}^{\infty}\frac{e^{-\frac{mv_x^2}{2k_BT}}}{(\nu-\nu_0-\nu_0v_x/c)^2+(\Gamma/4\pi)^2}dv_x \tag{2.19}$$

also expressed as:

$$\phi(\nu) = \frac{1}{\Delta\nu_D\sqrt{\pi}}H(a,x) \tag{2.20}$$

$H(a,x)$ is the *Hjerting function*:

$$H(a,x) = \frac{a}{\pi}\int_{-\infty}^{\infty}\frac{e^{-y^2}}{a^2+(x-y)^2}dy \tag{2.21}$$

where

$$a = \frac{\Gamma}{4\pi\Delta\nu_D} \quad , \quad x = \frac{\nu-\nu_0}{\Delta\nu_D} \tag{2.22}$$

The cross-section for the absorption is given by:

$$\sigma_\nu = \sigma_{\nu,0}H(a,x) \quad with \quad \sigma_{\nu,0} = \frac{\sqrt{\pi}e^2}{m_ec}\frac{f}{\Delta\nu_D} \tag{2.23}$$

where f is the oscillator strength.

As shown in Fig.2.2, the Gaussian profile dominates in the core of the line, while

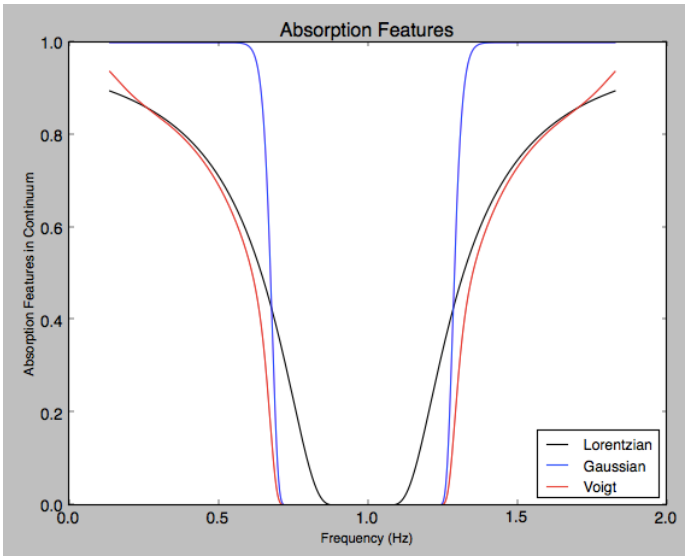

Figure 2.2: Gaussian and Lorentzian (or damping) contribution to the line profile. The Gaussian curve dominates in the center of the line, while the damping one in the wings. The Voigt profile is the convolution of these two function. Figure taken from https : //casper.berkeley.edu/astrobaki/index.php/Line_Profile_Functions .

the Lorentzian profile dominates in the wings.
The optical depth can be also expressed as $\tau_\nu = k_\nu L = \sigma_\nu n L = \sigma_\nu N$, where n is the volume density of the absorbing cloud and N is the column density. The column density is the number of absorbing atoms in a column of unit cross section in the direction of the observer. From Eq.2.23, it is possible to derive:

$$\tau_\nu = N \frac{\sqrt{\pi} e^2}{m_e c} \frac{f}{\Delta\nu_D} H(a,x) = \tau_{\nu,0} H(a,x) \tag{2.24}$$

where $\tau_{\nu,0}$ is the optical depth at the center of the line.
Fig.2.3 shows how the absorbing line profile changes by varying the temperature T and column density N of the absorbing gas. As the T increases, $\tau_{\nu,0}$ decreases and the line becomes broader. For an increasing N instead, $\tau_{\nu,0}$ increases and the line becomes deeper, until it becomes completely opaque in the center ($F_{\nu,0} = 0$); at this point, the contribution of the wings of the line profile is negligible and augmenting the number of absorbing atoms does not increase significantly the line width. The line is said to be *saturated*.
If N further increases, the contribution of the wings becomes important and the line profile becomes broader.
I will better discuss this issue in Section 2.3.

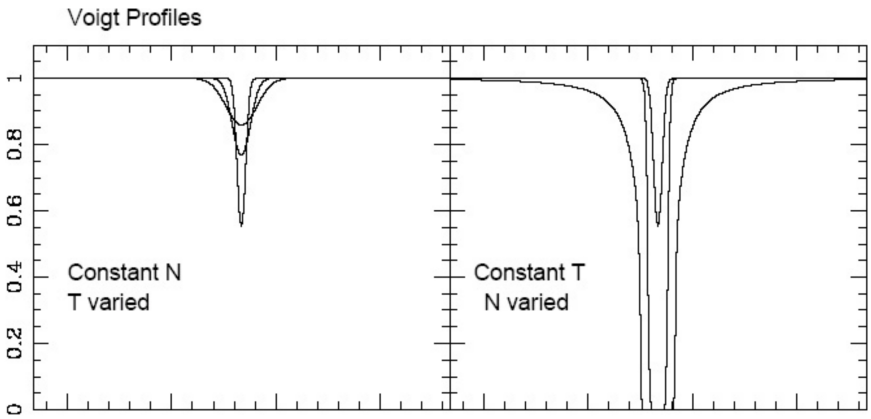

Figure 2.3: Line profiles as temperature T or column density N of the absorbing gas is changed. (Courtesy of Prof. S. Cristiani).

2.3 Equivalent Width

In a regime of low spectral resolution, when it is not possible to resolve properly the line profile, it can be useful to measure the equivalent width of the line.
The equivalent width is by definition the width of a rectangle with a unitary height and area equal to the one subtended by the spectral line with respect to the continuum. Its definition is given by the formula:

$$W(\lambda) = \int \left(1 - \frac{F_\lambda}{F_{\lambda,0}}\right) d\lambda \tag{2.25}$$

where F_λ is the observed flux in the wavelength range of the absorption and $F_{\lambda,0}$ is the continuum level.
The observed equivalent width W_{obs} is related to the rest-frame one W_r by the formula $W_{obs} = W_r(1 + z)$.
Increasing the number of absorbing atoms, the line profile changes, as already described in Section 2.2. To summarize, there are three regimes, listed according to an increasing absorber column density:

- Linear regime: the line is optically thin at every wavelength;

- Saturated regime: the line becomes optically thick in the center and, as the flux in the core cannot be less than zero, the line becomes saturated. The Voigt profile is dominated by the Doppler one;

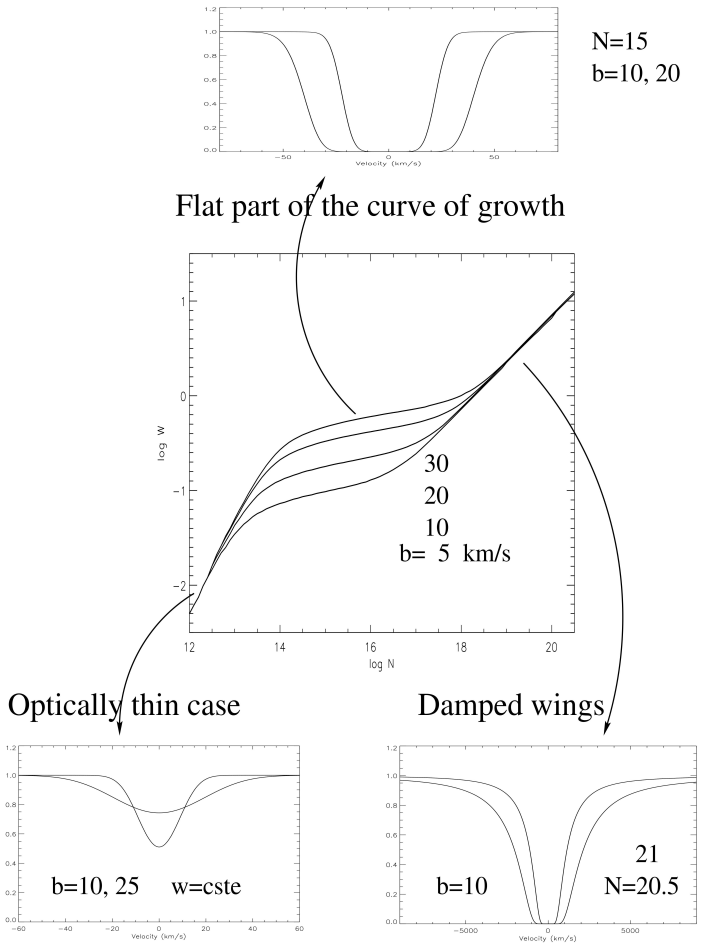

Figure 2.4: In the central panel, it represented the curve of growth for H I Lyα1215 for different values of Doppler parameter $b_{\rm th}$. The three different regimes are represented with their corresponding line profiles, as described in the text. The figure is taken from Petitjean (1998).

- Damped regime: the line becomes saturated also in the wings and the Voigt profile is dominated by the Lorentzian one.

This behaviour is shown in Fig.2.4 .

The *curve of growth* is a relation between the equivalent width and the number of absorbing atoms, expressed in column density.
In the different regimes of the curve of growth, the equivalent width has these dependences:

- linear regime, $W \propto$ N. When the line is optically thin, increasing the column

density produces a linear increase in the equivalent width. The line profile is dominated by the core contribution (Doppler broadening) and W does not depend on $b_{\rm th}$.

- saturated regime, $W \propto \sqrt{\ln \mathrm{N}}$. The equivalent width grows very slowly with N, as the line core is saturated. The contribution of the wings is still negligible and W is sensitive to $b_{\rm th}$.

- damped regime, $W \propto \sqrt{\mathrm{N}}$. The equivalent width is again sensitive to N and its increase is due to the wings, which become broader due to collisions between particles.

For these reasons, physical information about the absorbing gas can be extrapolated by constructing the curve of growth, especially when different lines of the same ion are available. In fact, column densities can be derived directly from the curve of growth, if not in the saturated regime. In the presence of a multiplet, with one line in the saturated regime and the other in the linear one, for example, constraints also on $b_{\rm th}$ (temperature), can be extrapolated.

2.4 Voigt Profile Fitting

For low resolution data, the equivalent width is the unique tool in order to gain some information on the gas physical state.
In a regime of high resolution, (FWHM < 25 km s^{-1}), where typical Lyα lines are well resolved, the line shapes are found to be approximated by Voigt profile.
The Voigt profile cannot be solved analytically, but there are different fitting codes, available to the users, which can solve the profile numerically, such as VPFIT (Carswell and Webb, 2014) or FITLYMAN (Fontana and Ballester, 1995).
The standard approach to Voigt profile Fitting (Webb, 1987; Carswell et al., 1987) is based on a decomposition of the spectrum into as many single Voigt profile components as are necessary to minimise the χ^2 and to make the χ^2 probability consistent with random fluctuations. The observable quantities derived by the fit are basically the column density, the Doppler parameter and the redshift of each Voigt component.
For saturated lines, higher order transitions can be fitted simultaneously in order to

provide additional constraints. Given enough spectral resolution and assuming that Lyα clouds are discrete entities, the profile fitting technique is the most meaningful method for extracting information from the spectra. As described in Section 2.2, if the gas particles have a Gaussian velocity distribution function, due to thermal motions plus any contribution from turbulence, line shapes are well described by the Voigt profile. Unfortunately, in more realistic cases, there can be density or velocity gradients that can invalidate the assumptions of the Voigt profile fitting. For this reason, derived parameters can have less immediate physical meaning. Possible sources of non-thermal distortions are rotational motions, gravitational collapse or galactic outflows, which have been discussed in terms of the likely line shape they produce (Weisheit, 1978; Prochaska and Wolfe, 1997; McGill, 1990; Meiksin, 1994; Rauch et al., 1996; Fransson and Epstein, 1982; Wang, 1995), but the applications of these studies have proven difficult because of the lack of realistic prototypical models for the actual line formation.
Non-Voigt profiles can still be fitted by single Voigt components and the information about nonthermal motions is encoded in the spatial correlations between individual profiles (Rauch et al., 1996).

2.5 Apparent Optical Depth (AOD) Method

The Apparent Optical Depth (AOD) method (Savage and Sembach, 1991; Sembach and Savage, 1992) is another technique which allows the user to derive column densities from absorption systems. It has gained popularity as it is a quick and reliable method for measurements in a regime of unsaturated absorption profiles, without requiring the prior knowledge of the component structure. This is very important when dealing with low resolution data.
Consider an absorption line having an optical depth $\tau(\lambda)$; in the spectrum it will appear as:

$$F(\lambda) = F_0(\lambda)e^{-\tau(\lambda)} \tag{2.26}$$

where F and F_0 are the observed flux and the continuum flux respectively.
The absorption feature is actually measured with an instrument, which has its own response $\phi_I(\Delta\lambda)$. The actual observed spectrum is a convolution between the intrinsic spectrum and the instrumental response:

$$F_{obs}(\lambda) = (F_0 e^{-\tau(\lambda)}) \otimes \phi_I(\Delta\lambda) \tag{2.27}$$

which can be rewritten as:

$$F_{obs}(\lambda) = F_0[e^{-\tau(\lambda)} \otimes \phi_I(\Delta\lambda)] \tag{2.28}$$

as the intensity of the continuum F_0 is expected to change very slowly over the spectral width of the instrumental response.
From Eq.2.26 and 2.28 it is possible to define:

$$\tau(\lambda) = \ln\left(\frac{F_0(\lambda)}{F(\lambda)}\right) \tag{2.29}$$

and

$$\tau_a(\lambda) = \ln\left(\frac{F_0(\lambda)}{F_{obs}(\lambda)}\right) \tag{2.30}$$

$\tau(\lambda)$ is the *true* optical depth, as determined from the true line profile; $\tau_a(\lambda)$ is the so-called *apparent* optical depth, which is a blurred version of the true one.
From Eq.2.28 and 2.30, we can rewrite:

$$\tau_a(\lambda) = \ln\left(\frac{1}{e^{-\tau(\lambda)} \otimes \phi_I(\Delta\lambda)}\right) \tag{2.31}$$

For $\tau(\lambda) \ll 1$, the equation is equal to $\tau_a(\lambda) = \tau(\lambda) \otimes \phi_I(\Delta\lambda)$. If the spectral resolution is high compared to the line width, that is FWHM[line] $\gg$ FWHM[ϕ_I], then $\tau_a(\lambda) \approx \tau(\lambda)$, as long as the measurements have high S/N and the continuum level is well defined.
Note that, in the cores of strong absorption lines, if the flux is very small, there will be great uncertainties in the measure of the optical depth; for this reason, this method becomes not reliable in presence of a saturated line, because it is impossible to recover the real optical depth that produced a flux equal to zero.
The AOD method relies on the connection between the optical depth and the column density, as described in Eq. 2.24.
If we consider a velocity-resolved flux profile, then we can write:

$$\tau(v) = \frac{\pi e^2}{m_e c} f\lambda N(v) = 2.654 \times 10^{-15} f\lambda N(v) \tag{2.32}$$

where λ is in Angstroms and $N(v)$ is in atoms cm^{-2} (km s^{-1})$^{-1}$.
The total column density of the absorption feature is given by solving Eq. 2.32 for the $N(v)$ and integrating along the velocity range of the absorption line:

$$N = \int N(v)dv = \frac{m_e c}{\pi e^2 f\lambda} \int \tau(v)dv = \frac{m_e c}{\pi e^2 f\lambda} \int \ln\frac{F_0(v)}{F(v)}dv \tag{2.33}$$

This method requires no prior assumption on the velocity distribution of the gas, unlike other methods.
It is possible to rewrite Eq. 2.32 and 2.33 in this way:

$$\log[N_a(v)] = \log \tau_a(v) - \log(f\lambda) + 14.576 \tag{2.34}$$

and

$$N_a = \int_{v_-}^{v_+} N_a(v)dv \tag{2.35}$$

where v_- and v_+ are the velocity limits of the absorption line.
As $\tau_a(v)$ is the instrumental blurred version of $\tau(v)$, in the same way $N_a(v)$ is the instrumental smeared version of $N(v)$.
$N_a(v)$ and $N(v)$ will have different values in presence of a saturated or unresolved line. In the case of a saturated feature, it would be useful to compare the results of $N_a(v)$ for two or more absorption lines of a given species, which differ in the product $f\lambda$ (Savage and Sembach, 1991; Jenkins, 1996).
The AOD method provides a reliable measure of the column density for spectra with S/N $\gtrsim$ 20, while it will likely overestimate the value of N, if applied to data with low S/N (Fox et al., 2005). This overestimation results from the non-linear relationship between the flux on a given detector pixel and $\tau_a(v)$ in that pixel.
In order to lessen the distortion, one artifice can be to rebin the spectrum before the measurement, since the rebinning process increases the S/N. Unfortunately, the gain in the accuracy of $N_a(v)$ is made at the expense of resolution, so the kinematic information is lost.
In case of marginally resolved lines, instead, the value of the apparent column density will be underestimated at high line depths, since the high optical depth pixels are smoothed to a lower value of the apparent optical depth. The low-resolution effect works in the opposite direction to the S/N effect (Fox et al., 2005).
For a more detailed discussion about the accuracy of $N_a(v)$ as a function of the line depth or S/N, I refer the reader to the above mentioned paper.
Apart from the problems related to the goodness of the data, the AOD method has important advantages with respect to the curve of growth or line profile fitting, which are summarized here:

- it is computationally simpler;

- it provides significant information about the velocity dependence of line saturation;

- it is easily applicable in situations of multiplet components, where the curve of growth or the line fitting analysis are not manageable, due to a kinematical complexity along the line of sight;

- in case when only a single unsaturated line is present, the integration of $N_a(v)$ over velocity provides a better lower limit to the column density than a simple equivalent width measurement.

2.6 Classification of QSO absorption lines

Intervening gas clouds between the background QSO and the observer give rise to absorption features in the spectrum of the QSO. There is a standard classification scheme that divides absorption systems into four categories according to their neutral hydrogen column density.
Gas clouds with $N_{HI} \leq 10^{17}$ cm^{-2} are called Lyα forest absorption systems, which produce very sharp absorptions.
From $10^{17} \leq N_{HI} \leq 10^{19}$ cm^{-2} they are called Lyman Limit systems (LLSs). These systems are thick enough that the gas is opaque to photons capable of ionizing HI, those with energies greater than 13.6 eV. For this reason, they are defined by a sharp break in the spectrum at the Lyman limit (912 Å). In these systems there is some neutral hydrogen remaining, screened by the outer layers.
Absorption lines with $N_{HI} \geq 2 \times 10^{20}$ cm^{-2} (Wolfe et al., 1986) are called damped Lyman α systems (DLAs), because of the pronounced damping wings in their absorption profiles. They are assumed to be characterized by an efficient self-shielding at these column densities, so they are predominantly neutral. They are rarer than LLSs and at low redshift they are usually associated with galaxies, as their column densities are also typical of sightlines in the Milky Way. At higher redshift, they are not always associated with a visible galaxy and they are thought to be associated with progenitors of spiral discs.
Finally, systems with $10^{19} \leq N_{HI} \leq 2\times10^{20}$ cm^{-2} are classified as sub-DLAs (Péroux et al., 2003; Dessauges-Zavadsky et al., 2003) or also as super-LLSs (Prochaska et al., 2006). These systems are characterized by line profiles with damping wings as DLAs,

but they are different from them, as they are not totally neutral, but they are partially ionized.
Classifications are, of course, not exclusive; DLAs systems will produce also the Lyman break, for example.
Metal lines have been observed associated to all of the four classes. Different ionizations states can provide complementary information, as low- and high-ionizations states trace gas at different temperatures and densities. In general, high-column densities absorbers can exhibit both weakly and highly ionized species, while low-column densities absorber tend to be associated with highly ionized gas.
The most common absorption features are Mg II (e.g., Berg et al., 2017; Lundgren et al., 2013, 2015; Steidel and Dickinson, 1992; Nestor et al., 2003), O VI (e.g., Schaye et al., 2000; Simcoe et al., 2004; Aguirre et al., 2008; Frank et al., 2010; Bergeron and Herbert-Fort, 2005) and C IV (e.g., Cowie et al., 1995; Songaila, 1998; Tytler et al., 1995; Schaye et al., 2003; Ellison et al., 2000; Pieri et al., 2006; D'Odorico et al., 2010, 2016), but also Si IV, Si III,C III and N V (e.g., Schaye et al., 2003; Aguirre et al., 2004; Fechner and Richter, 2009).
Lines, such as Mg II and C IV, have rest-frame wavelengths longer than the Lyα line, so they are easily observable, as they are not embedded in the thick Lyα forest, like O VI. Especially C IV can be easily observed in the optical band at $z \gtrsim 1.2$.
The ionization thresholds of the these species are different, suggesting that they trace different gaseous environments. Lines, like Mg II or the Lyα itself, may trace a relatively cold phase with a temperature $T \sim 10^4$ K, while species like C IV or O VI are associated to a hotter phase at a temperature $T \sim 10^5 - 10^7$ K.
Thus, studying different metal absorption line systems is very important for understanding the different phases of the IGM, their evolution and their connection with galaxies and their feedback.
In this thesis, I focused mainly on this last issue.

Chapter 3

Physical and chemical properties of the IGM

In this chapter, I will describe some of the properties of the IGM and the underlying physics.

3.1 The Gunn-Peterson Test

The Gunn-Peterson effect is a probe of the reionization history of the Universe. It was first proposed by Gunn and Peterson (1965) as a test to verify the presence of a uniform component of neutral Hydrogen in the IGM, that would have produced an absorption trough in the region blueward of the Lyα emission line in the spectra of high redshift QSO.
When the first observations of high redshift QSOs (e.g. Schmidt, 1965) did not show the expected trough, Gunn and Peterson (1965) concluded that either the Universe was roughly "empty"and by the time the Lyα forest is observed, the majority of the matter has condensed into galaxies, or most of the Hydrogen was not in the neutral form, where it can produce the Lyα absorption, but was fully ionized.
I now explain what are the physical mechanisms behind the Gunn-Peterson trough. Considering that light travels towards the observer along a light path given by the formula:

$$\frac{dl}{dz} = \frac{c\,dt}{dz} = \frac{c}{\dot{a}}\frac{da}{dz} = c\frac{a}{\dot{a}(1+z)} = \frac{c}{H_0(1+z)E(z)} \tag{3.1}$$

with

$$E(z) = \sqrt{\Omega_{\Lambda,0} + \Omega_{k,0}(1+z)^2 + \Omega_{m,0}(1+z)^3 + \Omega_{r,0}(1+z)^4} \tag{3.2}$$

from equations of Section 2.2, we can derive the probability of a resonant scattering of a photon in a proper spatial interval dl, which is:

$$d\tau = n_{\rm HI}(z)\sigma(\nu_0(1+z))dl \tag{3.3}$$

where $n_{\rm HI}(z)$ is the volume number density of neutral Hydrogen atoms of the absorbing cloud, $\sigma(\nu_0(1+z))$ is the cross-section for the Lyα transition and ν_0 is the observed frequency of the transition for a scattering gas cloud placed at redshift z. The total optical depth at a frequency ν_0 is:

$$\tau_{GP} = \int_0^z n_{\rm HI}(z)\sigma(\nu_0(1+z))\frac{dl}{dz}dz = \frac{c}{H_0}\int_0^z \frac{n_{\rm HI}(z)\sigma(\nu_0(1+z))}{(1+z)E(z)}dz \tag{3.4}$$

Since the cross-section can be approximated by a Dirac delta function, this leads to:

$$\tau_{GP} = \frac{c}{H_0}\int \frac{n_{\rm HI}(z)\sigma(\nu_0(1+z))}{E(z)}\frac{d\nu}{\nu} = \frac{\sqrt{\pi}e^2 f}{m_e\nu_\alpha}\frac{n_{\rm HI}(z)}{H_0E(z)} \tag{3.5}$$

where ν_α is the Lyα resonance frequency. It is, then, possible to inverte the equation and to derive:

$$n_{\rm HI}(z) = 2.4131\cdot 10^{-11}h\tau_{GP}(z)E(z) \quad cm^{-3} \tag{3.6}$$

In order to know how much gas is neutral or if it is mainly ionized, the mean total Hydrogen number density $\bar{n}_H$ must be computed. Assuming that the majority of the baryons at a given redshift z are in the diffuse IGM gas, this can be expressed as:

$$\bar{n}_H(z) = (1-Y)(1+z)^3\Omega_{0,b}\rho_{0,crit} = 1.124\cdot 10^{-5}(1-Y)(1+z)^3\Omega_{0,b}h^2 \quad cm^{-3} \tag{3.7}$$

where Y is the Helium fraction, $\Omega_{0,b}$ is the baryon density parameter and $\rho_{0,crit}$ is the present critical density.
This leads to:

$$\frac{n_{\rm HI}(z)}{\bar{n}_H(z)} = 1.5\cdot 10^{-4}\frac{h\tau(z)E(z)}{(1+z)^3}\frac{0.019}{\Omega_{0,b}h^2} \tag{3.8}$$

If we consider a matter-dominated Universe, an approximation valid at high redshift, the above formula becomes:

$$\frac{n_{\rm HI}(z)}{\bar{n}_H(z)} = 1.5\cdot 10^{-4}h\tau(z)\frac{0.019}{\Omega_{0,b}h^2}(1+z)^{-3/2} \tag{3.9}$$

If we observe a residual flux in the region blueward of the Lyα line of the order of 10% of a QSO spectrum at $z = 6$, for example, which corresponds to $\tau \sim 2.3$, we

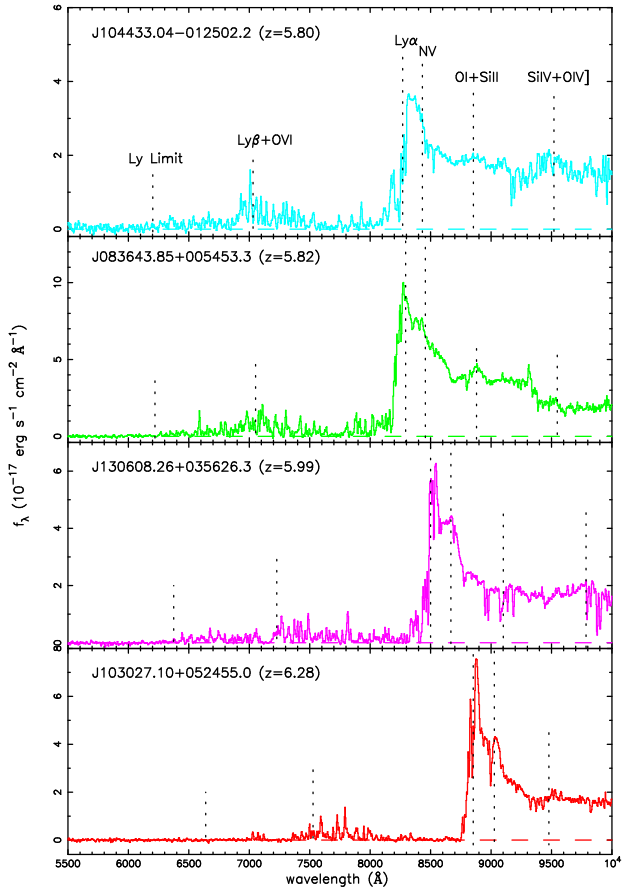

Figure 3.1: Optical spectra of 4 QSOs at $z > 5.8$ in the observed frame. Residual flux in the region blueward of the QSO Lyα emission line is observed in each spectrum and it is considered as an evidence of the ionized state of Hydrogen gas. Figure taken from Becker et al. (2001).

can infer:

$$\frac{n_{\rm HI}(z)}{\bar{n}_H(z)} \sim 10^{-6} \tag{3.10}$$

The Lyα scattering cross-section is so big, that even a tiny fraction of neutral Hydrogen would produce a significant absorption in a QSO spectrum, resulting as a trough in the region blueward the Lyα. Observing some residual flux in this region, even if small, is the evidence that the Universe is fully ionized.

In Fig.3.1, four QSO spectra at $z > 5.8$ are shown. The Lyα absorption strongly evolves with redshift, approaching nearly a trough, but the flux does not completely drop to zero. This is an evidence that at $z \sim 6$ the Universe is ionized, even if the significant drop in the absorption suggests that we are not very far from the end of the epoch of reionization.

3.2 General properties of absorption lines

3.2.1 Column density distribution

The column density distribution function, that is the number of absorption systems in a given column density bin at a certain redshift, provides similar information for the IGM as the luminosity function for galaxies.
As described in Chapter 2, there are different methods to derive the column density of an absorption system. In presence of high resolution data, Voigt profile fitting provides the best analysis of absorption features, because it decomposes the line profile in the various single components, giving information on their velocity structure. Measurements using the curve of growth method are just an integrated measure of the total system, instead.
The H I column density range measured so far is in the interval 10^{12}-10^{22} cm^{-2}; lower column densities are difficult to detect, while an upper limit is predicted by Prochaska et al. (2005).
The functional form for the distribution function was recognized by Tytler (1987) to be a power-law, $dN/dN_{\rm HI} \propto N_{\rm HI}^{-\beta}$ with $\beta = 1.5 - 1.7$ (Hu et al., 1995; Kim et al., 2002a; Tytler, 1987).
Fig. 3.2 shows the Lyα column density distribution function determined by Kim et al. (2013), using absorption systems in the redshift range $2.2 < z < 3.2$.

The drop of the function at low column densities is due to sensitivity, while the flattening at $N_{\rm HI} > 10^{18}$ cm^{-2} is due to self-shielding. The H I column density distribution function does not show a strong evolution in redshift (e.g., Kim et al., 2013; Williger et al., 2010; Rahmati et al., 2013). For example, Rahmati et al. (2013) show that the predicted function evolves only weakly from $z = 5$ to $z = 0$. Only below the Lyman limit range, the number of absorbers at $z > 3$ slightly increases with z as the Universe becomes denser while the UV background intensity remains similar. At lower redshift, the combination of decreasing UV background and the expansion of the Universe results in a non-evolving H I column density distribution function.

3.2.2 Doppler parameter distribution

The Doppler parameter distribution shows that the majority of Lyα systems falls in the interval $15 < b_{\rm obs} < 60$ km s^{-1} (Atwood et al., 1985; Carswell et al., 1991; Rauch et al., 1992; Hu et al., 1995; Lu et al., 1996; Kim et al., 1997; Kirkman and Tytler, 1997), as shown in Fig.3.3.

As described in Chapter 2, $b_{\rm obs}$ is not a direct measure of the gas temperature,

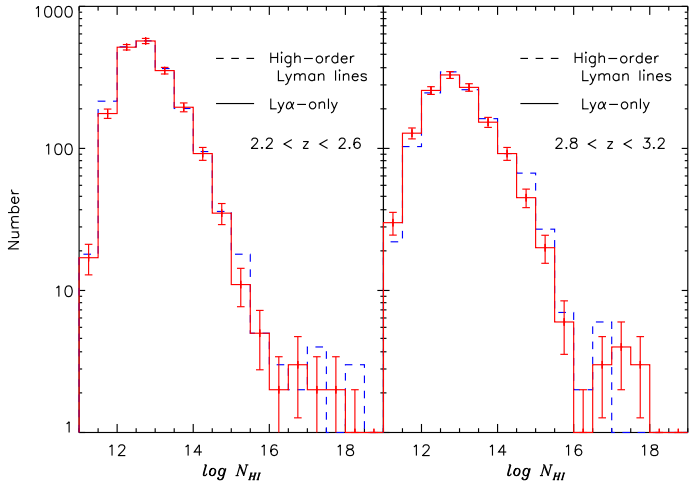

Figure 3.2: HI column density distribution function for absorption features in the redshift ranges $2.2 < z < 2.6$ and $2.8 < z < 3.2$. The Lyα-only fits are shown as solid lines, while the higher order Lyman fits are marked as dashed lines. The drop at low column densities is due to sensitivity. Figure taken from Kim et al. (2013).

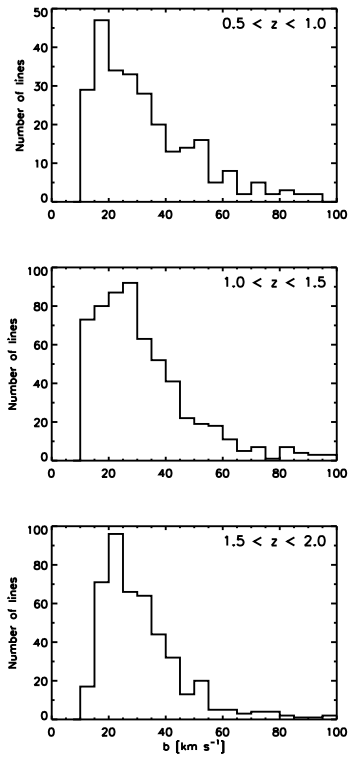

Figure 3.3: HI Doppler parameter distribution function for absorption features in different redshift ranges. No strong evolution is observed. Figure taken from Janknecht et al. (2006).

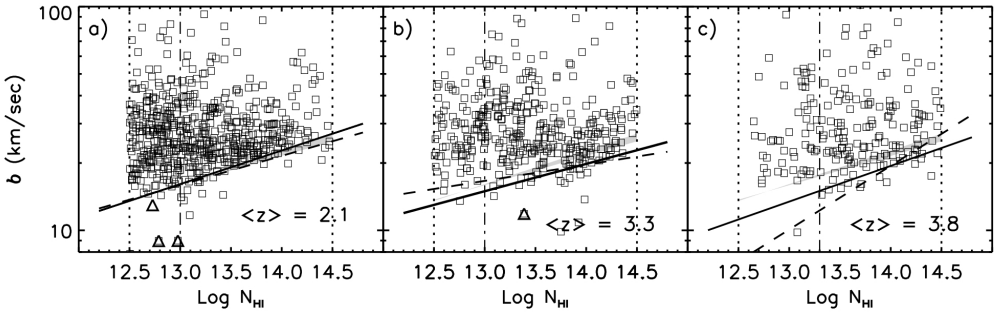

Figure 3.4: The $b_{\rm obs}$-N distribution at three different redshifts. Dotted lines indicate the $N_{\rm HI}$ ranges considered in the work by Kim et al. (2002b). Dot-dashed lines represent the lower $N_{\rm HI}$ fitting threshold actually used in the fit, above which incompleteness is negligible. Solid line marks the lower cutoff in the $b_{\rm obs}$ distribution. This cutoff shifts at lower values for increasing redshift. Solid lines and dashed lines represent two different fitting methods, as described in Kim et al. (2002b). Figure taken from Kim et al. (2002b).

because it contains also the information about turbulent motions. Nevertheless, it provides an upper limit for the gas temperature.

Fig.3.4 reports the $b_{\rm obs}$-N distribution at three different redshifts, taken from Kim et al. (2002b). At a fixed column density, the $b_{\rm obs}$ parameter shows a wide spectrum of possible values with a lower limit (solid line), which slightly increases with redshift. This lower limit to the line width is directly set by the thermal state of the gas. In fact, lines cannot have a width smaller than the value set by its thermal motions (see Eq. 2.18).

The fit to the lower cutoff increases slightly with the column density and this is a consequence of the equation of state of the low-density gas (Hui and Gnedin, 1997; Schaye et al., 1999). For overdensities $\delta \lesssim 10$, the temperature of the gas is predicted to be tightly correlated to its overdensity. The relation is defined by $T = T_0(1+\delta)^{\gamma_{\rm T}-1}$, where T is the gas temperature, T_0 is the gas temperature at the mean gas density and $\gamma_{\rm T} - 1$ is constant at a given z. Assuming ionization equilibrium, this relation is driven by the competition between photoionization heating of the UV radiation background and adiabatic cooling due to the Universe expansion and it strongly depends on cosmology and reionization history. In fact, the earlier the epoch of reionization, the lower the gas temperature at a given redshift, except in the case where the reionization happens at very high redshift (z >10). In this case, the temperature-density relation approaches an asymptote. Moreover, also the slope of the relation depends on the epoch of reionization, becoming steeper the

earlier the Universe reionizes.
The observational equivalents to T and δ of this relation are $b_{\rm obs}$ and $\rm N_{HI}$, respectively.
The mild redshift evolution of the cutoff fit is related to the conversion from theoretical overdensity to observed column density. Davé et al. (1999) derived a simple relation between δ and $\rm N_{HI}$ given by the formula:

$$N_{\rm HI} \sim [0.05(1+\delta)10^{0.4z}]^{1.43} \times 10^{14} \quad cm^{-2} \tag{3.11}$$

The overdensity associated to a given $\rm N_{HI}$ increases for decreasing redshift. The explanation behind this change is related to the expansion of the Universe and to the consequent drop of the value of the mean gas density.

3.2.3 Number density evolution

If the column density and Doppler parameter distributions show only a mild evolution with the redshift, this is not the case for the line number density, defined as the number of absorption systems above a threshold column density per unit redshift. Empirically it is described as:

$$\frac{dn}{dz} = \left(\frac{dn}{dz}\right)_0 (1+z)^{\gamma} \tag{3.12}$$

where $(dn/dz)_0$ is the local comoving number density of the Lyα forest. The number density evolution of the Lyα forest in the column density range $\rm N_{HI} = 10^{14} - 10^{17}$ $\rm cm^{-2}$ by Kim et al. (2013) is shown in Fig. 3.5.
It is clear from the picture that there is an abrupt change in the slope of the relation. At high redshift (z >1.5), the observed relation is fitted by $dn/dz = 6.1(1+z)^{2.47\pm0.18}$, while at lower redshift Weymann et al. (1998) found $dn/dz = (32.7 \pm 4.2)(1+z)^{0.26\pm0.22}$.
The rapid change in the slope of the relation between low and high redshift is due to the expansion of the Universe and to the changes in the UV background intensity. At high redshift, the expansion of the Universe, which causes a rapid decline in the gas density and so in the recombination rate, works together with an increasing UVB intensity, strongly ionizing the gas and the neutral HI fraction is lowered. At low redshift, the UVB intensity drops, due to a decline in the star formation rate and QSO space density. The fading of the UVB does not cooperate with the Universe expansion anymore and this causes a consequent increase in the observed neutral fraction (Davé et al., 1999).

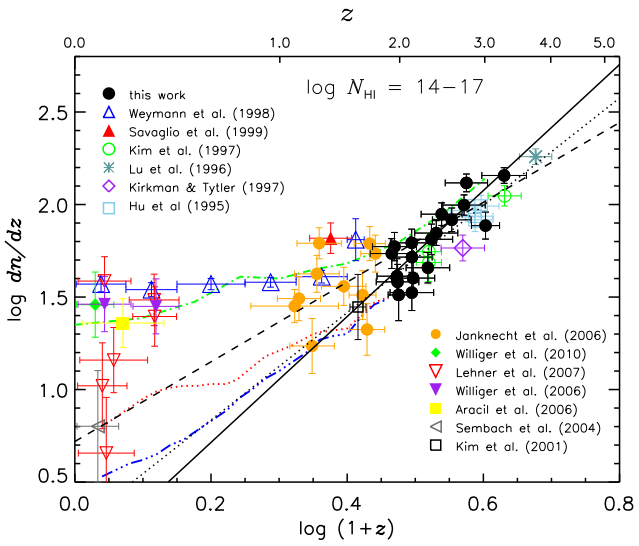

Figure 3.5: Number density evolution of the Lyα forest in the column density range $N_{HI} = 10^{14} - 10^{17}$ cm^{-2}. Lines are fits obtained by considering different subsamples of data or they are predictions obtained under different assumptions, as explained in Kim et al. (2013). Figure taken from Kim et al. (2013).

3.2.4 Characteristic sizes of absorbers

The characteristic size of absorption systems is of the order of the local Jeans length (Schaye, 2001). The characteristic size is defined as the size of the region for which the density is of the order of the characteristic density of the absorber.
Consider a gas cloud with a characteristic density n_H. The dynamical or free-fall time is defined as:

$$t_{dyn} = \frac{1}{\sqrt{G\rho}} \sim 10^{15} \left(\frac{n_H}{1cm^{-3}}\right)^{-1/2} \left(\frac{1-Y}{0.76}\right)^{1/2} \left(\frac{f_g}{0.16}\right)^{1/2} \quad s \tag{3.13}$$

where G is the gravitational constant, Y is the Helium mass fraction and f_g is the gas mas fraction.
The sound crossing t_{sc} is defined, instead, as:

$$t_{sc} = \frac{L}{c_{cs}} \sim 2.0 \times 10^{15} \left(\frac{L}{1kpc}\right) \left(\frac{T}{10^4 K}\right)^{-1/2} \left(\frac{\mu}{0.59}\right)^{1/2} \quad s \tag{3.14}$$

where c_{cs} is the sound speed and μ is the mean molecular weight.
In hydrostatic equilibrium, $t_{dyn} \sim t_{sc}$ and this defines a characteristic length called the Jeans length:

$$L_J = \frac{c_{cs}}{\sqrt{G\rho}} \sim 0.52 n_H^{-1/2} \left(\frac{T}{10^4 K}\right)^{1/2} \left(\frac{f_g}{0.16}\right)^{1/2} \quad kpc \tag{3.15}$$

To make a connection with observation, it is possible to define a "Jeans column density ":

$$N_{\rm H,J} = n_H L_J \sim 1.6 \times 10^{21} n_H^{1/2} \left(\frac{T}{10^4 K}\right)^{1/2} \left(\frac{f_g}{0.16}\right)^{1/2} \quad cm^{-2} \tag{3.16}$$

In general, $t_{dyn} \sim t_{sc}$ only locally, but not for the cloud as whole. In fact, the Jeans length is defined for spherical clouds and not for typical growing density perturbations, for which the collapse is not synchronized along the three spatial directions.

Large departures from hydrostatic equilibrium do occur when the pressure changes on a timescale shorter than the dynamical time. This is what happens, for example, during the reionization epoch, where a sudden increase in the IGM temperature is translated in a sudden increase of the Jeans length and until forces do not restore local hydrodynamical equilibrium, the gas can be clumpy on scales smaller than the Jeans length.

3.2.5 Clustering

An important question is if Lyα absorbers trace the same large scale structure as galaxies or if they are more randomly distributed. A simple measurement of the clustering is given by the two point correlation function of absorbing lines in redshift (velocity) space along the line of sight, that is defined as the excess probability of finding another absorbing line in an infinitesimal redshift interval δz at a redshift separation Δz from the first one at z_1:

$$\delta P(\Delta z) = \left(\frac{dn}{dz}\right)_{z1} [1 + \xi(\Delta z)] \delta z \tag{3.17}$$

Thus $\xi(\Delta z)$ can be derived by counting pairs of lines at different redshift separations.

It has been found that significant clustering signal is detected only at small separations $\Delta v \lesssim 300$ km s^{-1} (e.g., Rauch et al., 1992; Cristiani et al., 1997). The clustering amplitude $\xi(100$ km s$^{-1}) \sim 0.5$ is much lower than the measured one for local galaxies at the same spatial distance, assuming that $\Delta v \sim H_0 \Delta r$. The amplitude of ξ increases with the HI column density (Cristiani et al., 1995, 1997). Unfortunately, due to line blending, the clustering signal at small separations can

be drastically underestimated (Rauch et al., 1992).
The indication is that Lyα forest seems not to be as strongly clustered as galaxies. Other methods can also be used. For example, it is possible to derive ξ from the power spectrum of the normalized transmitted flux $F(\lambda) = e^{-\tau(\lambda)}$. The normalized flux $F(\lambda)$ in a wavelength range is Fourier transformed and a power spectrum as a function of k (the wavenumber corresponding to a certain redshift separation) is obtained.
Another interesting method is given by the void probability function, designed to detect voids in Lyα forest. If Lyα lines have a Poisson distribution along the line of sight, then the probability of a gap of Δz in the redshift distribution is:

$$P(z, \Delta z) = e^{-\left(\frac{dn}{dz}\right)\Delta z} \tag{3.18}$$

Any deviations from this distribution is a signal of clustering. Carswell and Rees (1987) found that voids with dimensions as great as those in galaxy distributions ($\sim$ 50 $h-1$ comoving Mpc) are extremely rare for Lyα forest, showing no strong clustering signal. This result has been confirmed also by other studies based on larger dataset than the one by Carswell and Rees (1987).

3.3 Early Models of IGM

Different models have been proposed for describing the physical structure of the IGM and its origin. In this section, a brief review of the most influential models is given.

3.3.1 Pressure confinement

The first model, which was proposed, was the one in which absorption features are produced by cold ($T \sim 10^4$ K) discrete clouds, which are pressure-confined by a hotter and more tenuous medium (Sargent et al., 1980).
These two components are considered to be in pressure equilibrium. Since the Universe expands, the pressure of the hot ambient gas must drop as $P \propto \rho T \propto (1+z)^5$ for adiabatic expansion. Consequently, as the temperature of the cold phase is roughly constant, as derived from observed Doppler parameters, the density of cold clouds must drop as $\rho_{\rm cold} \propto (1+z)^5$.
One motivation to this model at the time was that the hot ambient gas needed to confine cold clouds could also be responsible for the observed X-ray background.
This model suffered from different problems. First of all, the observed HI column

density range ($10^{13} < \mathrm{N_{HI}} < 10^{16}$ cm^{-2}) requires ± 9 orders of magnitude in the cloud mass ($\mathrm{N_{HI}} \sim n_{\mathrm{HI}} R_{cloud} \sim M_{cloud}^{1/3} J^{-1} P^{-5/3}$, with J the ionizing flux and P the gas pressure) or a factor $\sim$100 for the pressure. Both values are quite difficult to realize.

Moreover, this hot component would produce strong distortions in the CMB, which are not observed. Finally, there is now evidence that the X-ray background is formed by discrete sources rather than a diffuse medium.

Although this model has been discarded, pressure confinement may happen for some systems in galaxy halos.

3.3.2 Gravitational confinement

Self-gravity. Self-gravitating clouds were first proposed by Melott (1980) and Black (1981) in alternative to pressure confinement. In particular, Black (1981) studied the properties of this clouds and he found that in order to be consistent with observations, they had to be very extended (± 1 Mpc). They must be truncated by an external medium or large enough to overlap and provide their own boundary pressure. In this model, Lyα clouds are due to strong internal gradients of the neutral gas density rather than to a transition between different gas phases. The model met some scepticism as the sizes of the absorbers were too large and it had some problems also in reproducing the column density distribution (Petitjean et al., 1993).

Cold dark matter minihalos. The advent of theories of gravitational structure formation, where large-scale structures are produced by gravitational instability, led to the hypothesis that also Lyα clouds were related to this larger frame. All the physical parameters for the absorbers can be predicted as a consequence of cosmological models.

In small dark matter halos, the gas is stable if the potential well is too shallow for the photoionized gas to cool and collapse, but deep enough for the gas not to escape. CDM minihalos are more compact than the self-gravitating clouds of previous model, because of the larger dark matter gravity.

Because of the large density range for perturbations, a large interval in column densities can be produced and since minihalos are constantly produced from collapse and destroyed by merging, some evolution in the absorber number density is expected.

Since minihalos have generally $M_{halo} < M^*$, where M^* is the mass corresponding to the characteristic luminosity L^* of the luminosity function, they are also expected to be weakly clustered.

3.4 Lyα forest in hierarchical models

The minihalo model is obviously an oversimplification, as the collapse in hierarchical models is highly non-spherical, but it proceeds from sheets to filaments to halos. At any given time, the Universe consists of halos, filaments and sheets and density perturbations still in the linear regime. All these structures can produce absorption features in QSO spectra, as long as the H I column density is sufficiently high. For this reason, it is more correct to consider Lyα absorbers arising from the entire cosmic density field rather than being discrete clouds.

This change of notion started with Bi and collaborators (Bi et al., 1992; Bi, 1993; Bi and Davidsen, 1997); they realized that optical depth fluctuations corresponding to linear density fluctuations in the IGM can give a realistic representation of the Lyα forest, while higher column density systems may be produced by collapsed objects. Their semianalytical work is based on a log-normal density fluctuation field. For low densities, the collapse of baryons differs from the DM collapse for the presence of gas pressure, which acts in smoothing the baryon distribution on scales lower than the Jeans length.

Bi and collaborators treated the pressure as a modification of the baryon power spectrum, suppressing power at scales smaller than than λ_J:

$$\delta_b(k) = \frac{\delta_{DM}}{1 + k^2(\lambda_J/2\pi)^2} \tag{3.19}$$

where k is the wavenumber and δ_{DM} is dark matter overdensity.

From the 1990s, hydrodynamical simulations became sufficiently realistic to be able to predict the physical properties of the Lyα forest. By analysing simulated QSO spectra generated piercing artificial slices of Universe, it became possible to examine the correspondence between Lyα absorbers and the physical properties of the underlying gaseous structure. The generic picture that emerged is that low column density systems ($N_{HI} < 10^{14}$ cm^{-2}) arise from sheet-like structures. Low column density gas remains unshocked and just bounces back because of hydrostatic pressure.

Higher column density systems ($N_{HI} \sim 10^{14}$ cm^{-2}) arise in more filamentary structures, while increasing the column density, absorbers become more and more spherical ($N_{HI} > 10^{16}$ cm^{-2}), entering in a regime where absorbers correspond to minihalos. The visual appearance of all these different systems has been described as a "Cosmic Web "(Bond and Wadsley, 1997).

Simulations have been quite successful in reproducing the overall observational properties of absorbers, even if a lot of questions, regarding for example the metal en-

richment or the epoch of reionization, are still open and a lot of work has still to be done.

3.5 Statistics of the transmitted flux

Absorption line parameters, derived for example from Voigt profile fitting, give information on the physical characteristics of absorption systems. A more straightforward and direct analysis of the IGM can be made treating the flux as a continuous field and by measuring its statistical properties, such as the mean transmitted flux, the flux Probability Distribution Function (PDF) and the flux power spectrum. The correlation between the optical depth and the density can be made considering the *Fluctuating Gunn Peterson Approximation* (FGPA), a generalization of the Gunn-Peterson absorption, which assumes adiabatic expansion of a gas in photoionization equilibrium and obeying to a tight temperature-density relation. The FGPA is useful for modeling the large-scale clustering of the Lyα forest. At small scales, it is highly approximated, as it ignores the redshift space distortions due to gas peculiar motions. According to FGPA, the Lyα optical depth is proportional to:

$$\tau \propto T_0^{-0.7} \Gamma_{\rm HI}^{-1} \Delta^{2-0.7(\gamma-1)} \tag{3.20}$$

where T_0 is the gas temperature at the mean density, $\Gamma_{\rm HI}$ is H I photoionization rate, Δ is the overdensity and γ is the slope of the temperature-density relation.

3.5.1 Mean transmitted flux

The mean transmitted flux is the most basic observable of the Lyα forest and it is defined as:

$$\langle F \rangle = \langle e^{-\tau_{HI}} \rangle = e^{-\tau_{eff}} \tag{3.21}$$

where $\langle\rangle$ indicates the mean value averaged over wavelength and τ_{eff} is called the *effective optical depth*. Note that τ_{eff} is not the average of the optical depth. Kim et al. (2013) derived an empirical relation for the evolution of the mean transmitted flux as a function of the redshift from their sample of H I absorption systems at $1.7 < z < 4$. The best fit to their data is:

$$\tau_{HI}^{eff} = (0.0023 \pm 0.0007)(1+z)^{3.65 \pm 0.21} \tag{3.22}$$

in good agreement with previous measurements from the literature.

3.5.2 Flux PDF

The flux PDF is by definition the number of pixels which have a flux between F and $F + \Delta F$ for a given flux F divided by the total number of pixels (Jenkins and Ostriker, 1991; Rauch et al., 1997; McDonald et al., 2000; Kim et al., 2001).
The flux distribution encodes the information of the spatial distribution of the underlying matter and the thermal state of the IGM (Becker et al., 2007). However, it is largely sensitive to continuum fitting and contamination by metal absorption lines in the Lyα forest.
Analysis of the flux PDF compared to numerical simulations has suggested a possible inverted temperature-density relation at high redshift ($z \sim 2-3$), meaning that underdense regions may be hotter than generally assumed and the thermal state of the low density IGM is substantially more complex (Bolton et al., 2008; Viel et al., 2009; Calura et al., 2012). Different conclusions are instead reached by the study presented in Lee et al. (2015). Radiative transfer effects during He II reionization by QSOs are the most plausible explanation to this suggested inverted relation.

3.5.3 Flux power spectrum

The flux power spectrum $P_F(k)$ can be used to infer the matter power spectrum $P(k)$ (e.g., Croft et al., 1998, 2002; Viel et al., 2009). Following the FPGA, there is a strict correlation between the observed flux F and the gas density along the line of sight, which in turn traces also the dark matter density profile, because pressure gradients are small in the diffuse cool gas of the Lyα forest.
The 3D flux power spectrum can be recovered from the observed 1D flux power spectrum along the line of sight according to:

$$P_F(k) = -\frac{2\pi}{k}\frac{d}{dk}P_{F,1\mathrm{D}}(k) \tag{3.23}$$

$P_{F,1\mathrm{D}}(k)$ is measured by decomposing the absorption spectrum into Fourier modes and by measuring their variance as a function of the wavenumber. The underlying assumption is that $P_{F,1\mathrm{D}}$ is isotropic, which, in practice, is not correct at small scales where peculiar velocities and gas thermal motions are important. Then:

$$P(k) = b^2(k)P_F(k) \tag{3.24}$$

$b^2(k)$ is the bias function and it is inferred from simulations in order to reproduce the observed $P_F(k)$. It is fixed by matching the effective optical depth at the redshift under consideration. As already said, the measurement of τ_{eff} is strongly dependent

on the continuum fitting; for this reason, $b(k)$ is less constrained than $P_F(k)$.

3.5.4 Lyα forest as a cosmological probe

Lyα forest and its statistical properties can be used as an important and complementary tool to set cosmological constraints. It is a probe of the matter power spectrum in the mildly non-linear regime and it has demonstrated to be powerful in measuring the position of Baryonic Acoustic Oscillations (BAO) (Busca et al., 2013; Slosar et al., 2013). Busca et al. (2013) report, for example, the detection of the BAO feature in the 3D correlation function of the transmitted flux in the Lyα forest of high-redshift QSOs ($2.1 \leq z \leq 3.5$) from the BOSS survey. The peak is seen at a position of 1.01 $\pm$0.03 times the expected distance for BAO in concordance with ΛCDM model. Using Lyα forest instead of galaxy pairs for measuring BAO has certainly some interesting differences. First of all, galaxies surveys provide catalogues of positions that correspond to points of high-overdensities, while the forest provides an unbiased sample of points where the absorption is measured. Moreover, the forest is observable in a redshift range not accessible to galaxy surveys and where non-linear processes are less important in the theoretical modeling of cosmological structure formation.

McDonald et al. (2005) used $P_F(k)$ to provide a measurement of the linear matter power spectrum. They measured a linear power spectrum amplitude $\Delta^2_L(k_p = 0.009\, s\, km^{-1}, z_p = 3.0) = 0.452^{+0.069\,+0.141}_{-0.057\,-0.116}$ and a slope $n_{eff}(k_p, z_p) = -2.321^{+0.055\,+0.131}_{-0.047\,-0.102}$, which correspond to $\sigma_8 = 0.85$ and $n = 0.94$ for a ΛCDM model with $\Omega_m = 0.3$, $\Omega_b = 0.04$ and $h = 0.7$.

Lyα forest can be used also to disentangle warm dark matter (WDM) scenarios. For example, in Viel et al. (2013) they constrain the free streaming of WDM particles to the lower limit mass $m_{WDM} \gtrsim 3.3$ keV, which leads to a free streaming mass below which the mass function is suppressed of $2 \times 10^8 M_\odot$. This demonstrates that this is not enough to solve the small scale crisis of cold dark matter.

3.6 UV Background

The lack of the Gunn-Peterson effect is a probe of the highly ionized state of the IGM. There are two main processes by which the Universe can be ionized: collisional ionization and photoionization. Nowadays it is believed that the IGM is predominantly ionized by the latter process, because otherwise the needed temperature of the colliding particles would be too high to be consistent with the observed line

widths.

Photoionization is a process in which atoms are ionized by an incoming photon. The photoionization rate is indicated as Γ and its definition is given by:

$$\Gamma = \int_{\nu_L}^{\infty} \frac{4\pi J(\nu)\sigma(\nu)}{h\nu} d\nu \quad s^{-1} \tag{3.25}$$

where $\sigma(\nu)$ is the photoionization cross-section, ν_L is the frequency at the Lyman limit and $J(\nu)$ is the UV background intensity, expressed as $erg\, s^{-1} cm^{-2} sr^{-1} Hz^{-1}$. The UV background is the net radiation field due to the integrated contribution of all radiating sources. Thus, by measuring the UV background one can hope to place constraints on the evolution of the source population with redshift. The possible ionizing sources are QSOs and galaxies. It is known that QSOs emit copious quantities of photons and they play a major role in the IGM reionization. Despite this, QSOs alone are not sufficient for providing all the UV flux needed to reionize the Universe at the observed level, especially at redshift beyond $\sim$2, where the QSO space density is observed to decline. In this context, galaxies may play an important role, even if star-forming galaxies are dusty and it is quite difficult to estimate the exact escaping fraction of UV photons from these sources. Bianchi et al. (2001) estimated that the escape fraction is of the order $f_{\rm esc} \lesssim 0.1$ in order to match observations.

From an observational point of view, $J(\nu)$ can be derived from the QSO proximity effect or from the measurement of the flux decrement. In the former method, one focuses on the proximity region of the QSO, that is the region where the ionizing flux emitted by the QSO itself is comparable to the background. Weymann et al. (1981) noted that the number density of Lyα lines decreased as the redshift of the absorption line approached that of the QSO. The interpretation of this so called proximity effect is that near the QSO the absorbing clouds are more ionized than average because of the local UV radiation produced by the QSO. The extent of this proximity effect can be used to give constraints on $J(\nu)$. In fact, neglecting all the gas motions, the Lyα optical depth at any point is given by:

$$\tau^{prox} = \frac{\tau^{off}}{1 + w(r)} \tag{3.26}$$

where $w(r) = \Gamma^{\rm QSO}/\Gamma^{\rm bkg}$, $\Gamma^{\rm QSO}$ is the contribution to the photoionization rate due to the QSO itself at a proper distance r from it, and τ^{off} is the optical depth that would be obtained if the QSO were turned off. Near the QSO, $\Gamma^{\rm QSO}$ is large ($\Gamma^{\rm QSO} \propto r^{-2}$) causing the observed statistical decrease of absorption lines. Bajtlik

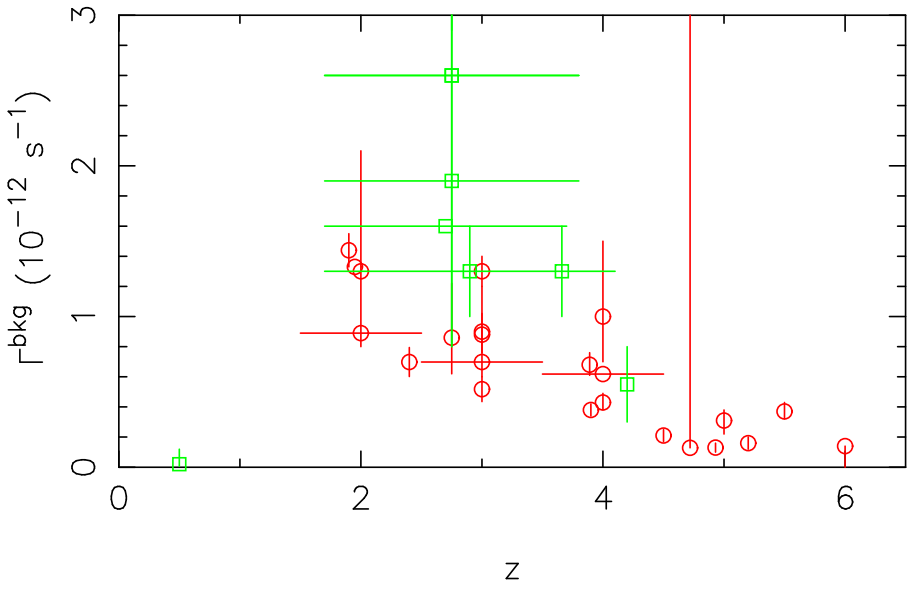

Figure 3.6: Observed measurements of $\Gamma^{\rm bkg}$ using the flux decrement method (red circles) and the proximity effect (green squares). The horizontal bars, when present, represent the redshift range over which the estimate applies. The vertical bars show the uncertainties in the measurements. Figure taken from Faucher-Giguère et al. (2008).

et al. (1988) developed a model for the variations of the density of absorption lines near the QSO to estimate $\Gamma^{\rm bkg}$.

The flux decrement method, instead, consists of a derivation of $\tau_{GP} \propto \Omega_b^2 h^3/\Gamma^{\rm bkg}$ by requiring that the mean flux decrement $D = 1 - e^{-\tau_{GP}}$ in a cosmological simulation agrees with the observed mean decrement.

The proximity effect method has generally yielded measurements of $\Gamma^{\rm bkg}$ higher than flux decrement estimates, suggesting unmodeled biases in one or both methods. There are indeed potential sources of bias in the proximity effect method, mostly owing to the peculiar environments in which quasars are thought to reside, that have not generally been modeled in proximity effect analyses. The flux decrement method is also not guaranteed to be unbiased, most importantly as it requires estimation of the unabsorbed continuum level. This is difficult to do reliably, especially at high redshifts where unabsorbed portions become increasingly rare, if existent at all, in quasar spectra. This method is also sensitive to assumed cosmological parameters, most notably Ω_b, If an independent measurement of $\Gamma^{\rm bkg}$ is available, then the flux decrement may be used to infer Ω_b. Fig. 3.6 shows existing measurement of $\Gamma^{\rm bkg}$ using both methods.

Theoretical computations of the UV Background were developed by Haardt and

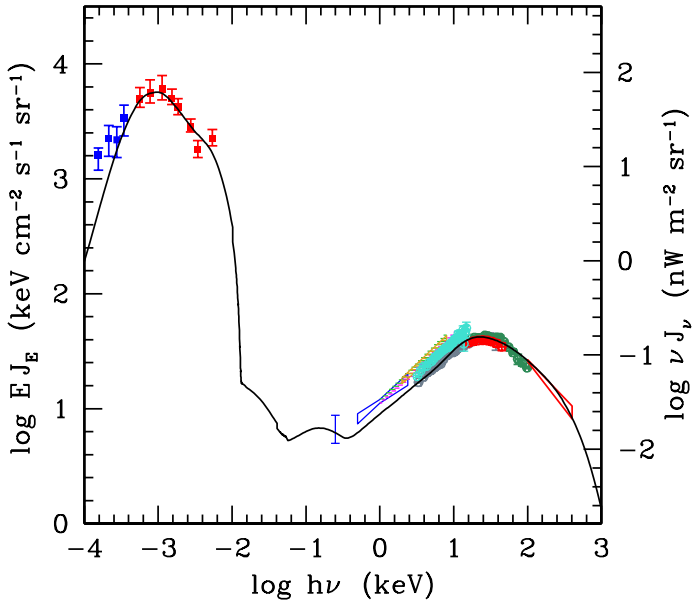

Figure 3.7: The Haardt and Madau (2012) predicted broadband extragalactic background, νJ_ν, from quasars and galaxies at z =0 compared with observed determinations at different wavelengths. *Red points*: data from Madau and Pozzetti (2000). *Blue points:* data from Fazio et al. (2004). $X-raypoints$: data taken from Gruber et al. (1999), Revnivtsev et al. (2003), Warwick and Roberts (1998),Kinzer et al. (1997), Georgantopoulos et al. (1996), Vecchi et al. (1999), Lumb et al. (2002) and De Luca and Molendi (2004)

Madau (1996, 2001, 2012), using the radiative transfer code CUBA. They consider two main contributions to the UV background emissivity: discrete sources, such as QSOs and galaxies, and also a diffuse emission of the IGM itself, due to H and He recombinations lines, which produce a sawtooth modulation of the UVB spectrum. The main differences between the models are the following: in Haardt and Madau (1996) only the contribution of QSO is considered, while in Haardt and Madau (2001) the contribution of galaxies is included and Haardt and Madau (2012) is a refinement of this last background.
Fig. 3.7 shows the predicted UVB by Haardt and Madau (2012).

3.7 IGM metal enrichment scenarios

Before the era of high resolution spectroscopy combined with large telescopes, QSO absorption lines were classified into two categories: 1) metal enriched high H I column density absorbers; 2) metal-free low H I column density absorbers ($N_{HI} < 10^{17}$ cm^{-2}). Thus, the IGM was thought to be chemically pristine. With the advent of powerful spectrographs, like HIRES at the Keck telescope and UVES at the ESO-VLT, absorption lines of the triply-ionised carbon doublet C IV ($\lambda\lambda$ 1548.204, 1550.778 Å), the most common metal transition found in QSO spectra, have been observed down to $N_{HI} \geq 10^{14.5}$ cm^{-2} at $z \sim 3$, in the so-called *Lyα* forest (Cowie et al., 1995; Tytler et al., 1995; Songaila, 1998).

As there is no $in-situ$ star formation activity in the IGM, due its high temperatures and low densities, and heavy elements are produced only by stars in galaxies, the main questions were: how can the IGM be polluted by metals? Can its physical properties shed light on the galaxy/IGM interplay? How far from galaxies can we observe metals?

Two main scenarios have been proposed for the IGM metal-enrichment, such as an early-enrichment by Population III stars at very high redshift ($10 < z < 20$) or galactic outflows/winds at lower redshift ($z \sim$ 2-3). Less consideration has gained the dynamical removal by galaxy mergers, as it cannot account for observed present-day mass metallicity relation (Aguirre et al., 2001).

In the first scenario, outflows from early protogalaxies drive the enrichment: metals can easily escape from the shallow potential wells, polluting large comoving pristine regions of the IGM. The enriched regions evolve following the Hubble flows likely resulting in a uniform distribution of metals at the studied redshift ($z \sim$2-3).

The second scenario predicts an overdensity-metallicity relation (Aguirre et al., 2001; Davé et al., 1998; Oppenheimer and Davé, 2006), resulting in a non-uniform metal pollution of the IGM.

Observations of metal abundances can quantify this metallicity-overdensity relation, constraining the enriching mechanism. CIV doublet can be used to trace the metallicity for different reasons: Carbon is the second most abundant metal element after Oxygen and its omnipresence in QSO spectra indicates that it traces a gas phase which is characteristic of many astrophysical gas environments. Moreover, it is quite easy to observe, as it falls in a region redward of the Lyα forest, free from line blendings, and observable in the optical band at $z \gtrsim 1.2$.

To test observationally which enrichment scenario is the dominant one, efforts have been concentrated on two main approaches: the investigation of the level of pollu-

tion in the low density gas at overdensities of a few and the detection of metals in the outskirts of galaxies.

The exploration of the low density regime has been attempted using two different methods: the stacking method (Lu et al., 1998) and the individual pixel optical depths (POD) of Lyα and C IV (Cowie and Songaila, 1998). Unfortunately, Ellison et al. (1999) revealed that the stacking method suffers from severe limitations, as the stacked signal in the C IV region is smoothed by random redshift differences between C IV and Lyα absorption, due to gas peculiar motions, and any sign of low metal pollution becomes difficult to recognize.

The observation of high S/N spectrum of the gravitationally lensed quasar B1422+231 ($z_{\rm em} = 3.623$) with the high resolution spectrograph HIRES at the Keck telescope has lead to interesting considerations. Ellison et al. (2000) showed that the 5 σ detection limit for C IV outside the Lyα forest in this object is $\mathrm{Log(N_{CIV})} \simeq 11.6$ for a Doppler value $b = 13$ kms and the column density distribution function corrected for completeness is fitted by the same power law at least down to $\mathrm{Log(N_{CIV})} = 11.75$, without showing a downturn. The POD result is consistent with an almost constant $\log(\mathrm{C\,IV/H\,I}) \sim -2.6$ down to $\tau(\mathrm{Ly}\alpha) \sim 2-3$ which implies that there are more C IV absorption systems with column densities below the detection limit. Only recently it has been possible to observe another QSO with a very high S/N (D'Odorico et al., 2016), which have shown that more than 40% of Lyα lines with column densities down to $\mathrm{Log(N_{HI})}\sim 14$ cm^{-2} have associated C IV absorption.

Further analyses based always on the POD technique have been carried out with larger samples (Schaye et al., 2003; Aracil et al., 2004). In particular, Schaye et al. (2003) measured the distribution of Carbon as a function of overdensity δ and redshift z. They used the high S/N spectrum of B1422+231 plus other 18 objects observed at lower S/N in their study, combined to hydrodynamical simulations to convert the measurement of the relation between the optical depths $\tau_{\rm CIV}$ and $\tau_{\rm HI}$ into a relation between [C/H], overdensity and redshift. They found that the carbon abundance is spatially highly inhomogeneous and is well-described by a log-normal distribution at fixed δ and z. They measure a median metallicity of $[\mathrm{C/H}] \simeq -3.47 + 0.65(\log\delta - 0.5) + 0.08(\mathrm{z} - 3)$ with a scatter $\sigma([\mathrm{C/H}]) \simeq 0.76 - 0.23(\log\delta - 0.5) + 0.02(\mathrm{z} - 3)$. They obtain a significant evolution with the overdensity valid down to approximately the mean density, but no evidence for a redshift evolution in the range $z = 1.8 - 4.1$. The statistical nature of this result does not provide the information on the distribution and covering factor of metals which could only be derived by a direct detection of the very weak metal lines and their association with the corresponding Lyα lines.

After the work by Ellison et al. (2000), the most ambitious surveys for weak associated metal absorption features, using Voigt Profile fitting of C IV lines, have probed only the densest portions of Universe by detecting systems with $\mathrm{LogN}(_{\mathrm{CIV}}) \gtrsim 12$ associated to $\mathrm{Log}(\mathrm{N_{HI}}) \gtrsim 14.5$ and corresponding to overdensities of a few at $z \sim 3$. At lower H I column densities, no associated C IV absorption is detected (Cowie and Songaila, 1998).

Also O VI absorption could be used to trace the metallicity in the low density IGM at $z \sim 2-3$ (e.g. Cen and Chisari, 2011), but its relevant absorption lines occur in the same wavelength range as the Lyman forest and are easily blended with the H I lines, which makes the detection of weak O VI absorption very difficult (e.g. Bergeron et al., 2002; Carswell et al., 2002; Simcoe et al., 2004).

On the other hand, galaxy/absorbers relations are constructed by searching for metal absorptions along a quasar line of sight and the galaxies at matching redshifts present in the field. Unfortunately, there are many results in literature concerning galaxy/absorbers cross-correlations with controversial results and, in general, they allow only a statistical insight into the problem. Furthermore, galaxy surveys are flux-limited, introducing an unavoidable bias in the observed galaxy/absorbers relations, as the faintest galaxies are missed.

The studies observationally carried out up to now both at high (e.g. Adelberger et al., 2005; Steidel et al., 2010; Turner et al., 2014) and low redshift (e.g., Prochaska et al., 2011; Tumlinson et al., 2011; Werk et al., 2013; Bordoloi et al., 2014; Liang and Chen, 2014) have agreed on the significant presence of metals in high and low ionization states at impact parameters at least as large as $\approx 100-300$ kpc, probing regions more typical of a circumgalactic medium (CGM) environment than of the IGM. This piece of evidence is not sufficient to discriminate between the different enrichment scenarios, since the same correlations at $z \sim 2-3$ could originate from the accumulation of older metals in higher density regions due to gravitational collapse (e.g. Porciani and Madau, 2005). Similar results for the size of the regions enriched by galaxies were found based on the clustering properties of metal absorbers (mainly C IV lines) along (e.g. Scannapieco et al., 2006) and across (e.g. Martin et al., 2010) the lines of sight to distant quasars.

Numerical hydrodynamical simulations that incorporate the relevant physical processes are thus a powerful tool to investigate these issues.

Recent observations of local starbursts have provided new insights into the nature and impact of supernova-driven winds. Observations of dwarf starbursts and luminous infrared galaxies generally find outflows when detectable (Martin, 2005; Rupke et al., 2005), observed as blueshifted Na I absorption arising from cold clumps en-

trained in hot metal-rich outflowing gas. While earlier data showed little trend of outflow properties with host galaxy properties (Martin, 1999; Heckman et al., 2000), these more recent data suggest that massive galaxies with higher star formation rates drive faster and more energetic winds.

Winds and outflows are expected to be the dominant processes that lead to ejection of metals from the interstellar medium (ISM) of galaxies. There is considerable evidence in favor of this mechanism for metal enrichment (Aguirre et al., 2001; Davé et al., 1998; Oppenheimer and Davé, 2006, e.g.,), also because observations have detected outflows around almost all galaxies at high redshifts (Heckman et al., 2000; Pettini et al., 2001; Frye et al., 2002; Shapley et al., 2003; Martin, 2005; Rupke et al., 2005). However, a clear picture of the outflows mechanisms is still not present and lots of questions are still open, such as how far from galaxies we can actually find metals.

Chapter 4

Cosmological simulations

Numerical simulations are a powerful tool to investigate cosmological structure formation and evolution, especially in the non-linear regime of gravitational dynamics. The ΛCDM cosmological picture has gained a leading role in the theoretical framework of structure formation, thanks to simulations.
Some of the most important results achieved through numerical simulations include the density profiles of dark matter halos (e.g., Navarro et al., 1996), the halo abundance (e.g., Jenkins et al., 2001), the dynamics of dark matter substructures (e.g., Tormen, 1997), the clustering properties of dark matter (e.g., Jenkins et al., 1998), the gas density and temperature in galaxy clusters (e.g., Evrard, 1990) and the Lyα forest properties (e.g., Hernquist et al., 1996). These developments are further fueled by the rapid progress in computer technology.
However, the cosmological picture regards many more complex astrophysical processes, which concern galaxy formation and the baryon evolution. The modeling of these processes, such as gas cooling, star formation, chemical feedback or energy input into gas by stellar winds, SN explosions or AGNs, is a hard task for several reasons. The physics behind some of these processes is currently not well understood and processes, such as star formation, are introduced using very simple recipes. Moreover, the range of spatial scales needed to simultaneously resolve the formation of cosmic structures in a representative volume of the Universe ($L \gtrsim 10$ Mpc) and the formation of stars ($L \lesssim 1$ pc) is huge.
This is quite unfeasible, thus even in the current best simulations of galaxy formation in a cosmological context, the most relevant processes are treated with analytical sub-resolution prescriptions. Sub-resolution processes are those that take place on scales smaller than the spatial resolution of the simulation. Detailed comparison with observations can provide important validations of different sub-resolution

models, but possibly without clearing the exact physical nature of the fundamental processes.
Numerical simulations can be divided into two main classes: pure N-body simulations and hydrodynamical simulations including sub-grid physics. Also the coupling between semi-analytical models (SAMs) and N-body simulations is a useful tool for the baryon physics modeling, but describing this complementary approach is beyond the scopes of this thesis.

4.1 Gravity solver algorithms

Gravity solver, or N-body, algorithms represent the backbone of a simulation. Their goal is to compute the gravitational force acting on each mass particle by solving the Poisson equation. In numerical simulations, the Universe is represented as a cubic "box", which contains a large number of particles, whose mass resolution ($m_{part} \sim 10^6$ $M_\odot$) is far too large compared to real particles.
To avoid particles "feel the edge of the box ", periodic boundary conditions are used. This means that a finite simulation is considered to be repeated infinitely in every direction.It also implies that when a particle exits from one side of the box, it reappears on the opposite side with the same velocity. Periodic boundary conditions are easy to implement if potentials are computed using Fourier Transforms.
Gravity solver algorithms in their essence can be described with a few basic steps:

1. set up initial conditions;
2. calculate gravitational force on each mass particle;
3. update position and velocity of each particle for a small time-step;
4. repeat from the second point until reaching the end redshift of the simulation.

Different techniques can be used for the calculation of the gravitational force, which will be briefly discussed here.

PP (Particle-Particle) or Direct Summation. The simplest way to calculate the gravitational force on a particle is to sum all the pairwise interactions between this particle and all the others. So, this method is a brute, but formally correct, computation of the Newton's law. The resulting acceleration will then be used to

update the particle velocity and position on a small time-step.
However, the problem related to this method is that, when particles are sufficiently close to each other, the gravitational force diverges and can be no longer numerically treated. A trick to bypass this problem is represented by the *softening length*, a term introduced in the Newton's law, modifying it in this way:

$$F_i = \sum_{j \neq i} \frac{G m_j}{\mid (\overrightarrow{r_i} - \overrightarrow{r_j})^2 + \epsilon^2 \mid^{3/2}} (\overrightarrow{r_i} - \overrightarrow{r_j}) \tag{4.1}$$

where F_i is the gravitational force acting on particle i, r_i and r_j are the particle's position of each considered pair and ϵ is the softening length. ϵ sets a sort of spatial resolution of the simulation, as it can be thought of as the "size "of simulated particles.
Since this calculation is a pairwise operation, the total time required to calculate all the forces is proportional to N^2, where N is the number of particles in the simulations, which makes it difficult to integrate systems with a particle number much larger than about 10^4 , even with present-day supercomputers.

PM (Particle Mesh) or grid method. This method calculates the potential by solving the Poisson equation on a grid of meshes. The density field in each grid point is computed by smoothing nearby particles masses with a kernel function, solving the Poisson equation on the grid and then, calculating the forces acting on each particle by differentiating and interpolating from grid points.
This method is faster than PP method, as the computational time cost scales linearly with N, but it has the disadvantage that forces are softened on a scale equal to the grid spacing.

P^3M (Particle-Particle-Particle-Mesh) method. An expedient in order to increase the spatial resolution of PM method is to combine it with the PP code. More specifically, forces due to distant particles are computed with the PM method, while nearby interactions are computed with the PP code. The transition between the two methods generally happens at ∼2-3 grid units. Actually, this simplest implementation of the P^3M code with a fixed mesh size is very time-consuming, when particles become highly clustered. An alternative is to use adaptive submeshes, that is a finer grid is used, whenever many particles are found within the same cell. PP method is applied only to particles with distances a few times the size of the finest grid.

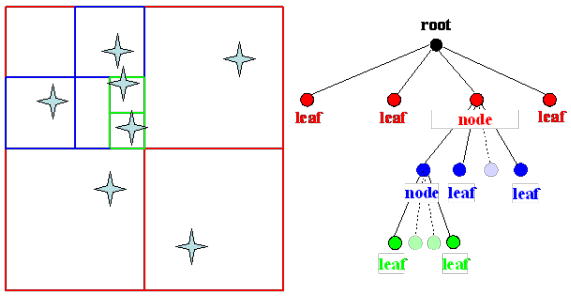

Figure 4.1: Illustrative representation of the space division applied in Tree codes. Space is divided in smaller cells until each unit contains at most one particle. A tree is built from this division and it will be traversed in the computation of the force. Figure taken from http : //www.kof.zcu.cz/st/dis/schwarzmeier/gravitational_simulation.html .

Tree method. The basic idea in this method is to group systematically distant particles into a single massive pseudo-particle and to compute the exerted force by it with the PP method. Going in more detail, the space is divided iteratively into smaller cubic cells until a cell contains at most one particle, as shown in Fig. 4.1. These cells form the nodes of a tree structure. The center of mass and the total mass for each subcell is computed and the force from each group, or pseudo- particle, is replaced by its multipole expansion.
The force computation proceeds by walking the tree and summing up appropriate force contributions from tree nodes. The multipole expansion of a node of size l is used only if r $> l$ $/\theta$, where r is the distance of the point of reference to the center-of-mass of the cell and θ is a prescribed accuracy parameter. If a node fulfills this criterion, the tree walk along this branch can be terminated, otherwise it is "opened", and the walk is continued, until a cell can be no more opened and the subcell is treated singularly with its direct summation of the force. This method has a computational time for a complete force evaluation of the order of N logN, so it is very fast. On the other hand, it requires large amounts of memory resources.

TreePM method. It is a smart combination of the PM and Tree methods, where the former is used to compute long range interactions and the latter for short range ones. It maintains the flexibility and large dynamical range of Tree codes, while at the same time speeding up the computation.

4.2 Hydrodynamics

Hydrodynamical simulations can follow the evolution of both the gas and the dark matter, by solving numerically gravitational and hydrodynamical equations. They are limited only by numerical resolution. For this reason, some of the most important physical processes have to be modeled approximately on a subgrid level, using recipes which are not so different from those adopted in semianalytical models. Nevertheless, the advantages with respect to the latter ones are related, for example, to the possibility of following the evolution of the halo distribution in detail with no prior assumption, as well as for the dark matter and baryon interactions, or to the possibility of following merger histories self-consistently as part of the dynamical process rather than being the result of simple prescriptions.
The intergalactic or interstellar gas can be represented as a smooth fluid, thanks to the small mean free paths of gas particles compared to the size of the structures they belong to. For this reason, its treatment and evolution can be followed by solving the equations of hydrodynamics representing mass, momentum and energy conservation, the so-called Navier-Stokes equations.
Gas dynamic equations can be written from two different point of view, which correspond to two classes of numerical codes: Eulerian codes (or Mesh codes) and Lagrangian codes (or SPH codes).

Eulerian schemes. The evolution of a fluid and its properties (like velocity, pressure, density, etc...) are followed at fixed positions on a cell grid. The fluid is, thus, discretized on a mesh and the fluxes of each physical quantity are evaluated at the cell boundaries in order to update their cell-averaged value on a single timestep. Modern codes consider an adaptive grid (Adaptive Mesh Refinement (AMR) codes), in order to improve the spatial resolution, which is the main limitation of these codes. On the other hand, they have the great advantage of being able to treat shocks without adding an artificial term, contrary to Lagrangian codes. Examples of current AMR codes are: ENZO code (Bryan et al., 2014), RAMSES code (Teyssier, 2010), FLASH code (Fryxell et al., 2000) and ART code (Kravtsov et al., 1997).

Lagrangian schemes. Each fluid element is represented as a particle and its evolution in time and space is followed. This scheme is easier to implement in N-body simulations, since it has a similar logic with respect to the one that treats DM particles, and the spatial resolution is automatically increased in denser regions. On the other hand, Lagrangian schemes have problems in treating shocks, which can

be captured only by adding to the equations an artificial viscosity, and very large gradients/discontinuities with a finite number of particles. The most popular Lagrangian method is the Smoothed Particle Hydrodynamics (SPH). In this treatment, the value of a generic variable is evaluated at any point as a smoothed estimate, that is a smoothed sum using a kernel function over nearby particles within the *smoothing length h*. The value of h specifies the fall-off of the kernel function with respect to the particle separation. Current SPH hydro codes are GADGET -2 (Springel, 2005), GASOLINE (Wadsley et al., 2004), VINE (Wetzstein et al., 2009), HYDRA (Couchman et al., 2011), CHANGA (Menon et al., 2015), SWIFT (Theuns et al., 2015) and GIZMO (Hopkins, 2014).

Moving mesh schemes. These codes represent a synthesis between Eulerian and Lagrangian codes, where the mesh is allowed to move with the flow. They are Galileian-invariant and adjust automatically their spatial resolution, like SPH-codes, but they are also able to capture shocks and discontinuities, like mesh codes. AREPO (Springel, 2010) is an example.

The SPH scheme is so far the most used scheme in cosmological simulation, but the optimal choice is, of course, problem dependent.

4.2.1 Sub-grid physics

To simulate the formation and evolution of galaxies, the most relevant physical processes have to be modeled using subgrid prescriptions. Dark matter interacts only through gravitational force, while gas can dissipate by cooling or absorb energy from an incident radiation field. Cooling, heating, star formation, feedback from SN or AGN are treated by means of approximate, phenomenological and uncertain prescriptions, able to regulate the mass and energy exchanges between the various components that are modeled in the simulation. In general, the recipes contain some tunable parameters, which are chosen in order to reproduce some observables. The concern is that the subresolution physics dominate the evolution of simulated galaxies.
Since star formation results from gravitational collapse of gas, star formation laws are in general described by the following equation (Katz, 1992):

$$SFR = \dot{\rho_\star} = f_\star \frac{\rho_{gas}}{\tau_{dyn}} \tag{4.2}$$

where $f_\star$ is the star formation efficiency and τ_{dyn} is a dynamical timescale. The dynamical time for gas to collapse is $\tau_{dyn} \propto 1/\sqrt{\rho_{gas}}$ and the star formation laws assume the generic form of Schimdt laws: $SFR = \dot{\rho_\star} = k\rho_{gas}^n$. This star formation implementation is inspired by observational results by Schmidt (1959) and Kennicutt (1998).

On the other hand, feedback is needed in order to reconcile with some observational evidences. In fact, in the absence of any feedback, gas cooling would lead to ∼80% of baryons condensed into galaxies by present day, while observations state that this percentage is only ∼ 5%. Moreover, feedback is a fundamental ingredient to shape both the faint and bright end of the galaxy luminosity function. Finally, without feedback, gas condenses and forms stars very early in small blobs that lose efficiently angular momentum to DM by dynamical friction and merge to form spheroids. The result are too small disk galaxies, which do not match observations.

Energy feedback can be provided by SN explosions, stellar winds or AGNs. Stellar feedback alone is not strong enough to affect massive galaxies, while AGN feedback could be. However the latter has been incorporated in simulations only recently (from ∼2005) and only crude recipes have been realized at the moment (e.g., Springel et al., 2005; Sijacki and Springel, 2006; Booth and Schaye, 2009; Teyssier et al., 2011).

Feedback can be implemented in two different forms: thermal and kinetic feedback. The former has essentially the task of heating the gas and hinder the gas cooling, while the latter is implemented by actually giving “kicks ”to particles.

Several numerical codes can be found in literature with different implemented subgrid models. Scannapieco et al. (2012) performed a comparison between 13 codes that differ in the hydrodynamical part (SPH, moving mesh, AMR, cooling model, kinetic or thermal feedback) but share the same initial conditions, by resimulating the same galaxy, selected from the Aquarius project (Springel et al., 2008).

The main conclusions of the comparison were that state-of-the-art simulations cannot uniquely predict the properties of the baryonic component of a galaxy, even when the assembly history of its host halo is fully specified. In fact, all the 13 codes ended up with different physical properties of the same galaxy. Moreover, each simulation produced a wrong result, as every resimulated galaxy was overly massive, smaller and less gas-rich than typical spirals. This confirmed that star formation and final morphology strongly depend on the very uncertain subgrid prescriptions. A weak early feedback leads to a bulge dominated galaxy, while a stronger early

feedback produces a disk dominated galaxy (Zavala et al., 2008).
More recent implementations (Murante et al., 2015; Marinacci et al., 2014; Aumer et al., 2013) succeded in reproducing realistic disk galaxies using the same halo as in Scannapieco et al. (2012). This was achieved using very different subgrid implementations. If, on one hand, this is quite reassuring, since it tells us that the task is not impossible, on the other hand, it shows how degenerate the problem is and how little we are learning from this kind of approach to galaxy formation, where physical processes are treated with a lot of freedom.

4.3 Our simulation

The simulation used for this thesis was performed using the GADGET-3 (GAlaxies with Dark matter and Gas intEracT) code, a non-public improved version of the code GADGET-2 (Springel, 2005), which uses a TreePM gravity solver algorithm and the gas dynamics is computed with smooth particle hydrodynamics (SPH).
The improved version includes a more efficient domain decomposition to improve the work-load balance over GADGET-2.
The Plummer-equivalent softening length[1] for gravitational forces is set to $\epsilon = 2.08$ kpc comoving for the evolution up to $z = 2$. The softening is then held fixed at $\epsilon = 0.69$ kpc in physical units from $z = 2$ to $z = 0$.
Two cosmological volumes of size $L_{box} = 18\ h^{-1}$ Mpc comoving are evolved from $z = 199$ up to $z = 0$ with periodic boundary conditions. Each volume uses $N_{part} = 2 \times 256^3$ particles in the initial condition, half of which are DM particles and half are gas particles. DM and gas particle masses are $m_{DM} = 2.68 \times 10^7$ $M_\odot$ and $m_{gas} = 5.36 \times 10^6$ $M_\odot$ respectively.
The two boxes differ in the baryonic interaction prescriptions governing star formation (SF) and stellar/supernovae (SN) feedback. One simulation is described in Barai et al. (2015), from where I used the run E25cw. The other one is very similar to the run M25std from Barai et al. (2015), but with slightly different stellar yields and feedback parameters: $f_{b,out} = 0.2$, $f_{b,kin}$=0.5, P_{kin}= 0.02 (the parameters $f_{b,out}$, $f_{b,kin}$ and P_{kin} will be described in the next subsection). Two different sub-resolution models were adopted: the MUPPI model (MUlti-Phase Particle Integrator; Murante et al., 2010, 2015) in run M25std, and the Effective Model (Springel and Hernquist, 2003) in run E25cw, whose main features are described in the following subsections.

[1]The softening length ϵ defined in 4.1. The Plummer potential refers to a particular model for gravitational potential distribution in a spherical halo of matter. It is used to "soften "gravity at small distance scales.

In both models I:

- consider energy feedback driven by SNe;
- do not consider AGN feedback;
- adopt SF models with metal-dependent cooling;
- assume the gas is dust-free, optically thin and in photoionization equilibrium, heated by a uniform photoionizing background (CMB plus the Haardt and Madau (2001) model for the UV/X-ray);
- use the chemical enrichment and stellar evolution model by Tornatore et al. (2007), which is briefly described below in Section 4.3.1.

A flat ΛCDM model is used with the following parameters: $\Omega_{M,0} = 0.24$, $\Omega_{\Lambda,0} = 0.76$, $\Omega_{B,0} = 0.04$, $H_0 = 72$ km s^{-1} Mpc^{-1}.

4.3.1 Chemical enrichment and the stellar evolution model

The GADGET-2 code by Springel (2005) has a very simple model for chemical enrichment. It considers, in fact, a radiative cooling only by a primordial gas composition and a feedback contribution only by SNII expected by a Salpeter Initial Mass Function (IMF) using global stellar yields.
Tornatore et al. (2007) improved this model by:

- including the contribution of SNII, SNIa and AGB stars to the chemical enrichment and considering different stellar yields for each population;
- taking into account the age of different stellar populations, in order to release mass and energy over different timescales for different star masses;
- considering different IMFs, in order to check their effect on both stellar population and diffuse gas.

In this model, each star particle is treated as a Simple Stellar Population (SSP), that is an ensemble of coeval stars having the same metallicity. The information needed to calculate the evolution of each SSP (birth time, mass and initial metallicity) is carried by each star particle.
Since the star particle is born, at every time-step it is possible to compute how many

stars are dying as SNII and SNIa and how many are undergoing an AGB phase. It is assumed that SNIa arise from stars belonging to binary systems and having a mass in the range 0.8-8 $M_\odot$ (Greggio and Renzini, 1983), while SNII explode from stars with mass M> 8 $M_\odot$. AGB stars contribute only to the metal production, and so to the mass release, but not to the energy feedback, and they are classified as those stars in the mass range 0.8-8 $M_\odot$, which do not turn into SNIa.
The production of 11 chemical elements (H, He, C, Ca, O, N, Ne, Mg, S, Si, Fe) is followed. For each chemical element, the equation that represents its evolution $\dot{\rho}_i(t)$ is given by:

$$\begin{aligned}\dot{\rho}_i(t) = &- \psi(t)Z_i(t)+ \\ &+ A\int_{M_{Bm}}^{M_{BM}} \varphi(m)\left[\int_{\mu_{min}}^{0.5} f(\mu)\psi(t-\tau_{m2})p_{Z_i}(m,Z)d\mu\right]dm+ \\ &+ (1-A)\int_{M_{Bm}}^{M_{BM}} \psi(t-\tau(m))p_{Z_i}(m,Z)\varphi(m)dm+ \\ &+ \int_{M_L}^{M_{Bm}} \psi(t-\tau(m))p_{Z_i}(m,Z)\varphi(m)dm+ \\ &+ \int_{M_{BM}}^{MU} \psi(t-\tau(m))p_{Z_i}(m,Z)\varphi(m)dm\end{aligned} \tag{4.3}$$

The first term is the product between the SFR and the initial metallicity of the element i and represents the rate at which an element is subtracted from the ISM by the SF process and is locked up in stars.
The second term represents the rate at which an element is restored into the ISM by SNIa, for which it is assumed a single degenerate scenario (i.e., only one star of the binary system is a white dwarf which explodes in a SNIa event). A is the fraction of stars in binary systems which can be progenitors of SNIa events and it is set to the value $A = 0.1$, in order to match observations (Greggio and Renzini, 1983; Matteucci and Greggio, 1986). $\varphi(m)$ is the IMF, $p_{Z_i}(m, Z)$ is the stellar yield, which gives the mass of the element i produced by a star of mass m and initial metallicity Z and τ_{m2} is the stellar lifetime. The inner integral accounts for all possible mass ratios $\mu = m_2/(m_1 + m_2)$, where m_1 and m_2 are the masses of the primary and secondary star of the binary system, respectively. $f(\mu)$ represents the distribution function for the mass fraction of the secondary star and it has the following functional form: $f(\mu) = 2^{1+\gamma}(1+\gamma)\mu^\gamma$, with $\gamma = 2$, which is derived from statistical studies in the

solar neighborhood (Matteucci and Recchi, 2001). The integral is made over the mass range M_{Bm} =3 $M_\odot$ and M_{BM} =16 $M_\odot$, which represents the total masses of binary systems able to produce Type Ia SNe in the framework of the single degenerate scenario.
All the other terms describe the enrichment by single stars in different mass ranges, where M_L and M_U are the minimum and maximum mass of a star, which are set to 0.1 $M_\odot$ and 100 $M_\odot$, respectively.
Adopted stellar yields p_{Z_i} are taken from: Thielemann et al. (2003) for Type Ia SN, (Woosley and Weaver, 1995) for Type II SN and (van den Hoek and Groenewegen, 1997) for AGB stars.
Stellar lifetimes are taken from Padovani and Matteucci (1993) and are given by the formula:

$$\begin{aligned} \tau(m) &= 10^{[(1.34-\sqrt{1.79-0.22(7.76-log(m))})/0.11]-9} \quad for \quad m \leq 6.6 M_\odot \\ &= 1.2 m^{-1.85} + 0.003 \quad \text{otherwise} \end{aligned} \tag{4.4}$$

A multi-slope stellar IMF by by Kroupa et al. (1993) in the range [0.1-100] $M_\odot$ is used, which is defined as:

$$\begin{aligned} \phi(m) &= m^{-1.7} \quad m \geqslant 1 \quad M_\odot \\ &= m^{-1.2} \quad 0.5 \leq m \leq 1 \quad M_\odot \\ &= m^{-0.3} \quad m \leq 0.5 \quad M_\odot \end{aligned} \tag{4.5}$$

The enriched material is spread among the neighbouring gas particles using the SPH kernel function to compute weights. Metal cooling is implemented using the prescriptions of Wiersma et al. (2009).

4.3.2 The MUPPI Model

In the MUPPI model, whenever a gas particle's density is higher than a threshold value n_{thr} = 0.01 cm^{-3} and its temperature is below the threshold T_{thr}=5 $\times$ 10^4 K, it enters a multi-phase regime. The multi-phase gas particle is composed of a hot and a cold phase in thermal pressure equilibrium ($n_c T_c = n_h T_h$), plus a virtual stellar component. The masses of these three components are indicated as M_h, M_c and $M_\star$, respectively.
The temperature of the cold phase is kept fixed at T_c = 1000 K, while the hot phase T_h is computed from the particle's entropy. The number densities of the cold and hot component n_c and n_h are computed from their filling factors f_c and f_h, which are given by:

$$f_c = 1 - f_h = \frac{1}{1 + \frac{F_h}{F_c} \cdot \frac{\mu_c}{\mu_h} \cdot \frac{T_h}{T_c}} \tag{4.6}$$

where F_h and F_c are the fractions of cold and hot gas mass ($F_h + F_c = 1$) and μ_h and μ_c are the corresponding molecular weights. Then:

$$n_c = \frac{\rho F_c}{f_c \mu_c m_p} \tag{4.7}$$

with ρ being the average gas density of the particle.

A fraction of the cold gas, f_{mol}, is considered to be in the molecular phase. It is the reservoir of the material available for star formation. It is computed following the observed relation by Blitz and Rosolowsky (2006) between the ratio of molecular to atomic gas surface densities and the external pressure exerted on molecular clouds. The external pressure is the mid-plane pressure of a thin disk composed of gas and stars in vertical hydrostatic equilibrium. In the MUPPI model, the hydrodynamical pressure of gas particles is used as a measure of the external pressure. This enables us to derive the following simple relation for computing f_{mol}:

$$f_{mol} = \frac{1}{1 + P_0/P}. \tag{4.8}$$

Here P is the pressure of the gas particle and P_0 is the pressure at which half of the cold gas is molecular and is set to the value $P_0/k_B = 35000$ K cm^{-3} (Blitz and Rosolowsky, 2006).

The star formation rate is directly proportional to f_{mol} and is given by this equation:

$$\dot{M}_{SF} = f_\star \frac{f_{mol} M_c}{t_{dyn}}. \tag{4.9}$$

Here $f_\star$ is the star formation efficiency and t_{dyn} is the dynamical time, $t_{dyn} = \sqrt{3\pi/32 G n_c}$.

It is important to highlight that in this star formation prescription, SF is dependent on disk pressure. Thus no Schmidt-Kennicutt relation is imposed in the MUPPI model. Rather, as demonstrated in Monaco et al. (2012), the Schmidt-Kennicutt relation is naturally recovered from the model.

Mass and energy exchanges between the three gas phases (hot, cold, stellar) are described by a set of equations. When a gas particle enters the multi-phase, all the particle's mass is assigned to the hot phase. Then, matter flows among the three phases in the following way: cooling deposits hot gas into the cold component; evaporation, happening under the action of hot SN bubbles, brings cold gas back to the hot phase; SF deposits mass from the cold phase into the stellar component;

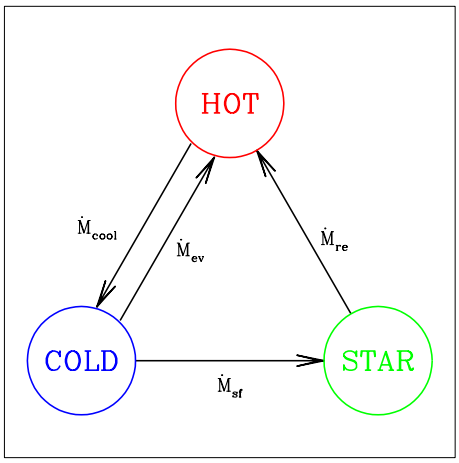

Figure 4.2: Illustrative representation of the different phase coexisting in a single gas particle, as it enters into the multiphase regime, and the corresponding mass flows. Figure taken from Murante et al. (2010).

mass restoration from dying stars moves mass from the stellar component back to the hot phase.
Energy feedback from SN is transferred to gas particles both in the form of thermal and kinetic energy. Thermal energy is given to the hot phase, which is lost by cooling and acquired from SN explosions.
Mass and energy exchanges are regulated by:

$$\begin{aligned} \dot{M}_\star &= \dot{M}_{SF} - \dot{M}_{re} \\ \dot{M}_c &= \dot{M}_{cool} - \dot{M}_{SF} - \dot{M}_{ev} \\ \dot{M}_h &= -\dot{M}_{cool} + \dot{M}_{re} + \dot{M}_{ev} \\ \dot{E}_h &= \dot{E}_{heat,local} - \dot{E}_{cool} + \dot{E}_{hydro} \end{aligned} \tag{4.10}$$

as represented also in Fig. 4.2. The cooling flow $\dot{M}_{cool}$ is given by:

$$\dot{M}_{cool} = \frac{M_h}{t_{cool}} \tag{4.11}$$

Cooling time is computed using the hot density and temperature.
The evaporation $\dot{M}_{ev}$ is assumed to be proportional to the SF, so:

$$\dot{M}_{ev} = f_{ev} \cdot \dot{M}_{SF} \tag{4.12}$$

where f_{ev} is a free parameter of the model. $\dot{M}_{re}$ is computed by chemical model by Tornatore et al. (2007). $\dot{E}_{heat,local}$ represents the contribution of SN energy from stars formed within the multiphase particle and is given by:

$$\dot{E}_{heat,local} = E_{SN} \cdot f_{fb,local} \cdot \frac{\dot{M}_{SF}}{M_{\star,SN}} \tag{4.13}$$

where E_{SN} is the energy supplied by a single supernova and $M_{\star,SN}$ is the associated stellar mass associated, while $f_{fb,local}$ is again a free parameter of the model and represents the fraction of SN energy that is deposited in the hot phase. The model assumes to have one SN event per $M_\star = 120\ M_\odot$.
$\dot{E}_{cool}$ represents the energy radiated away and it is described by:

$$\dot{E}_{cool} = \frac{E_h}{t_{cool}} \tag{4.14}$$

The last term in energy exchange equation, $\dot{E}_{hydro}$, takes into account the energy received from neighbouring particles. In fact, while a fraction of this energy is given to the local hot phase to sustain the high temperature of the particle itself, the remaining energy is redistributed to the hot phase of neighbouring gas particles within its SPH smoothing length and lying in a bi-cone of aperture $\theta = 60°$. The bi-cone axis is aligned along the least resistance direction of the gas density. This is to simulate the explosion of SN bubbles. The computation of the energy budget that is redistributed to neighbouring particles is given by:

$$\Delta\dot{E}_{heat,out} = E_{SN}\dot{f}_{fb,out} \cdot \frac{\Delta M_\star}{M_{SN,local}} \tag{4.15}$$

Kinetic feedback is implemented in the following manner. When a particle exits from the multi-phase regime, it is assigned a probability P_{kin} to become a wind particle. Then, it can receive kicks from neighbouring gas particles for a given time t_{wind}. The kinetic energy available for feedback from a single gas particle is a fraction $f_{b,kin}$ of the energy of a single SN. It is distributed to neighbouring wind particles in a cone within the gas particle's SPH smoothing length in a similar manner as for the thermal feedback. For each wind particle, the total kinetic energy available from all neighbouring kicking gas particles is first computed, as described above. Then the wind particle's kinetic energy is increased by this total amount. The velocity vector of the wind kick is oriented by energy-weighting among all the kicking particles.
Unlike other feedback prescriptions in the literature (Oppenheimer and Davé, 2008; Schaye et al., 2010; Springel and Hernquist, 2003), the MUPPI model depends only on the local properties of the gas. The mass-loading factor or the velocity of the wind are not input parameters of the feedback model. However these quantities can be estimated empirically as described in Murante et al. (2015).
A new star particle is produced following the stochastic star formation algorithm of

f_{re}	f_{ev}	$f_\star$	$f_{fb,local}$	$f_{fb,out}$	$f_{fb,kin}$	P_{kin}
-	0.1	0.02	0.02	0.2	0.5	0.02

Table 4.1: Parameters of MUPPI used in this thesis work.

Springel and Hernquist (2003). A multi-phase gas particle undergoing SF is turned into a collisionless star particle whenever a random number drawn uniformly from the interval [0,1] falls below the probability

$$P = \frac{M_p}{m_\star}\left[1 - exp\left(-\frac{\Delta M_\star}{M_p}\right)\right]. \tag{4.16}$$

Here M_p is the gas particle mass (hot mass + cold mass + stellar mass), and $\Delta M_\star$ is the cold gas mass transformed to stellar mass in a single SPH time step. The mass of the star particle, $m_\star$, is defined as $m_\star = M_p/N_g$ with N_g being the number of generations of stars per gas particle. With N_g set equal to 4, $m_\star$=1.34 $\cdot$ 10^6 $M_\odot$. A gas particle stays in the multi-phase regime until its density reaches a value equal to 1/5 of the threshold density n_{thr} or lower densities. If the energy feedback is incapable to sustain the hot phase resulting in hot phase temperatures that stay lower than 10^5 K, the particle is forced to escape from the multi-phase regime.
The implemented parameters used in this thesis work are summarized in Table 4.1.

4.3.3 The Effective Model

In the Effective model, a multi-phase gas particle is composed of a hot and a cold phase in thermal pressure equilibrium. Gas particles enter a multi-phase regime whenever their density is higher than a threshold value ρ_{SF} = 0.13 cm^{-3}. This threshold is a SF density threshold, as SF prescription is not based on the Blitz and Rosolowsky (2006) relation. It depends only on the cold gas mass, which is directly converted into stars on a characteristic timescale, given by the formula:

$$\dot{M}_{SF} = \frac{M_c}{t_\star} \tag{4.17}$$

where $t_\star = t_{\star,0} \cdot \sqrt{\rho/\rho_{SF}}$. A value of $t_{\star,0}$ = 2.1 Gyr was chosen by Springel and Hernquist (2003) in order to fit the Kennicutt relation.
Mass and energy exchanges between the hot and cold gas phase are regulated by similar physical processes as in the MUPPI section, that is star formation, cloud evaporation due to supernovae and cloud growth due to cooling. With respect to the

original model by Springel and Hernquist (2003), the simulation used in this thesis work includes additional subgrid physics, that is : metal-dependent radiative cooling and heating by a photoionization background; model coupling with the chemical enrichment and stellar evolution model by Tornatore et al. (2007).
Star particles are generated from gas particles using the stochastic scheme introduced by Katz et al. (1996).
Energy feedback is given both in the form of thermal and kinetic energy. Differently from the MUPPI model, the two forms of feedback do not consider any distribution of the energy to neighbouring particles in a cone within the SPH smoothing length simulating the blowout of a SN bubble. Thermal feedback in the form of thermal heating and cloud evaporation is implemented.
Kinetic feedback uses the prescriptions of the *energy-driven wind* scenario with a constant wind velocity. The wind mass-loss rate is given by this formula:

$$\dot{M}_w = \eta \dot{M}_{SF} \tag{4.18}$$

where η is the mass loading factor, which is set to $\eta = 2$. A fixed fraction χ of the SN energy is converted into wind kinetic energy:

$$\frac{1}{2}\dot{M}_w v_w^2 = \chi \epsilon_{SN} \dot{M}_{SF}. \tag{4.19}$$

Here v_w is the wind velocity and ϵ_{SN} is the average energy released by SN for each $M_\odot$. So we have:

$$v_w = \sqrt{\frac{2\chi\epsilon_{SN}}{\eta}} \tag{4.20}$$

In the adopted run, I use a fixed value $v_w = 350$ km s^{-1}. Gas particles are given wind kick using a probabilistic approach (see Equation 10 in Barai et al. 2013 for details). Their velocity v is incremented according to:

$$v' = v + v_w \hat{n} \tag{4.21}$$

where $\hat{n}$ is the direction of the wind, preferentially chosen along the rotation axis of spinning objects.

Chapter 5

Comparison between observations and simulations

The main goal of this thesis work is to characterize the properties of the IGM around galaxies at high redshift, in order to study the galaxy/intergalactic medium interplay. As already said in Chapter 1, there is a cosmic cycle of baryons between galaxies and IGM, which is important to understand in a cosmological context.
In this thesis, I focus on analysing a sample of simulated galaxies and the environment around them using two different numerical simulations, which are described in Chapter 4. These two simulations were chosen as they share the same gravity solver algorithm, the same box size (18 Mpc h^{-1} comoving), the same number of gas and dark matter particles (N = 2 $\times$ 256^3), the same chemical enrichment and stellar evolution model by Tornatore et al. (2007), but strongly differ in both the star formation and feedback prescriptions.
The goal is to test different subgrid schemes in order to better understand the chemical properties of the environment around galaxies and, in particular, in order to quantify the physical scales up to which present-day observed absorption systems can be found. In fact, galaxy/absorber relations suffer from the bias of being flux-limited, so a proper derivations of the physical distances between these two components cannot be derived correctly, as the less luminous galaxies can be missed.
In this Chapter, I will present the results of this thesis work, the methods used to derive them and the observational data used to compare with.

5.1 Observational data set

Data for the comparison with the C IV (and also Si IV) mock spectra are taken from Kim et al. (2016). This data set is chosen because it represents a state-of-the-art, homogeneous and statistically significant sample of high resolution absorption lines. The sample consists of 23 QSOs in the redshift range $2 \lesssim z \lesssim 3.5$, which were observed with the VLT/UVES (21 spectra) and Keck/HIRES (2 spectra) instruments. Spectra were first presented in the following papers: Kim et al. (2004), Kim et al. (2007), Kim et al. (2013) and Boksenberg and Sargent (2015).
Spectral resolution is $R \sim 45000$ (~ 6.7 km s^{-1}), while typical S/N per pixel are of the order of 30$\sim$50 for the Lyα forest and $\sim$100 for the C IV region.
H I and C IV absorption lines detected in all the QSO spectra are in the redshift range $1.5 \lesssim z \lesssim 3.3$.
Data points, used for comparison with simulations in Section 5.4, are integrated column densities values representing H I and C IV *systems*, as defined in Kim et al. (2016). Precisely, the QSO spectra by Kim et al. (2016) are fitted using the VPFIT code[1] (Carswell and Webb, 2014), which performs a Voigt profile fitting of the spectrum. An absorption feature is fitted by the code by decomposing it in single Voigt profile components and by minimising the χ^2. The output of the fit consists of the physical parameters, such as the column density, the redshift and the Doppler parameter, of the single fitted components.
Then, C IV and H I *system* are constructed with this procedure. Column densities of C IV single Voigt absorption components, found in each spectrum, are integrated within $\pm$150 km s^{-1} from C IV flux minimum. This defines a C IV system. If the C IV absorption extends over $\pm$150 km s^{-1} or when two different absorption systems are found to lie within $\pm$150 km s^{-1} but they are spread at >150 km s^{-1} or <150 km s^{-1}, then the velocity range is extended by another 100 km s^{-1} in order to include all the C IV absorption.
The *associated* H I system is given by the integration of all the single H I Voigt single components in the same velocity range as the C IV system. With this working definition, the C IV centroid does not necessarily coincide with the H I centroid and there is no evidence that C IV and H I systems are physically connected. This definition is more related to volume-averaged quantities, commonly used in numerical simulations.
As reported by Kim et al. (2016), the range of the velocity integration is chosen according to some observational findings: a strong clustering signal is found within

[1] http://www.ast.cam.ac.uk/ rfc/vpfit.html

200 km s^{-1} in close QSO pairs (Rauch et al., 2005). In D'Odorico et al. (2006) an HI clustering signal is found on transverse velocity separation of $\sim$500 km s^{-1}. Moreover, the average velocity dispersion of galaxies at high redshift is of the order of $< \sigma > \sim$ 120 km s^{-1} (Erb et al., 2006). Finally, it is demonstrated in Kim et al. (2016), that the N_{CIV} vs N_{HI} relation converges when considering velocity integration ranges greater than 70 km s^{-1}.
In order to be consistent with data, I used the same velocity integration range in the analysis of the simulated absorption systems.
For the comparison with the constructed covering fractions, I compared instead with the observational samples of Rubin et al. (2015), Landoni et al. (2016) and Prochaska et al. (2014). Landoni et al. (2016) and Prochaska et al. (2014) use QSO pairs, that is they use the light of a background QSO to study the gaseous envelope of a QSO host galaxy.
The sample of Prochaska et al. (2014) consists of QSO pairs, whose spectra were taken mainly from the BOSS survey or obtained with the Keck/LRIS instrument, with impact parameters in the range 39 kpc$<$ b $<$1 Mpc and redshifts 1.8$<$ z $<$3.5. QSO pairs by Landoni et al. (2016) were taken from the SDSS survey and have impact parameters smaller than b $<$200 kpc and redshifts 2.0$<$ z $<$2.8.
Rubin et al. (2015) use,instead, QSO pairs to study the diffuse gas in the CGM of 40 DLAs, that is the primary sightline probes an intervening DLA system in the redshift range 1.6$<$ z $<$3.6, while the secondary sightline is used to look for a C IV absorption at the same redshift of the DLA, up to a distance of the order b$<$ 300 kpc.

5.2 Method

In order to interpret the observed data, I have built a set of simulated data, which I processed in a way as close as possible to the one adopted for the observations. First of all, I have built simulated mock spectra and then I constructed absorption systems and computed their column densities. I give details of those operations in the following subsections.

5.2.1 Constructing mock spectra in the simulation

Simulated data are obtained by piercing through the cosmological box with lines of sight, either randomly or forcing them to have impact parameters less than a certain value around a given galaxy or position in the simulation.

Lines of sight are as long as the box side and are always parallel to it along one of the three directions $x - y - z$.
Each line of sight is divided in 2048 pixels of $\Delta L \sim 10$ kpc each. Along each line of sight I can compute different quantities, such as the density profile of the total gas or of a particular chemical element, the temperature profile, the gas peculiar velocity or the optical depth profile of a given chemical element.
Profiles are computed following the prescriptions by Theuns et al. (1998): the total gas density ρ of each pixel i is the sum of the densities of all gas particles $\rho_{\rm part}$ convolved with their SPH kernel functions W, that means that all the gas particles j contribute to the pixel's density; these particles have a smoothing length h which intersect the line of sight. The density of a gas particle is defined as $\rho_{\rm part} = M_p/h^3$. The same procedure is applied to compute the other physical quantities, such as the gas peculiar velocity or the temperature.

$$\begin{aligned} \rho_i &= \sum_j W_{ij} \\ v_i &= \sum_j v_{part,j} W_{ij} \\ T_i &= \sum_j T_{part,j} W_{ij} \end{aligned} \tag{5.1}$$

Here, W_{ij} is:

$$\begin{aligned} W_{ij} = \rho_{part} \cdot W(q_{ij}) &= \rho_{part} \cdot \left[\frac{1}{4\pi}(4 - 6q_{ij}^2 + 3q_{ij}^3) \right] \quad , if \quad q_{ij} \leq 1 \\ &= \rho_{part} \cdot \left[\frac{1}{4\pi}(2 - q_{ij})^3 \right] \quad , if \quad 1 \leq q_{ij} \leq 2 \\ &= 0 \quad , otherwise \end{aligned} \tag{5.2}$$

with

$$q_{ij} = \frac{jx(i) - x(j)j}{h} \tag{5.3}$$

$x(i)$ is the pixel's position and $x(j)$ is the particle's position.
I can also compute density profiles of a given chemical species in a given ionization state.
The metallicity of a specific chemical element in a single gas particle is defined as the ratio between the mass of that element in the gas particle and the total mass of the particle, such as:

$$Z_X = m_X/M_p \tag{5.4}$$

with X=[H, He, C, Ca, O, N, Ne, Mg, S, Si, Fe]. In order to have the fraction of that element in a particular ionization state k for a specific gas particle, I used the

formula:

$$f_{X,k} = f_{X,k,\odot} \cdot Z_X \tag{5.5}$$

$f_{X,k,\odot}$ is the fraction of an element X in the ionization state k per solar metallicity. Given the density, the temperature and the redshift of the particle, $f_{X,k,\odot}$ is computed using the CLOUDY code[2] (Ferland et al., 2013) with the UV background by Haardt & Madau (2005) [3]. For the H I, f_{HI} is an output of the simulation and, as described in Section 4.3, it is computed considering a UV background by Haardt and Madau (2001), which is not so different from Haardt & Madau (2005) at $z \sim 2$. Defining $\rho_{X,k} = f_{X,k} \cdot \rho_{part}$ and using this quantity in place of ρ_{part} in equation (5.2), I can compute all the profiles of equation (5.1) but for specific ions.
Optical depths along lines of sight were computed by considering their density, temperature and velocity in each pixel. I consider a pixel i and first calculate the central optical depth of the line, which falls in that pixel, using its density and temperature with this formula:

$$\tau_{0,i} = \frac{\sigma_\alpha c}{\sqrt{\pi}} \frac{\rho_i \Delta L}{b_i} \tag{5.6}$$

with $b_i = \sqrt{\frac{2K_B T_i}{m_{atom}}}$ and $\sigma_\alpha = (3\pi\sigma_T/8)^{1/2} f \lambda_0$, where $\sigma_T = 6.625 \times 10^{25}$ cm^{-2} is the Thomson cross-section, f is the transition oscillator strength and λ_0 is the rest-frame transition wavelength.
According to the Voigt profile line shape, neighboring pixels q will suffer absorption from pixel i by an amount $e^{-\tau_q}$, where:

$$\tau_q = \tau_{0,i} \cdot exp\left\{ -\left[\frac{v_q - v_i}{b_i} \right]^2 \right\} \tag{5.7}$$

The number of pixels q that will suffer absorption from pixel i is set to be equal to $3b_i \Delta v_L$, where Δv_L is the length of a pixel in velocity, so depending on temperature of pixel i.
Shifting pixel by pixel, I can repeat the same operation along all the line of sight, summing each new contribution to the optical depth in a pixel to what was previously computed a number l of times, depending on the temperature of neighboring pixels. In this way, the optical depth in one pixel is the sum of the contribution from pixels l, depending on their temperature and density, and itself.
I can also construct τ-weighted density or temperature profiles. Focusing only on

[2] http://www.nublado.org/
[3] The UV backgrounds could be obtained from http://www.ucolick.org/ pmadau/CUBA/HOME.html

density, I define:

$$\rho_{\tau,q} = \frac{\sum_l \rho_i(l) \cdot \tau_i(l)}{\sum_l \tau_i(l)} \tag{5.8}$$

where $\rho_{\tau,q}$ is the τ-weighted density in a given pixel q, $\rho_i(l)$ is the density of an adjacent pixel i, considering only its contribution and not by its own adjacent pixels, and $\tau_i(l)$ the optical depth contribution to pixel q by pixel i given by the Eq. 5.7, that is the contribution to pixel q is given by the wings of the Gaussian profile whose central contribution is given by pixel i. The sum is over a number l of pixels, as defined as before.

5.2.2 Measuring simulated column densities: integrating τ-weighted density profile versus AOD method

In the regime of high resolution spectroscopy, observed parameters of absorption systems, such as the b-parameter or the column density, can be derived using Voigt profile fitting codes, such as VPFIT. Observed absorption lines contain the information of gas peculiar motions and thermal broadening, so, in order to compare with them, it is important to take into account redshift space distortions also in the simulation. For this reason, it is obvious that I can not just integrate the real gas density profile along the line of sight, because, in this way, I am not considering the gas that produced an absorption in a given point of redshift space.
One possibility could be to use optical depth weighted quantities, as described in Schaye et al. (1999). As illustrated in their Figs. 3-4, absorption line minima correspond to peaks in the τ-weighted density profile and the τ-weighted density measured in the line centre is proportional to the column density measured by the VPFIT code. Using τ-weighted density profiles, I do not lose the information about gas peculiar motions, but calculating column densities integrating this density profile is not correct either.
To address this issue, I pierced through the cosmological box 1000 random lines of sight and I obtained C IV spectra. I post-processed the C IV spectra adding instrumental noise and rebinning to the spectral resolution of observational data. I chose a spectral resolution of 6.7 km s^{-1} and S/N =100 . I also rescaled all the fluxes by a factor ≈0.44 in order to match the effective optical depth by Kim et al. (2007).
These spectra were then fitted by VPFIT. I discarded all the spectra having single components fitted with column densities smaller than log(N)=12.06 and errors on b and N greater than 50%. The first condition is due to the fact that many spectra show no C IV absorption, but VPFIT attempts to fit the spectra anyway by putting

a small component. The threshold of 12.06 is our chosen value to discard all false detections. Applying this condition only 369 spectra are left.
I then constructed *absorption systems* trying to be as consistent as possible with the procedure by Kim et al. (2016). With an algorithm similar to the "Friends-Of-Friends ", I identify an absorption system as a group of single components that lie within $\pm$ 150 km s^{-1} of each other along the line of sight. The condition "any friend of a friend is a friend"is valid, that is, starting from one component, I identified all the components lying within $\pm$ 150 km s^{-1} of this first one. Then I moved to the second closest component and I repeated the operation. If new friends (new with respect to the first considered component) are identified, they are added to form a unique system with the first one, and so forth with all other components satisfying this algorithm. This scheme was chosen in order to translate in an automatic way the procedure by Kim et al. (2016) and, in particular, the fact that, when considered necessary, they decide by eye to extend the velocity range of integration. Looking by eye each single spectrum and deciding which range of integration to take for every absorption system is not feasible when dealing with thousands and thousands of simulated spectra.
The column density of the group is the sum of the column densities of all the single components that form the system. I then determined a mean redshift of the group by weighting the redshifts of single components with their column density. I repeated the same procedure for constructing also H I absorption system. After that, I associated C IV and H I systems in this way: for every C IV system, I considered its mean redshift and I defined the velocity range of integration by extending $\pm$ 150 km s^{-1} from this mean redshift. Then, I looked for associated H I absorption systems by searching in the same spectra when the mean redshift of an H I group falls in the just defined velocity integration range.
At this point, I performed a comparison between column densities of absorption systems derived with the VPFIT code, as just described, and the ones derived by integrating in the same velocity range the τ-weighted density profile of the same spectra, not convolved with the instrumental response. In Fig. 5.1, I show this comparison. In the top panel, the VPFIT total column density of absorption systems, as defined above, found in the 369 spectra is shown on the x-axis, while on the y-axis the column density, in the same velocity range as VPFIT, of the same spectra calculated by integrating the τ-weighted density profile is reported. The orange line is the 1:1 ratio.
It is clear from the picture that there is a disagreement of one order of magnitude between the two determinations of the column density and this is due to the fact

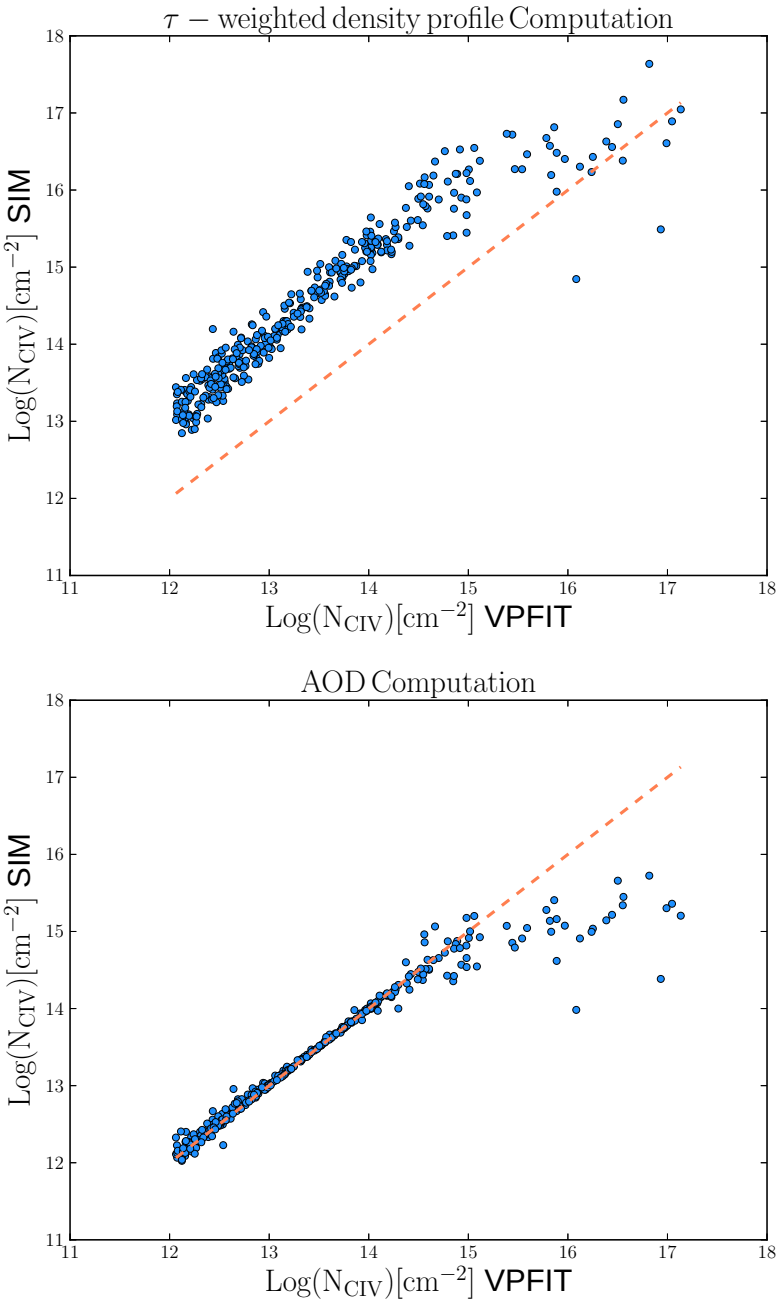

Figure 5.1: *Top* : Comparison between column densities derived with the VPFIT code and the ones derived by integrating the τ-weighted density profile of the same spectra and in the velocity range $\pm$ 150 km s^{-1} from VPFIT mean group redshift. The orange line is the 1:1 ratio. A disagreement of one order of magnitude is observed. *Bottom* : Comparison between column densities derived with the VPFIT code and the ones of the same spectra derived using the AOD method. The two values are the same. In both the panels the disagreement at high column densities (Log(N$_{CIV}$) $\gtrsim$ 15) is due to the fact that when lines become saturated, VPFIT is no more reliable in calculating column densities without higher order transitions.

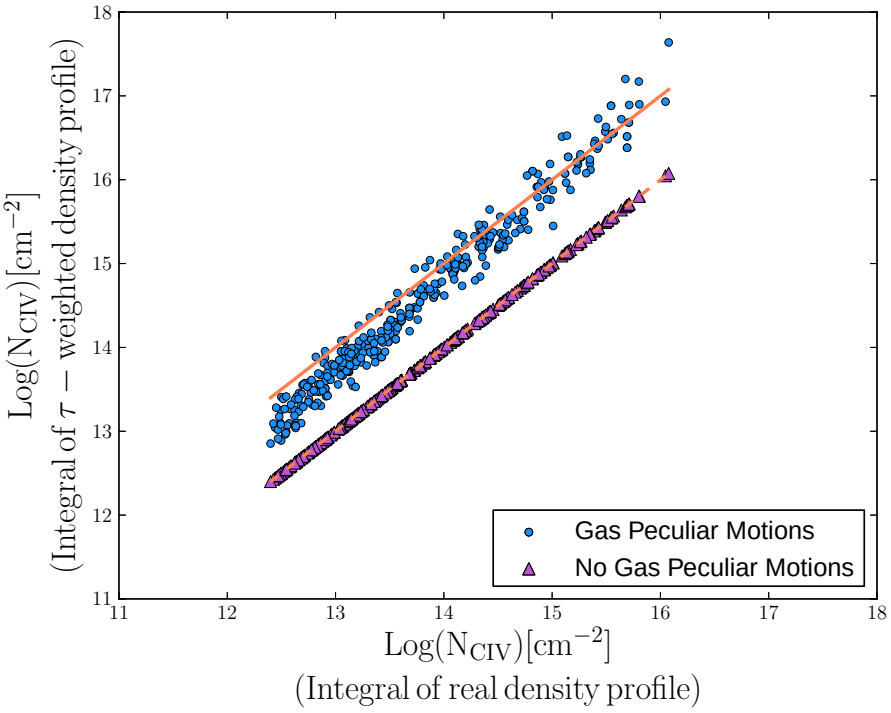

Figure 5.2: Integral along all the line of sight of the τ-weighted density profile versus the integral along all the line of sight of the real density profile, considering in the simulation gas peculiar motions (blue circles) or setting gas peculiar velocities to zero in the computation of the spectra profiles (purple triangles). The dashed orange line is the 1:1 ratio, while the solid one is the same line shifted above of one order of magnitude. When considering gas peculiar motions, the process of τ-weighting the density profile does not preserve the integral of the function and this explains the disagreement observed in the top plot of Fig. 5.1.

that the process of τ-weighting does not preserve the integral of the density function along the line of sight. This is the reason why using the τ-weighted density profile for estimating column densities is not correct, as shown in Fig. 5.2. I considered the τ-weighted density profile and the real one of the above mentioned 369 spectra. I computed the integrals of the two functions along all the line of sight. If the process of τ-weighting would have been just a replacement of the same gas in different parts of the spectra according to their peculiar velocities, maintaining the area of the function, the two integrals would have of course been the same. As it is clear from Fig. 5.2, there is instead a disagreement of one order of magnitude between the two integrals (blue circles), which explains also the disagreement of the top plot of Fig. 5.1.

I made a further check by setting gas peculiar velocities to zero before the spectra

computation and recalculating the two integrals (purple triangles). When gas peculiar velocities are ignored, the two integrals are of course the same.
Summing up, integrating real gas density profiles is not correct, because we are ignoring peculiar motions, which are present in observations. Considering a τ-weighted density profile, which preserves the information of peculiar motions, is not correct either, because the process of τ-weighting introduces an error in the integration. What was found by Schaye et al. (1999) is correct when speaking about the center of the line, but not when considering a finite velocity range.
I consequently decided to use the AOD method, described in Section 2.5 for estimating column densities. This method is often used dealing with observational data, because it provides a quick and reliable measure of the column density of unsaturated lines in a regime of high resolution spectroscopy. According to this method, an apparent optical depth can be converted into an apparent column density using the formulas 2.32-2.35.
From an observational point of view, this method is not reliable in presence of a saturated line, because the flux goes to zero which makes it impossible to recover the real optical depth. However, in the simulation I have the value of the true optical depth in each pixel, thus this method is correctly applicable in our case.
In a regime of high resolution spectroscopy, $\tau_a(v) \approx \tau_{true}(v)$, so for this reason, I used the simulated true optical depth profile along the line of sight not convolved with the instrumental response.
I performed the same comparison with the VPFIT code, so I integrated column densities derived with the AOD method in the velocity range defined by the mean redshift of the system, as explained before. Before the computation, I rescaled all the optical depth values in each pixel by the same factor ≈ 0.44, in order to be consistent with VPFIT.
The comparison is shown in the bottom panel of Fig. 5.1. The AOD method predicts the same column densities as VPFIT for C IV column densities lower than 10^{15} cm^{-2}. The AOD method has the advantage of being much faster than the Voigt profile fitting, thus I adopted it to determine the column density of the absorptions in the simulated spectra.
In both panels of Fig. 5.1, the disagreement at high column densities ($\mathrm{Log}(\mathrm{N_{CIV}}) \gtrsim 15$) is due to the fact that, when lines become saturated, VPFIT is no longer reliable in estimating column densities in particular because only the strongest line of the C IV doublet is used in simulated spectra and the same is true for H I column density, for which no higher order transitions are used in addition to Lyα. My considerations refer to the part of the plot at low column densities. This is also the

reason why I did not use VPFIT directly on the simulation to compare with the data of Kim et al. (2016).

5.3 Selection of simulated galaxy sample

In order to investigate the IGM/CGM of galaxies, I selected from the snapshot at $z = 1.94$ of both cosmological runs two samples of 20 galaxies with a total halo mass M_h in the range $[\sim 10^{10} - 10^{12}]$ $M_\odot$, identified with the SUBFIND algorithm (Springel et al., 2001) and stellar mass greater than $M_* \gtrsim 2 \cdot 10^9 M_\odot$.
The selection criteria were the following: the galaxies had not to be on major merger's interactions and had to be the main halo of their FOF-group, so not a substructure, in order to compare similar conditions at a given distance from galaxy center between the different galaxies of the sample. The first condition puts an upper limit on the chosen halo mass, as only 6 objects with $M_h > 10^{12}$ $M_\odot$ are in the two runs, but they are actually all formed by clusters of merging galaxies. The lower limit on the halo mass, instead, is related to the number of particles that sample the galaxy and its various components, in order to consider the object reliable.
In Table 5.1, I report some properties of the two galaxy samples. Following the spherical-collapse model, virial radii are defined for each FOF-halo as the radii of a sphere centered on the main halo of the FOF-group and which contains an overdensity of 200 the critical density, so they are calculated with this formula:

$$R_{vir} = \left(\frac{M_h}{\frac{4}{3}\pi \cdot 200 \cdot \rho_{Crit}} \right)^{1/3} \tag{5.9}$$

with

$$\rho_{Crit} = \frac{3H(z)^2}{8\pi G} \tag{5.10}$$

I also visually selected from the two boxes, using the software GADGETVIEWER[4], 10 near-filaments environments, in order to investigate the low density IGM near galaxies.
In the first row of Fig. 5.3, a galaxy from the MUPPI simulation is shown, while in the second row I plot an example of a near-filament environment. In the left panels the H I maps around these two objects are reported, in the center the C IV maps and on the right I show the images of the two environments with GADGETVIEWER.
For near-filament environments, I choose as "center of the object " the position of the white cross, as shown in the bottom-left panel of Fig. 5.3.

[4]http://astro.dur.ac.uk/ jch/gadgetviewer/index.html

MUPPI MODEL				EFFECTIVE MODEL			
Obj.	M_h [$M_\odot$]	$M_\star$ [$M_\odot$]	R_{vir} [phys. kpc]	Obj.	M_h [$M_\odot$]	$M_\star$ [$M_\odot$]	R_{vir} [phys. kpc]
1	$6.87{\cdot}10^{11}$	$2.37{\cdot}10^{10}$	94	1	$5.04{\cdot}10^{11}$	$2.18{\cdot}10^{10}$	84
2	$4.03{\cdot}10^{11}$	$1.13{\cdot}10^{10}$	78	2	$4.91{\cdot}10^{11}$	$3.07{\cdot}10^{10}$	84
3	$4.02{\cdot}10^{11}$	$8.31{\cdot}10^{9}$	78	3	$4.90{\cdot}10^{11}$	$3.73{\cdot}10^{10}$	84
4	$3.63{\cdot}10^{11}$	$1.11{\cdot}10^{10}$	76	4	$4.11{\cdot}10^{11}$	$2.23{\cdot}10^{10}$	81
5	$2.74{\cdot}10^{11}$	$1.24{\cdot}10^{9}$	69	5	$3.66{\cdot}10^{11}$	$2.70{\cdot}10^{10}$	74
6	$2.60{\cdot}10^{11}$	$6.87{\cdot}10^{9}$	68	6	$3.04{\cdot}10^{11}$	$1.66{\cdot}10^{10}$	71
7	$2.08{\cdot}10^{11}$	$6.83{\cdot}10^{9}$	63	7	$3.00{\cdot}10^{11}$	$1.31{\cdot}10^{10}$	71
8	$1.66{\cdot}10^{11}$	$5.92{\cdot}10^{9}$	58	8	$2.39{\cdot}10^{11}$	$1.16{\cdot}10^{10}$	66
9	$1.43{\cdot}10^{11}$	$5.04{\cdot}10^{9}$	55	9	$2.32{\cdot}10^{11}$	$7.50{\cdot}10^{9}$	65
10	$1.06{\cdot}10^{11}$	$3.38{\cdot}10^{9}$	50	10	$2.12{\cdot}10^{11}$	$8.22{\cdot}10^{9}$	63
11	$9.49{\cdot}10^{10}$	$2.54{\cdot}10^{9}$	48	11	$9.91{\cdot}10^{10}$	$2.81{\cdot}10^{9}$	49
12	$9.22{\cdot}10^{10}$	$1.95{\cdot}10^{9}$	48	12	$9.66{\cdot}10^{10}$	$3.07{\cdot}10^{9}$	48
13	$9.12{\cdot}10^{10}$	$2.84{\cdot}10^{9}$	48	13	$9.40{\cdot}10^{10}$	$3.48{\cdot}10^{9}$	48
14	$8.91{\cdot}10^{10}$	$2.53{\cdot}10^{9}$	47	14	$9.01{\cdot}10^{10}$	$4.99{\cdot}10^{9}$	47
15	$8.21{\cdot}10^{10}$	$2.06{\cdot}10^{9}$	46	15	$8.95{\cdot}10^{10}$	$2.21{\cdot}10^{9}$	47
16	$8.14{\cdot}10^{10}$	$2.13{\cdot}10^{9}$	46	16	$8.93{\cdot}10^{10}$	$3.64{\cdot}10^{9}$	47
17	$8.10{\cdot}10^{10}$	$1.75{\cdot}10^{9}$	46	17	$8.25{\cdot}10^{10}$	$2.21{\cdot}10^{9}$	46
18	$8.05{\cdot}10^{10}$	$2.51{\cdot}10^{9}$	46	18	$7.78{\cdot}10^{10}$	$2.30{\cdot}10^{9}$	45
19	$7.79{\cdot}10^{10}$	$3.06{\cdot}10^{9}$	45	19	$7.77{\cdot}10^{10}$	$3.48{\cdot}10^{9}$	45
20	$7.36{\cdot}10^{10}$	$2.09{\cdot}10^{9}$	44	20	$3.73{\cdot}10^{10}$	$3.64{\cdot}10^{9}$	35

Table 5.1: Properties of the sample galaxies of the MUPPI Model Box and the Effective Model Box. In the first column of the two tables, there is the object ID; in the second column, the halo mass of the galaxy; in the third column, the stellar mass of the galaxy; in the fourth column, the virial radius of the galaxy in physical units.

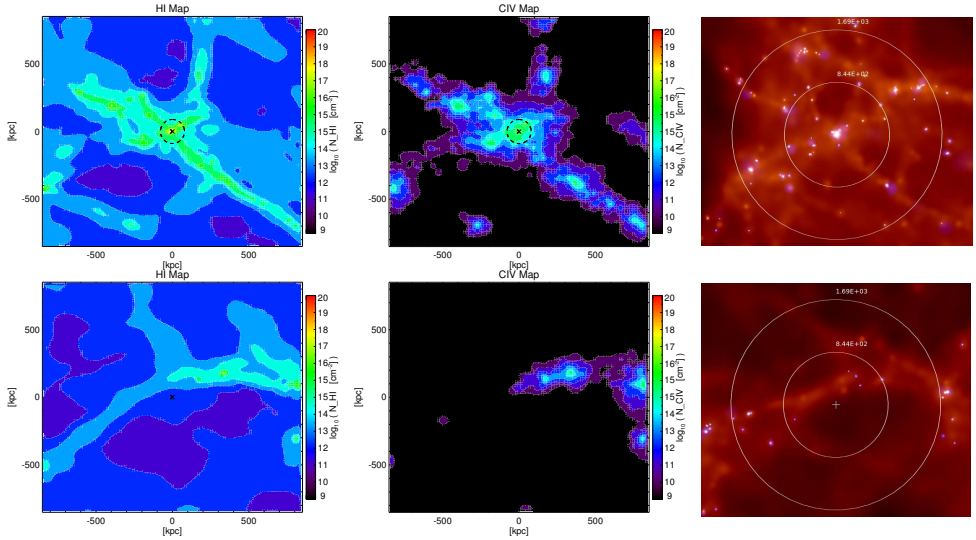

Figure 5.3: *Top*: Projected maps of the H I (left) and C IV (center) distribution around a particular galaxy of the sample. Column densities have been computed by integrating the density profile of these subboxes along a perpendicular slice of width ±300 kpc from galaxy's position. Image of the chosen galaxy (right) from *GadgetViewer*. *Bottom*: same as *top* but for a near-filament environment. The white cross here represents the visually-chosen "center of the object ".

5.4 Results

5.4.1 The N_{CIV} vs N_{HI} relation: piercing around galaxies

The N_{CIV} vs N_{HI} relation, constructed here in order to compare with data, is the observational equivalent to the theoretical overdensity-metallicity relation, as the overdensity is related to N_{HI} and the metallicity can be traced by the C IV doublets which fall in a region redward of the Lyα forest, free from line blendings, and observable in the optical band at $z \gtrsim 1.2$. Its ubiquitous presence in QSO spectra also indicates that it traces a gas phase, which is characteristic of many astrophysical gas environments.

I pierced through the cosmological boxes random lines of sight around the 40 galaxies with impact parameters less than 800 kpc, in order to characterize the environment around them.

As the line of sight is as long as the box side, I first identified the position of the center of the galaxy along it. I, then, selected a region along the line of sight ± 150 km s^{-1} from this position and I consider the optical depth profile both for H I and C IV in this region rescaled by a factor ≈0.44, as explained in Sec. 5.2.2. For each

pixel of this region, I converted the value of the optical depth into a column density using Eq. 2.34 and then I integrated.
In Fig. 5.4, I reported the N_{CIV} versus N_{HI} relation for the sample of the MUPPI galaxies, while in Fig. 5.5 the same relation but for the Effective Model box.

Each blue or cyan point refers to a single line of sight. Blue points refer to lines of sight around galaxies with a total halo mass between [$\sim 10^{11} - 10^{12}$ $M_\odot$] while cyan points refer to galaxies with a total halo mass in the range [$\sim 10^{10} - 10^{11}$ $M_\odot$]. Magenta points represent the observational sample by Kim et al. (2016) and the green line is the detection limit of this sample.
Lines of sight are divided according to their distance from the galaxy. Going from top-left to bottom-right, in each plot are grouped lines of sight with impact parameters b between [0-1] r_{vir}, [1-3] r_{vir}, [3-5] r_{vir} and $b > 5$ r_{vir}.
Going to larger distances, I can see that the bulk of the points gradually shifts to lower values of H I and C IV column densities. Inside the virial radius, all the simulated lines of sight are above the observational limit. Simulated points occupy a slightly different region than the data of Kim et al. (2016). This could be due to the fact that I am using a wrong UVB, as I am assuming that each gas particle is photoionized by Haardt & Madau UVB, neglecting that near galaxies there is also the contribution of the ionizing photons of the galaxy itself. For this reason, N_{CIV} could be lower, with part of C IV becoming actually C V. Another possible explanation could be that the simulation produces too many metals, due to inefficient feedback, that causes too much star formation. To investigate this last issue, I constructed the mass-metallicity relation for all the galaxies of the MUPPI box with stellar mass $M_* > 2 \times 10^9$ $M_\odot$. For each gas particle inside one tenth of the virial radius of a galaxy, I computed the abundance O/H. For each galaxy, I then took the gas particle's mass-weighted average value of O/H between all the previous calculations.
Our result are shown in Fig. 5.6. The simulation does actually produce too many metals with respect to the observed relation by Kacprzak et al. (2016) and this could explain the disagreement in the C IV data, although I think the assumptions on the UVB could still play a role.
Goz et al. (2017, in prep., private communication) also analysed the mass-metallicity relation of the MUPPI simulation, but at z=0. They compare the gas metallicity of their sample of MUPPI galaxies, taken from the same box I used, as a function of stellar mass, with the observational relation by Tremonti et al. (2004). They recover the same trend as the observed relation, but with a global offset of roughly $\sim$ 0.1-0.2 dex, extending up to 0.3 dex in the low-mass end of the relation. They claim

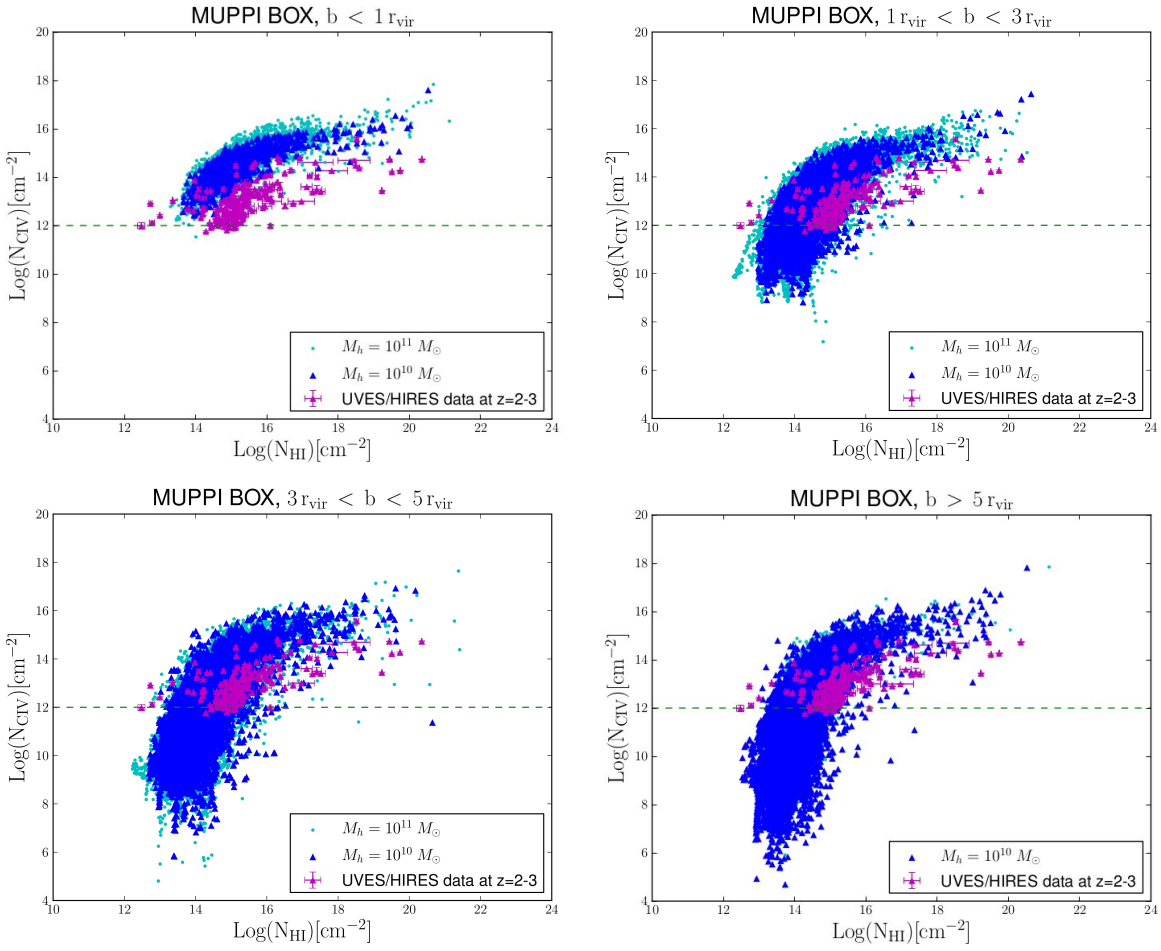

Figure 5.4: Each point refers to a single line of sight for the MUPPI simulation. *Cyan points*: lines of sights around halos with $M_h \sim 10^{11}$ $M_\odot$. *Blue points*: lines of sights around halos with $M_h \sim 10^{10}$ $M_\odot$. *Magenta points*: observational data from Kim et al. (2016) (the same data are reported in each panel). *Green line*: observational detection limit. Plots have been divided according to the distance of lines of sight from galaxy center in units of virial radius.

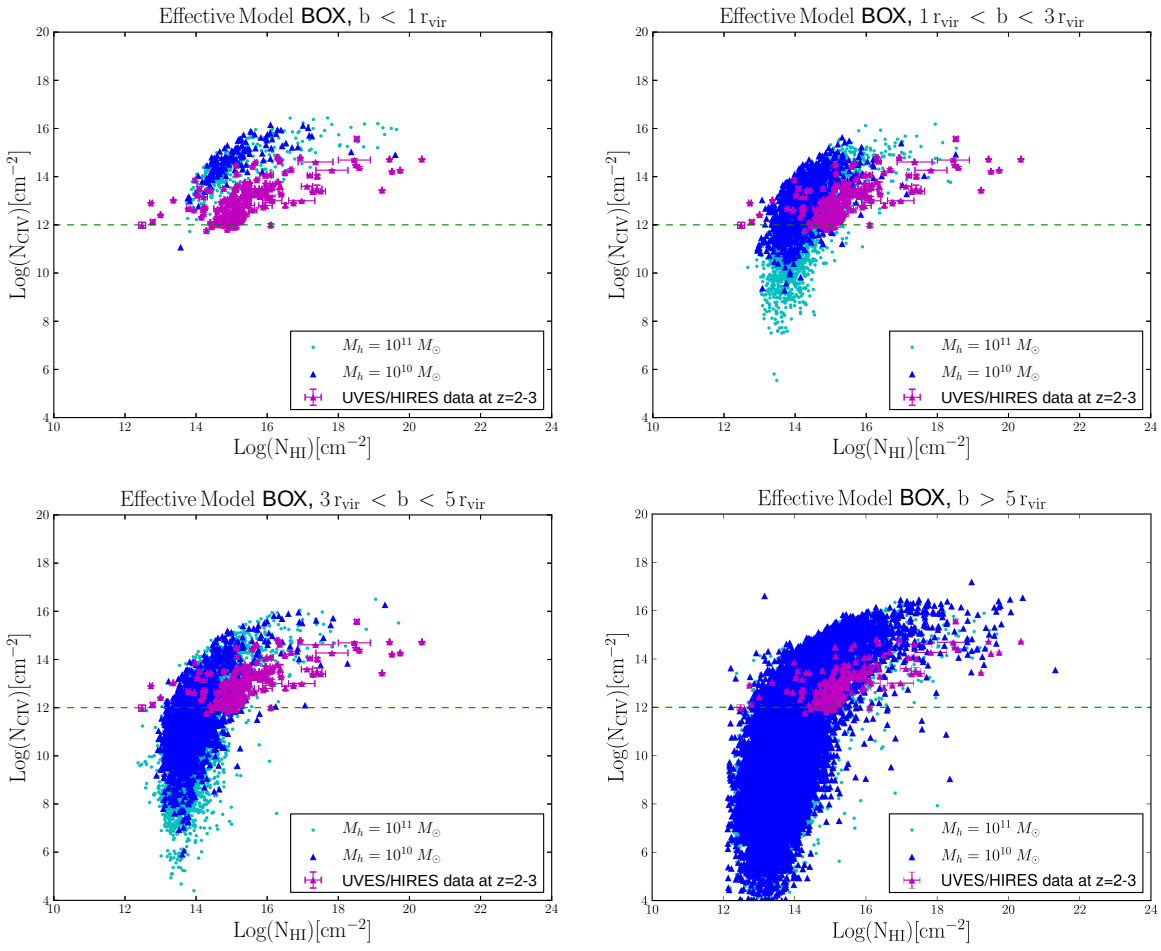

Figure 5.5: Each point refers to a single line of sight for the MUPPI simulation. *Cyan points*: lines of sights around halos with $M_h \sim 10^{11}$ $M_\odot$. *Blue points*: lines of sights around halos with $M_h \sim 10^{10}$ $M_\odot$. *Magenta points*: observational data from Kim et al. (2016) (the same data are reported in each panel). *Green line*: observational detection limit. Plots have been divided according to the distance of lines of sight from galaxy center in units of virial radius.

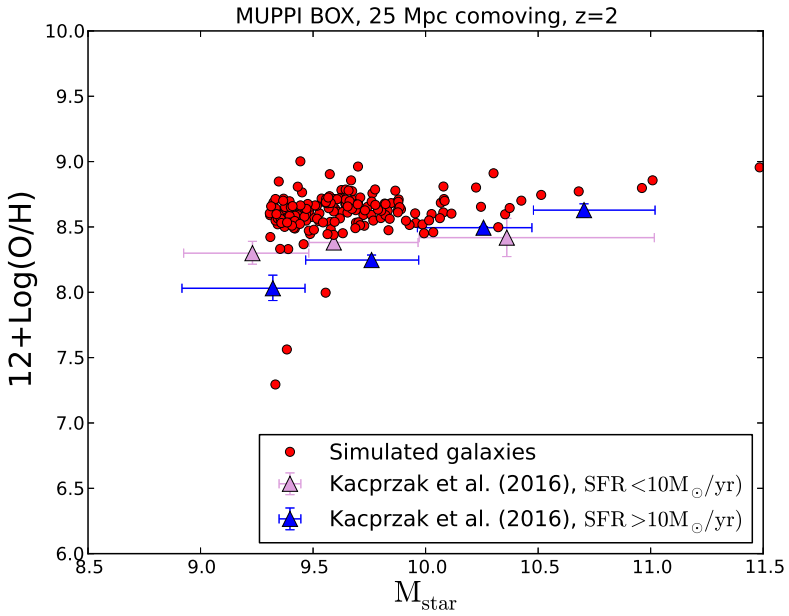

Figure 5.6: Mass metallicity relation for all the MUPPI galaxies with $M_* > 2 \times 10^9$ $M_\odot$ compared to the observed one by Kacprzak et al. (2016).

that this could be due to the lack of AGN feedback, capable instead of quenching the cooling and star formation.
Even if the bulk of the points shifts downwards at large distances, there are still points at high H I and C IV column densities. This could be a consequence of the fact that galaxies are not isolated systems.
I investigated the nature of these points by considering all the lines of sight of Fig. 5.4 with b $> 5\ r_{vir}$ and with absorption systems with $14.0 \leq \mathrm{Log}(\mathrm{N_{CIV}}) \leq 18.0$ [cm^{-2}]. I searched for substructures near the lines of sight and I computed the minimum distance from a line of sight to a substructure. The distribution of the distances is reported in Fig. 5.7. I estimated a median value and a 1σ error of 19^{+29}_{-11} kpc. This result suggests that those lines of sight are the ones hitting or passing close to the halos of other substructures. However, note that the search algorithm I used looks for dark matter substructures, so some of them could be simply gas clumps without star formation.

For completeness, the median values with the 1 σ error of the distance distributions in the ranges b $< 1\ r_{vir}$, $1\ r_{vir} <$ b $< 3\ r_{vir}$ and $3\ r_{vir} <$ b $< 5\ r_{vir}$ are 15^{+12}_{-8} kpc, 19^{+18}_{-11} kpc and 19^{+21}_{-11} kpc respectively. The total mass of the substructure is in the range $[10^8 - 10^{12}\ M_\odot]$. In Figs. 5.8 and 5.9, I show the Probability Distribution Functions (PDFs) of the points of Figs. 5.4 and 5.5 for the MUPPI model and the Effective Model respectively. The plots reflect the same distance division as the

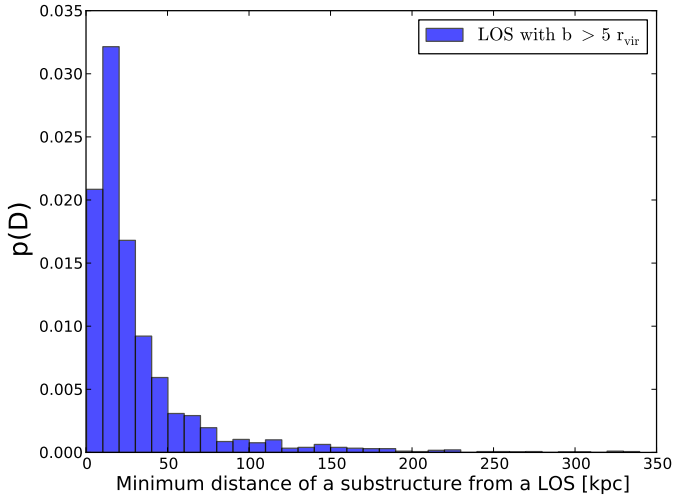

Figure 5.7: Probability distribution function of the minimum distance between a line of sight (LOS) with b $> 5\ r_{vir}$ of an absorption system with $14.0 \leq \mathrm{Log(N_{CIV})} \leq 18.0$ [cm^{-2} and a dark matter substructure identified with SUBFIND. No distinction in the mass of substructures has been done.

previous ones. The orange line represents the observational detection limit.
These plots constitute the main result of the thesis and they give the probability to find an absorption system with a given H I and C IV column density at a certain distance from a galaxy. I can state that observational data have the highest probability to be confined in a region up to 3-5 virial radii from galaxies.
This result is validated by the fact that I do not recover any strong difference between the MUPPI and the Effective models. They show very similar trends. Only in the range 1 r_{vir} < b < 3 r_{vir} , I see that the MUPPI Model has a higher probability to find absorption systems with large column densities with respect to the Effective model for H I column densities in the range [10^{13}-10^{15} cm^{-2}] and this could be due to a more efficient feedback with respect to the Effective model, which is not capable to spread metals with the same strength.
As surveys are flux-limited, faint galaxies can be missed. For this reason, I can state from Fig. 5.7-5.8-5.9 that finding a strong absorption system at a high distance from a galaxy it could be possible and the two can be related to each other, but it is more probable that there is a smaller galaxy, which is not observed and to which the absorption system is related.
In Fig. 5.10, I performed a comparison between halos of different masses in our sample. I did not find any strong trend.
I repeated the same procedure for near-filament environments, by piercing through

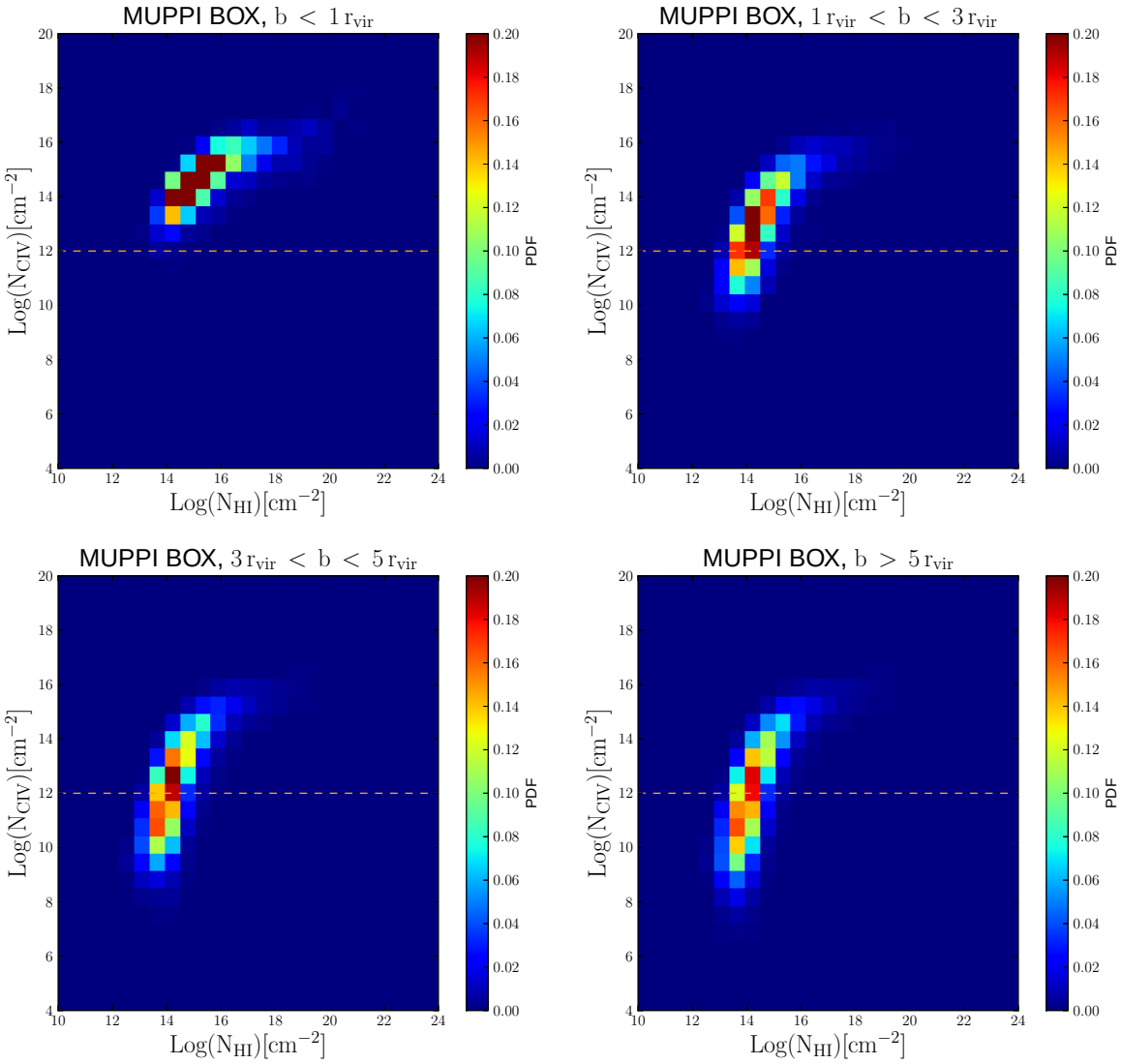

Figure 5.8: Probability Distribution Function (PDF) of points in Fig. 5.4. The orange line is the observational detection limit.

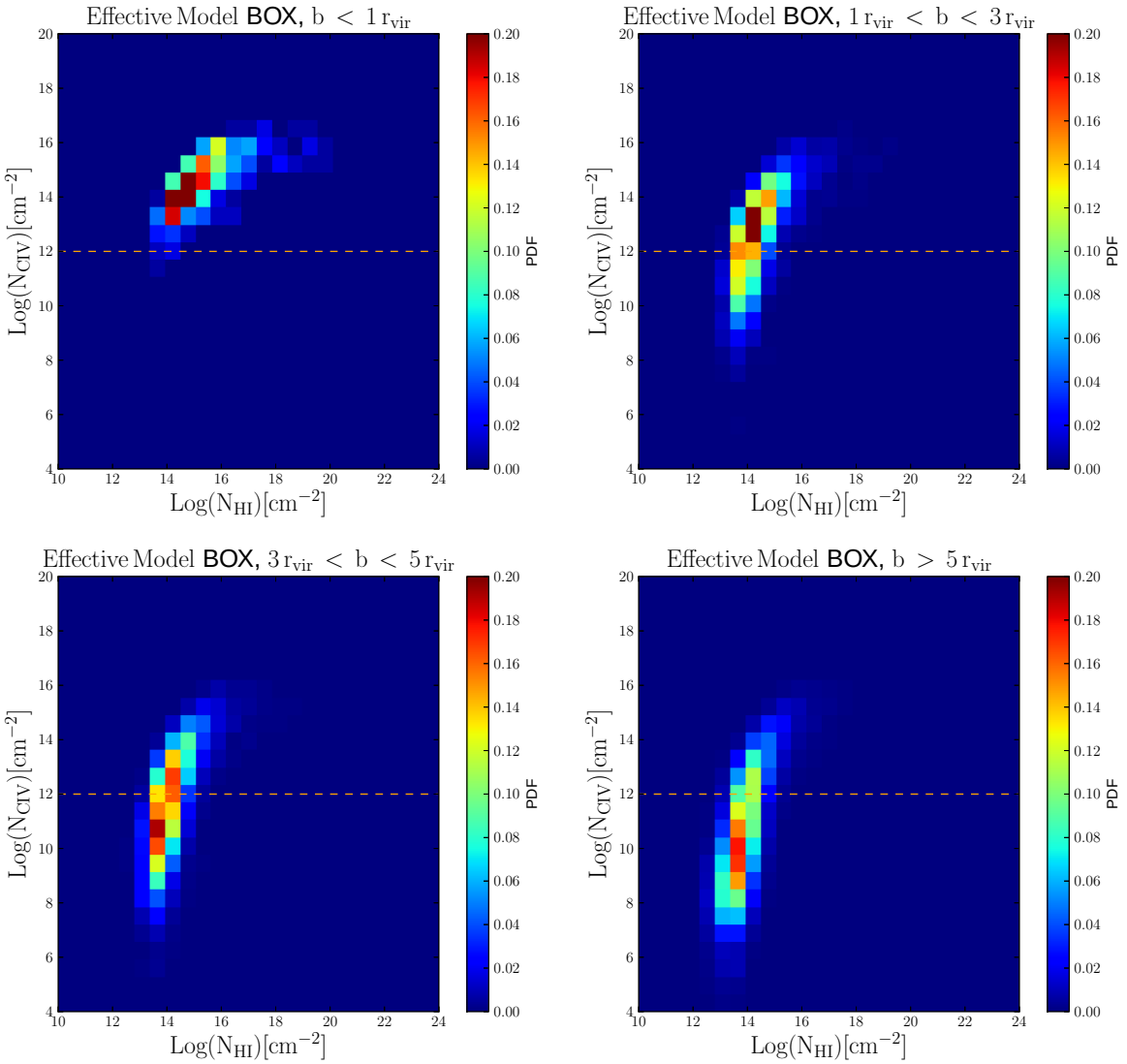

Figure 5.9: Same as Fig. 5.8, but for the *Effective Model* simulation.

the cosmological box random lines of sight around the chosen "center "of near-filament environments with impact parameter less than 800 kpc. In Fig. 5.11, it is shown the probability distribution function for near-filament environments. Plots are divided according to their physical distance from the given center.
For each radial bin, the bulk of the points has the highest probability to have values of the C IV and H I which are below the detection limit. The tail of the PDF above the detection limit could be due to the presence of halos near the chosen "center "of a near-filament environment.

5.4.2 The N_{CIV} vs N_{HI} relation: median values in concentric regions

I performed also another kind of analysis, based more on a statistical point of view. I took lines of sight of Sec. 5.4.1 and for each object, I divided lines of sight according to their distance from the center of the object: going from 0 to 800 kpc, I divided the spatial region considered in radial bins of size $\sim$ 10 kpc and I grouped lines of sight in each bin according to their impact parameter.
For each object, I computed the mean and the 1-σ error of the integrated N_{CIV} and N_{HI} values of all the lines of sight in each bin.
I report this modified N_{CIV} versus N_{HI} relation for the MUPPI model and the Effective Model in Figs. 5.12 and 5.13.
For each galaxy, I divided the mean values according to their distance from galaxy center, so plotting mean values whose radial bin is at a distance from center between [0-1] r_{vir}, [1-3] r_{vir} , [3-5] r_{vir} and r $>$ 5 r_{vir}. Galaxy color coding is the same as Sec. 5.4.1.
For near-filaments environments, it is obviously not possible to define a virial radius, so I plotted in each panel of Figs. 5.12-5.13 the mean values of all the radial bins from 0 to 800 kpc.
Large error bars, representing the 1-σ error, are due to the fact that the medium is not homogeneous, so at same radial distance I could find a low-density environment, having low column densities, or I could hit (or be close to) a substructure, having higher values of column densities.
As in the previous section, I can see that for galaxies median values shift to lower column densities as the distance increase and I do not find any correspondence between simulated and observational data above 3-5 r_{vir} except for the weakest systems of the sample of Kim et al. (2016). Near-filaments points are confined to a region under the detection limit, suggesting that they have metallicities too low to be probed by

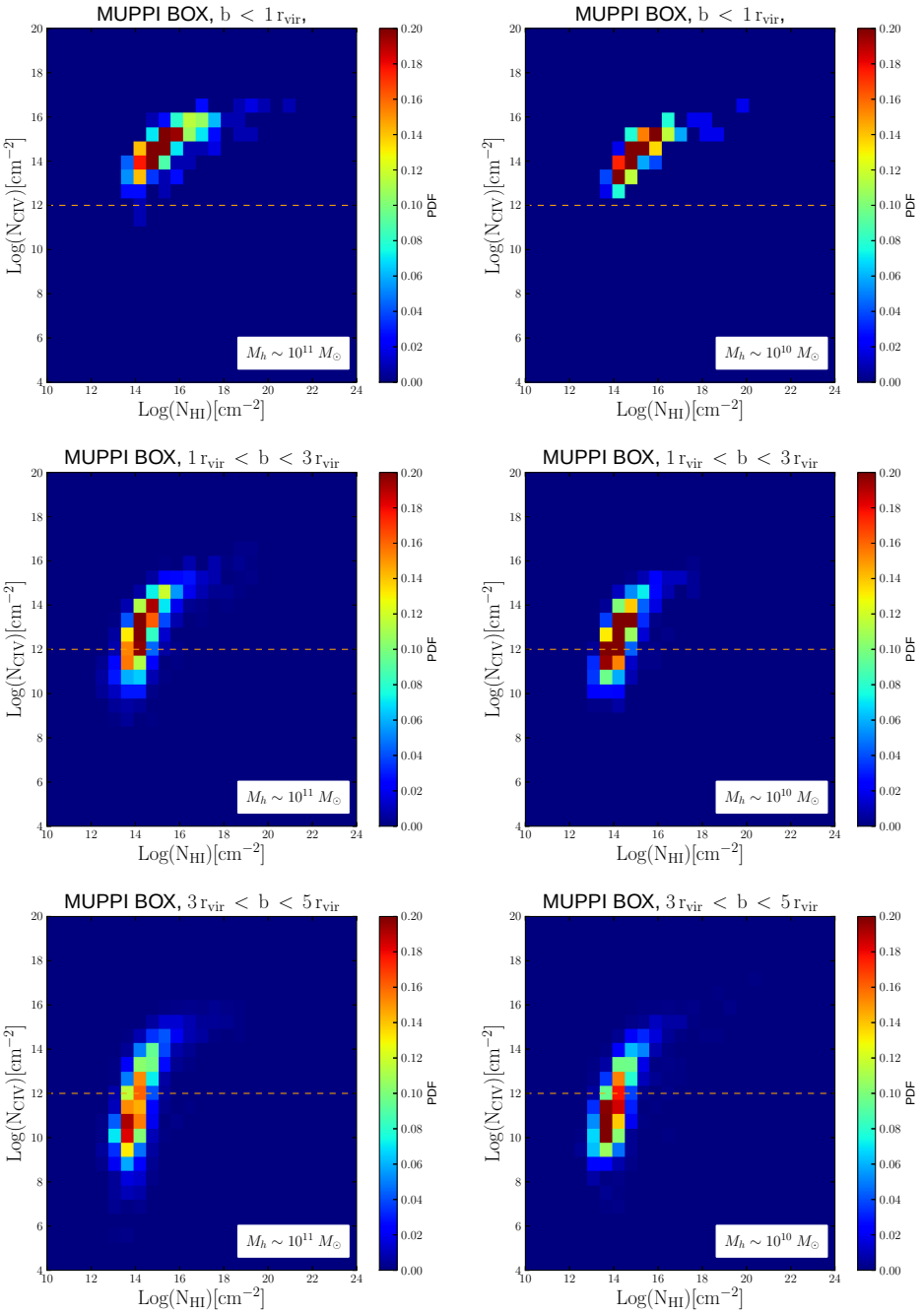

Figure 5.10: *Left* : Probability Distribution Function (PDF) of points related to halos with $M_h \sim 10^{11}$ $M_\odot$ of Fig. 5.4. *Right* : Probability Distribution Function (PDF) of points related to halos with $M_h \sim 10^{10}$ $M_\odot$ of Fig. 5.4.

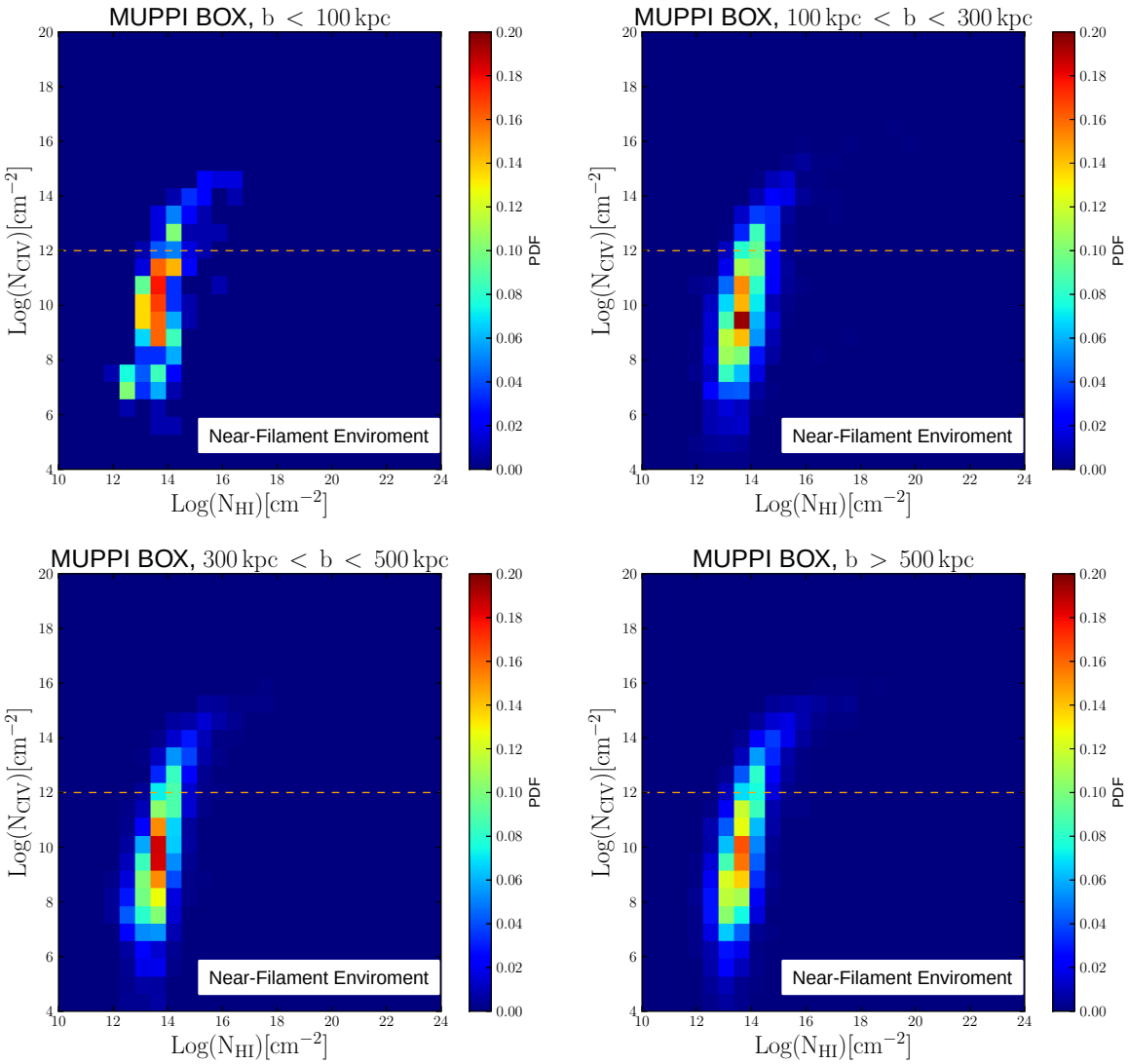

Figure 5.11: Probability Distribution Function (PDF) of points related to near-filaments environments of the MUPPI simulation.

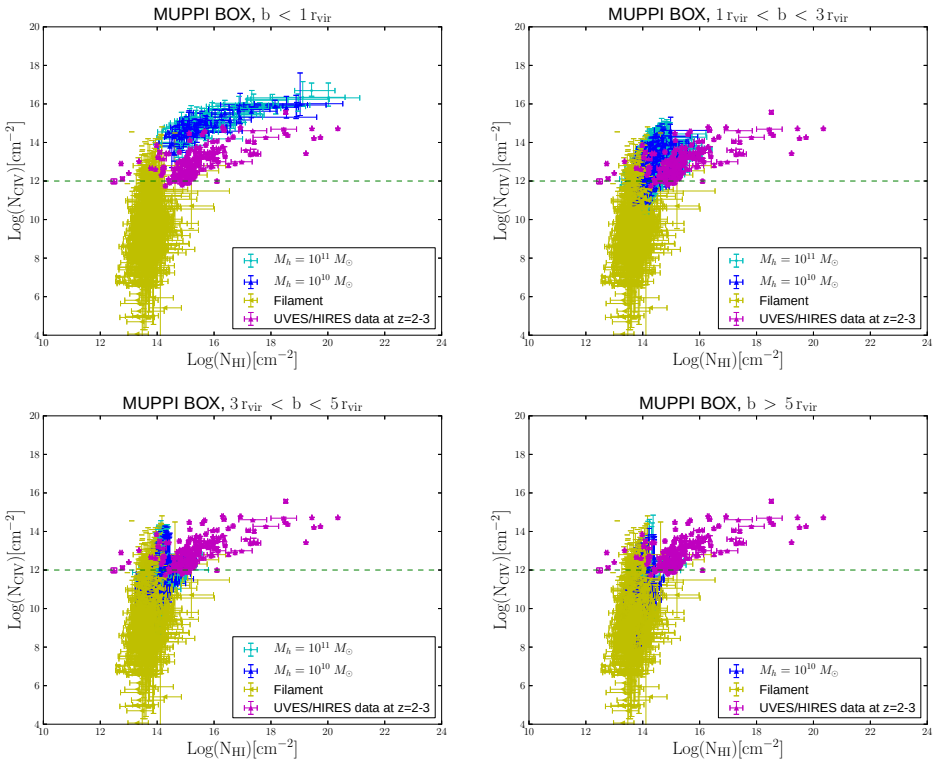

Figure 5.12: Each point is the spherical average value of H I and C IV column densities profiles in radial bins of width of $\sim$ 10 kpc around the 30 objects for the MUPPI simulation. *Cyan points*: mean values of lines of sights around halos with $M_h \sim 10^{11}$ $M_\odot$. *Blue points*: mean values of lines of sights around halos with $M_h \sim 10^{10}$ $M_\odot$. *Yellow points*: mean values of lines of sights around near-filaments points. *Magenta points*: observational data from Kim et al. (2016) (the same data are reported in each panel). *Green line*: observational detection limit. Plots have been divided according to the distance of radial galaxy spherical averages from galaxy center in units of virial radius. This division does not concern near-filaments points, whose al values are reported in each plot.

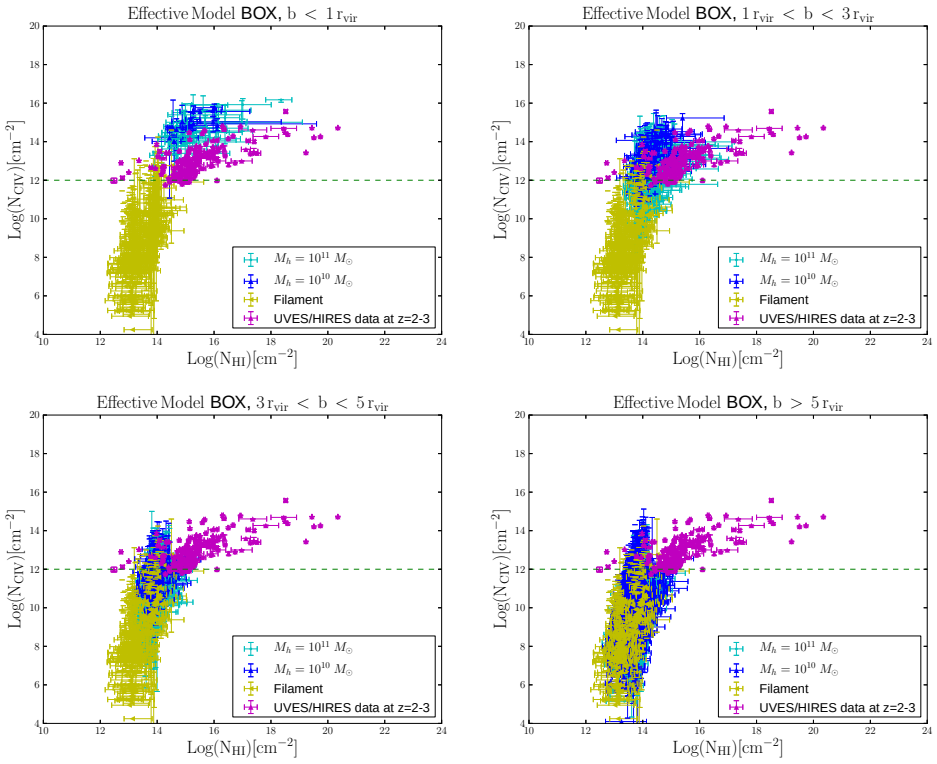

Figure 5.13: Same as Fig. 5.12, but for the *Effective Model* simulation.

present day observations. In the future, high resolution spectrographs like HIRES at the E-ELT could enter this interesting regime of weak absorbers.

5.4.3 The N_{OVI} vs N_{HI} and N_{SiIV} vs N_{HI} relations: extending the comparison between the two subresolution models

As already stated, the subresolution models do not show strong differences in the results.

To better investigate this last issue, I performed the same overall analysis with two other ions: O VI and Si IV. The results are shown in Figs. 5.14- 5.17. Like for the C IV, I do not find any strong differences between the two models.

For O VI I do not have any available data, but the simulated O VI shows a similar trend to C IV, with the main difference between the two subresolution models in the range 1 r_{vir} < b < 3 r_{vir}. I interpret this last point as a result of the less effective feedback in the Effective Model with respect to the MUPPI one.

For the Si IV, I compared always with the observational sample by Kim et al. (2016). This time, I do not see any difference between the models in every radial bin. Si IV traces a gas phase at higher N_{HI}, closer to galaxies. At these close distances to

galaxies, the effects of the feedback could not be traced.
One explanation of these results could be that the differences in the feedback prescriptions of the two models could be more related to the thermal feedback than to the kinetic one. Figs. 5.18 shows a temperature map around the same galaxy for both models, where the temperature profile along parallel lines of sight has been integrated ±300 kpc. It is clear that the MUPPI model is more capable of heating the surrounding gas with respect to the Effective model, while the differences related to kinetic feedback, that is how metals are distributed outside galaxies, are less visible. Barai et al. (2015) already studied the difference between different feedback schemes, among which the ones used in this thesis work. In their paper, they constructed radial profiles of the total gas metallicity around galaxy centers at $z \sim 2$ and they inferred that the MUPPI model distributes metals more adequately than the Effective model. I do also recover a slight difference between the two models in the range $1\ r_{vir} < b < 3\ r_{vir}$, but when comparing with observational data, these differences seem not to significantly impact in the IGM properties investigated here. It is important to highlight, as already said in Chapter 4, that the MUPPI simulation, that I used, was run with slightly different model parameters, due to small changes in the chemical sector with respect to the one by Barai et al. (2015).

In Figs. 5.19, I show a comparison for a particular galaxy between column density maps for H I, C IV, O VI and Si IV calculated with the AOD method as previuosly done, so taking into account gas peculiar motions.
Also by looking at the distributions of the gas around the galaxy for each element, I do not see any strong difference between the two models.

5.4.4 Covering fractions

The covering fraction is by definition the ratio between the number of lines of sight showing an absorption system with an equivalent width greater than a threshold value and the total number of lines of sight. In practice, it is a measure of the clumpiness of the medium. If the medium is perfectly homogeneous, the covering fraction is equal to 1. The clumpier the medium, the lower the covering fraction is. In Fig. 5.20, I report the covering fraction for our sample of MUPPI data, calculated in bins of 100 kpc, in which I computed equivalent widths by always integrating ± 150 km s^{-1} from galaxy position along the line of sight.

Dashed and dot-dashed lines are the median values of the covering fraction of our total sample of lines of sight for two different threshold values of the equivalent

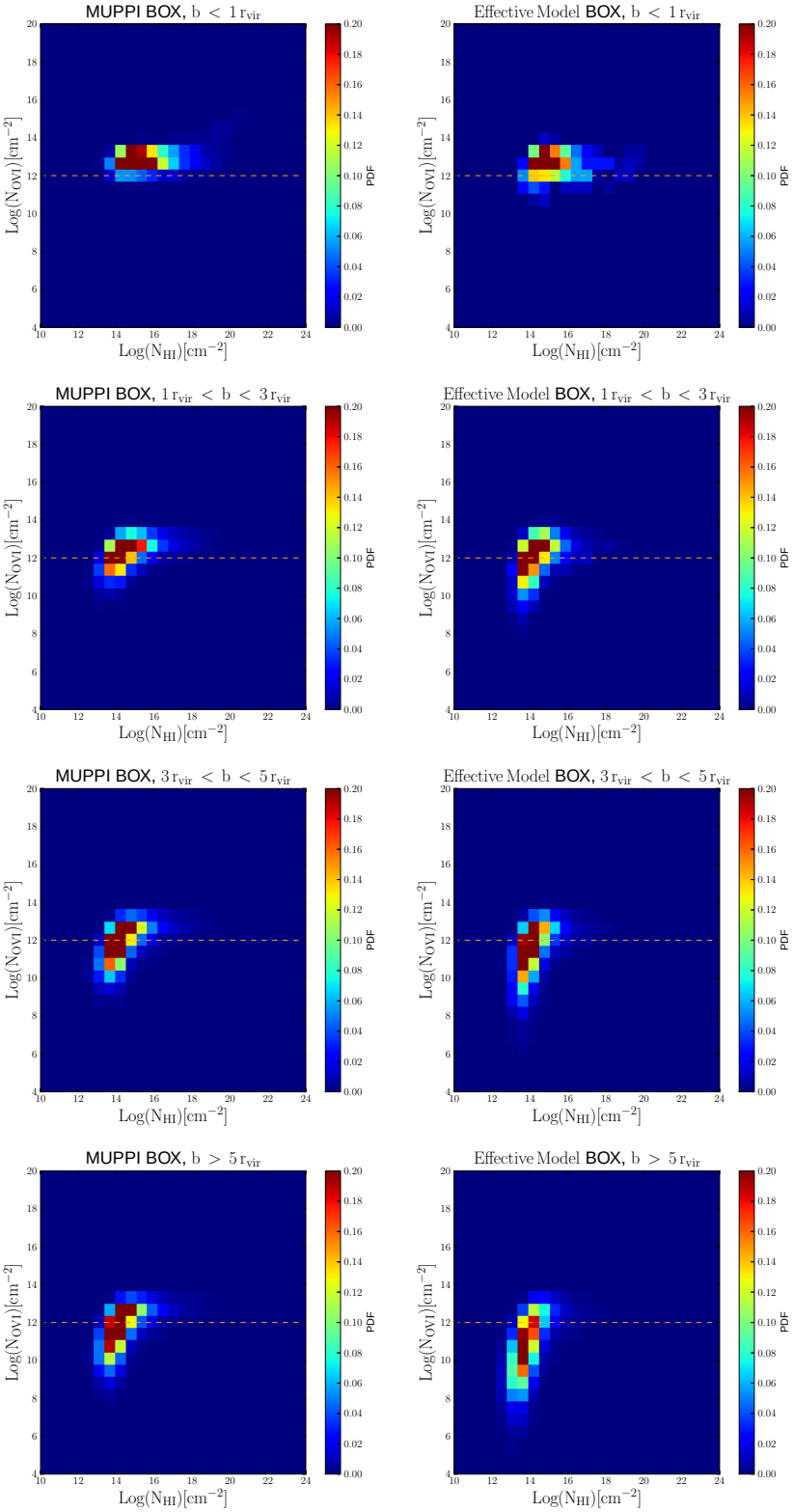

Figure 5.14: (OVI):PDF of lines of sight around the sample of galaxies.

.

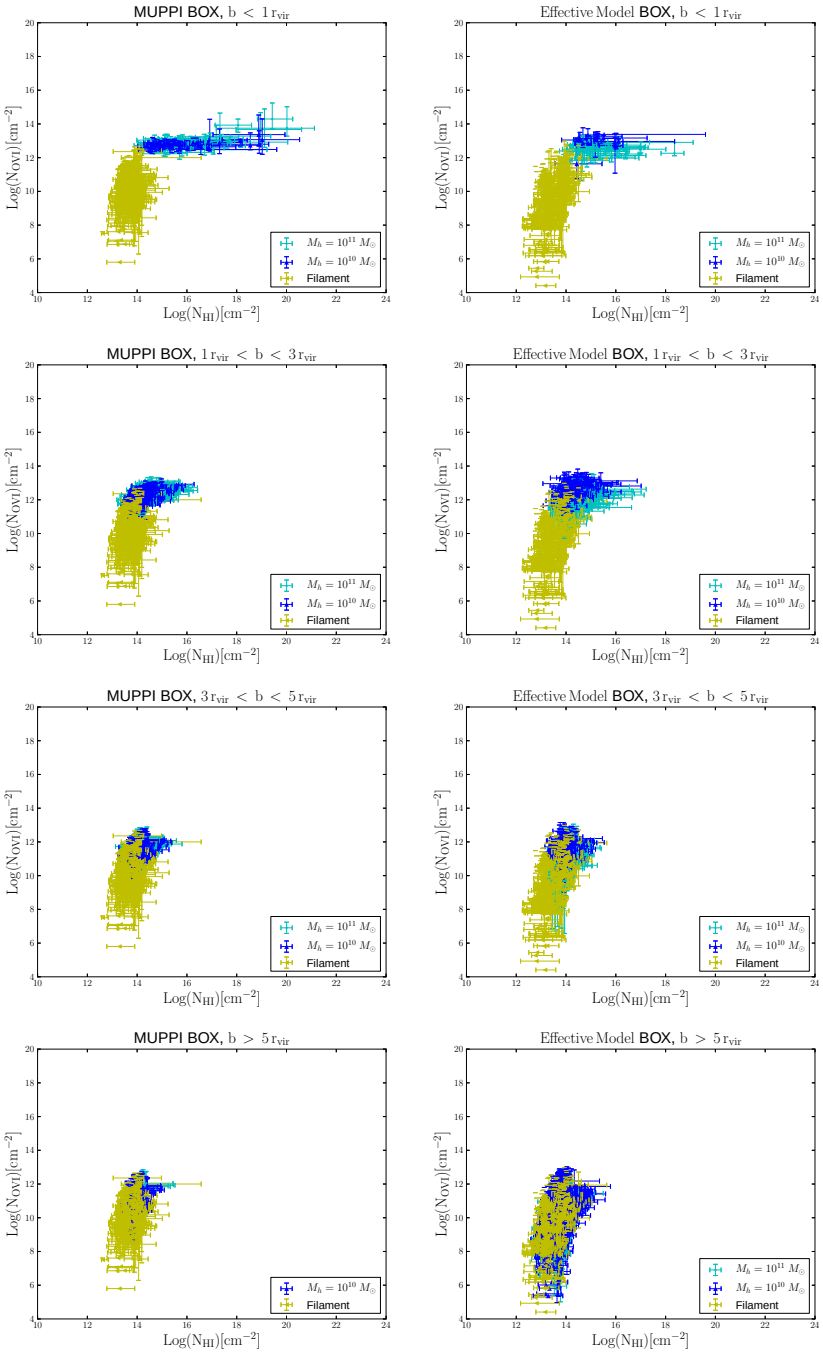

Figure 5.15: (OVI): Each point is the spherical average value of H I and O VI column densities profiles in radial bins of width of $\sim$ 10 kpc around the 30 objects for the MUPPI (left) and the EFFECTIVE (right) model. *Cyan points*: mean values of lines of sights around halos with $M_h \sim 10^{11}$ $M_\odot$. *Blue points*: mean values of lines of sights around halos with $M_h \sim 10^{10}$ $M_\odot$. *Yellow points*: mean values of lines of sights around near-filaments points. Plots have been divided according to the distance of radial galaxy spherical averages from galaxy center in units of virial radius. This division does not concern near-filaments points, whose al values are reported in each plot.

.

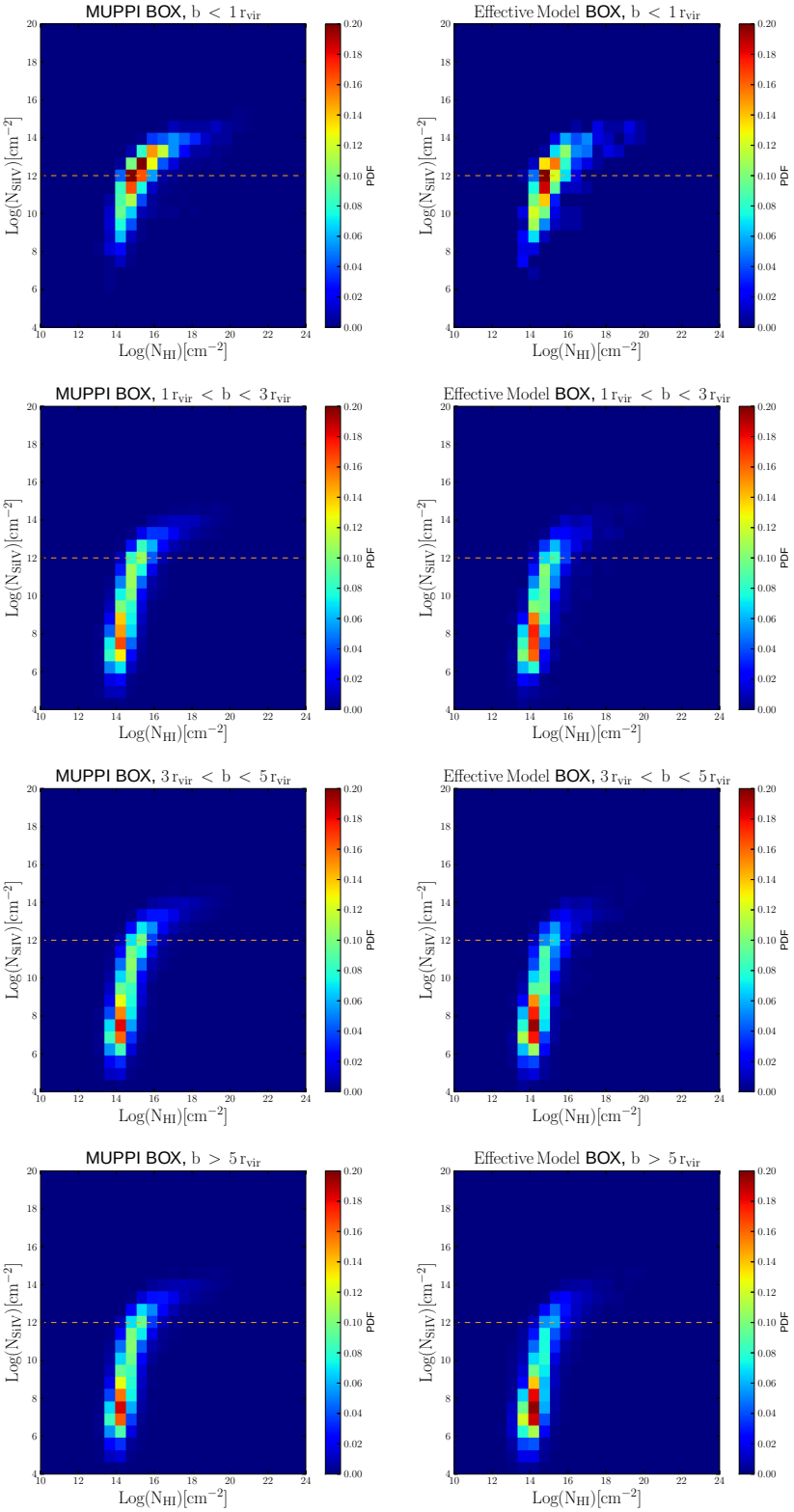

Figure 5.16: (SiIV):PDF of lines of sight around the sample of galaxies.

.

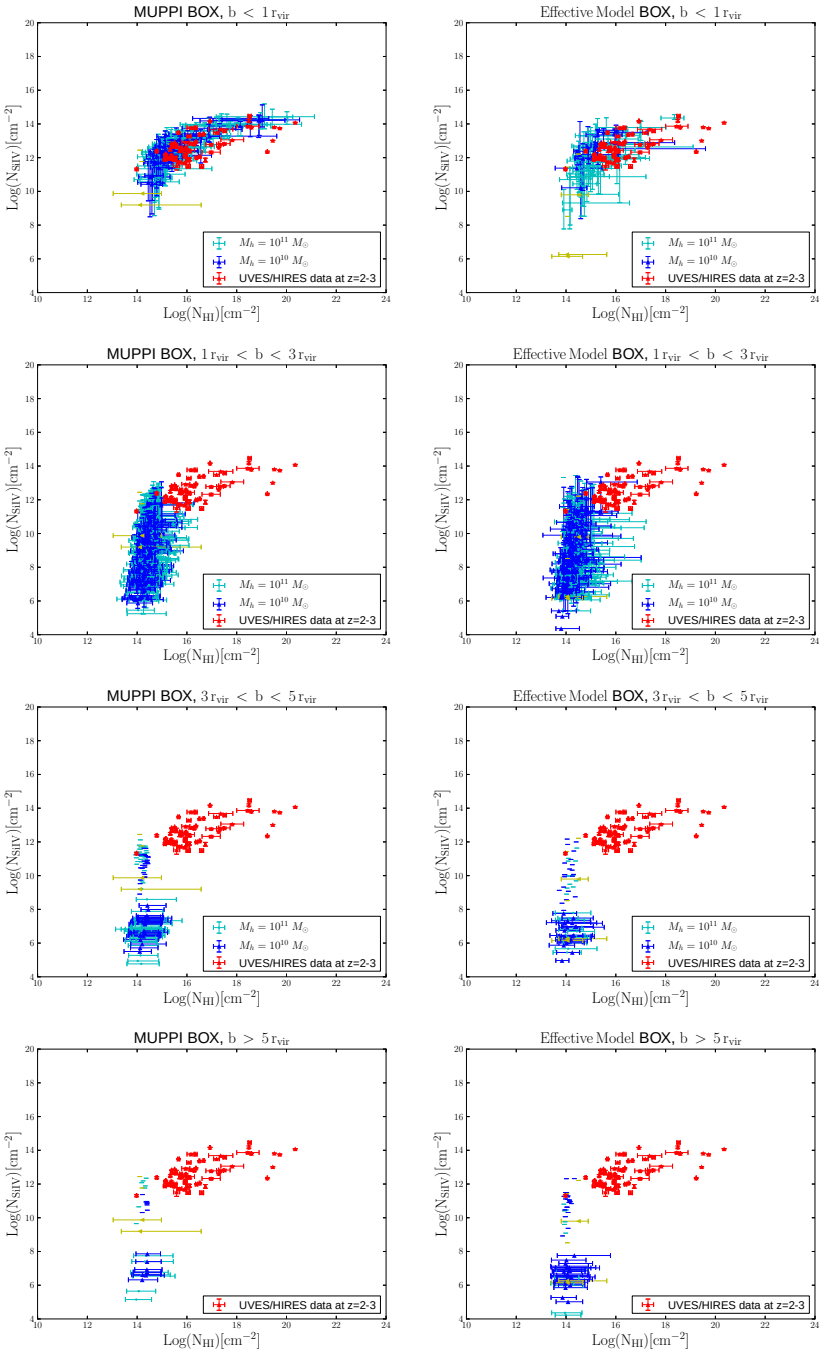

Figure 5.17: (SiIV): Each point is the spherical average value of H I and Si IV column densities profiles in radial bins of width of $\sim$ 10 kpc around the 30 objects for the MUPPI (left) and the EFFECTIVE (right) model. *Cyan points*: mean values of lines of sights around halos with $M_h \sim 10^{11}$ $M_\odot$. *Blue points*: mean values of lines of sights around halos with $M_h \sim 10^{10}$ $M_\odot$. *Yellow points*: mean values of lines of sights around near-filaments points. *Red points*: observational data from Kim et al. (2016) (the same data are reported in each panel). Plots have been divided according to the distance of radial galaxy spherical averages from galaxy center in units of virial radius. This division does not concern near-filaments points, whose al values are reported in each plot.

.

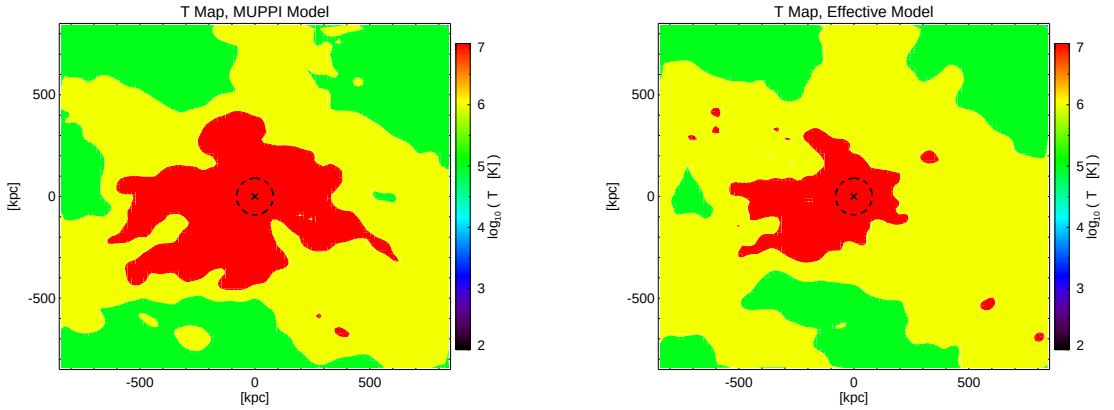

Figure 5.18: Comparison between temperature maps of the same galaxy between the MUPPI and the Effective model. Temperatures are computed integrating the temperature profile along the LOS ± 300 kpc.

width. Shaded areas are the 1 σ error. In Fig. 5.21, instead, I have the covering fraction obtained by integrating ± 600 km s^{-1} , in order to be consistent with the sample of Landoni et al. (2016) and Rubin et al. (2015).

Our calculated covering fraction (orange line with EW $>$ 0.3 Å) is quite in agreement with the sample of Landoni et al. (2016), if I consider also the 1-σ error. Their values are a little bit higher, but this could be due to the fact that their sample is formed by quasar host galaxies and they could be selecting galaxies with slightly higher masses and so bigger halos. For this reason, it should be more correct to report the relations as a function of the distance in units of virial radius. They could also have a bias in the direction, as they are taking face-on galaxies. In other directions, their covering fraction could be lower, due to inhomogeneities of the medium. The sample of Rubin et al. (2015) is actually formed by 40 DLAs, so a little bit different from our work. The masses of the structures forming the DLAs are not known and this could explain why the sample of Rubin et al. (2015) has slightly higher values.

The sample of Prochaska et al. (2014) has a window of integration of ± 1500 km s^{-1}, which is a huge number, due to uncertainties in the redshifts of their quasar sample. Unfortunately, our box size is not big enough, as our maximum range of integration is ± 800 km s^{-1}. I tried to integrate along all the box size and I did recover higher values with respect to those shown in Fig. 5.21, but still not in agreement with the Prochaska et al. (2014) sample. I am confident that if I have had a bigger cosmological box, I would have found similar values to the Prochaska et al. (2014) sample. I would probably have found a situation similar to Landoni et al. (2016), because

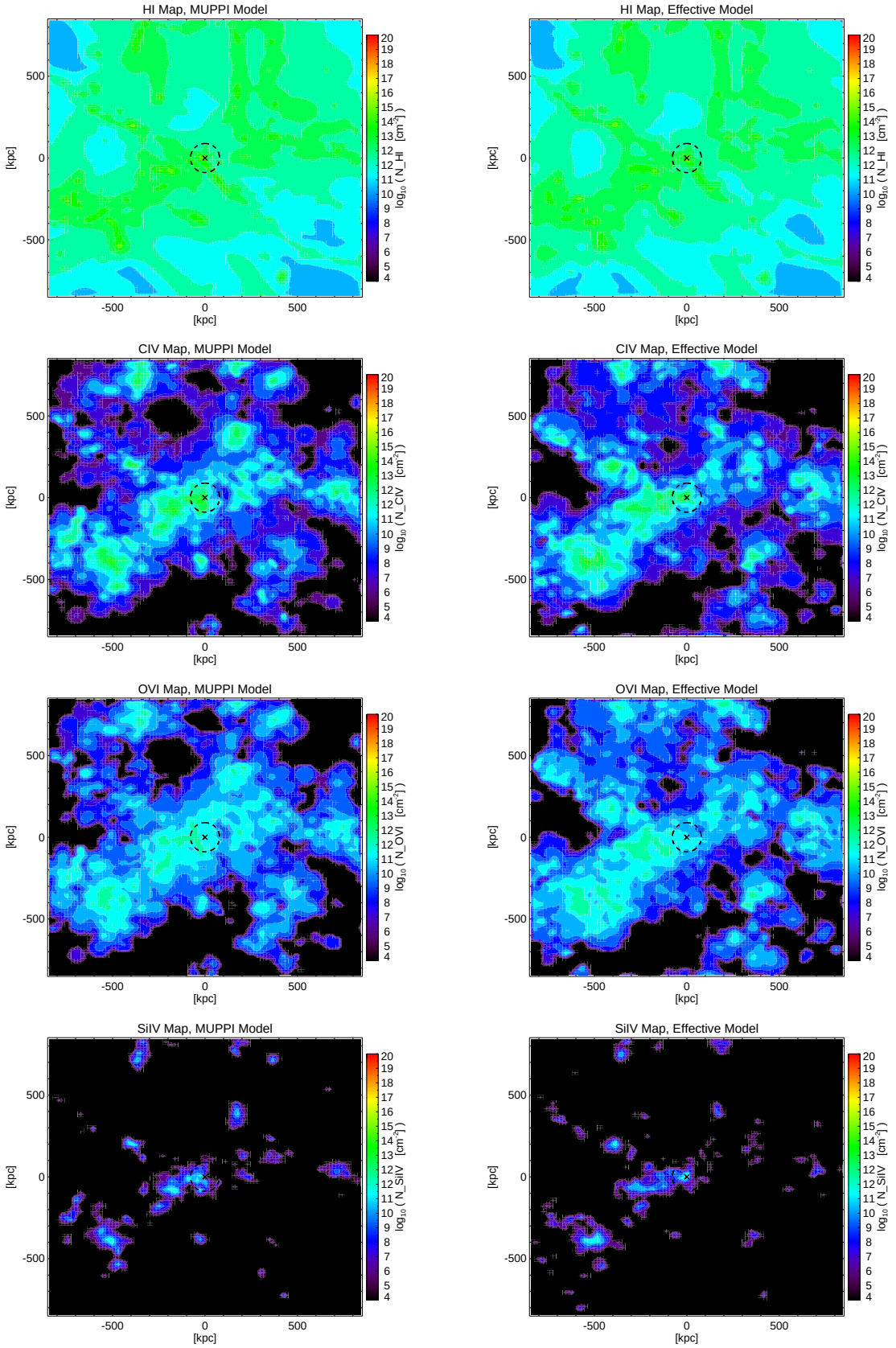

Figure 5.19: Comparison between colum density maps of different chemical elements between the MUPPI and the Effective model. Column densities are computed using the AOD method $\pm$ 150 km s^{-1}.

.

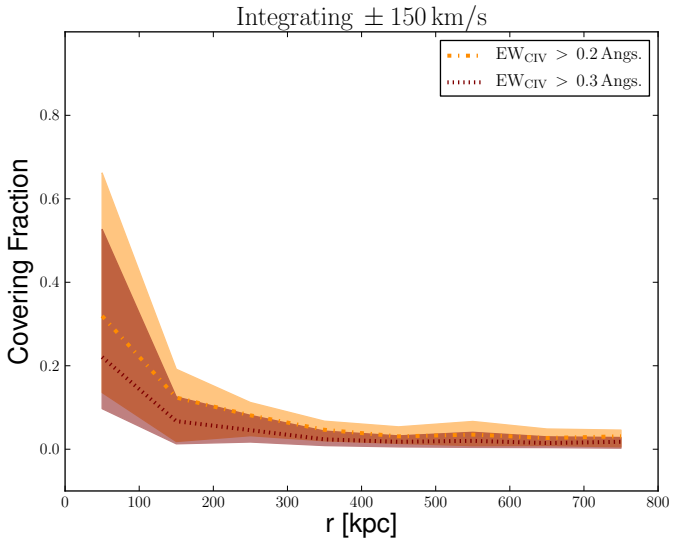

Figure 5.20: C IV covering fraction of our sample of lines of sight, in which rest-frame EW have been integrated ± 150 km s^{-1} from galaxy position. Dotted and dot-dashed lines are the median values corresponding to two different EW thresholds (orange: EW$_{CIV}$ >0.2 Å; red: EW$_{CIV}$ >0.3 Å), while shaded areas are the 1 σ error.

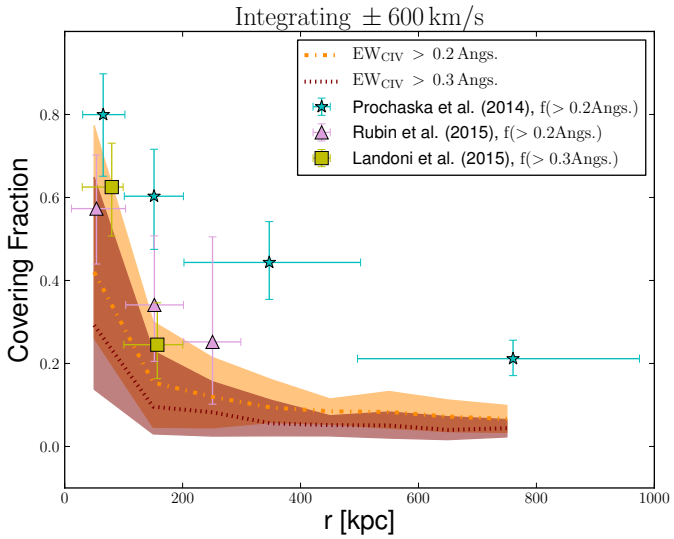

Figure 5.21: C IV covering fraction of our sample of lines of sight, in which rest-frame EW have been integrated ± 600 km s^{-1} , to be consistent with the observational sample of Rubin et al. (2015) and Landoni et al. (2016). The integration window of Prochaska et al. (2014) is of ± 1500 km s^{-1}, a value higher than our box size. This explains the disagreement with the sample of Prochaska et al. (2014).Dotted and dot-dashed lines are the median values corresponding to two different EW thresholds (orange: EW$_{CIV}$ >0.2 Å; red: EW$_{CIV}$ >0.3 Å), while shaded area is the 1 σ error.

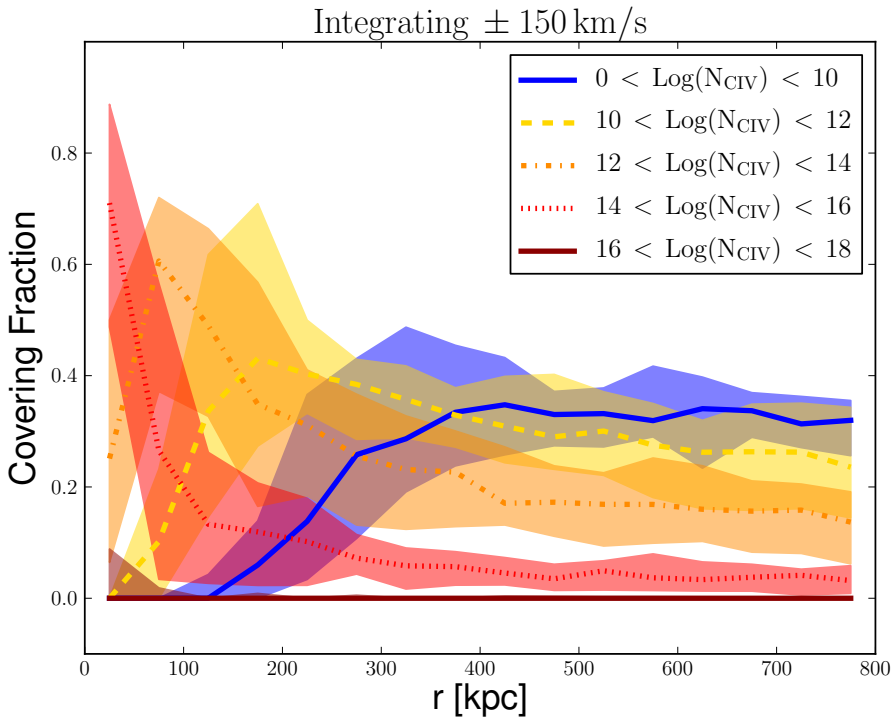

Figure 5.22: Covering fraction of our sample of lines of sight as a function of the C IV column density and not of the equivalent width. Column densities are integrated ± 150 km s^{-1} from galaxy position. Dotted and dot-dashed lines are the median values, while shaded area is the 1 σ error.

also in the Prochaska et al. (2014) sample, they are selecting quasar host galaxies, so there could be a bias in the mass and in the direction of the sampled galaxies.

Computing the covering fraction as a function of the equivalent width is what it has been done so far in the literature, as measuring the equivalent width of an absorption system is the simplest thing that can be done, especially with low resolution data.

With the advent of high-resolution spectroscopy, it has become possible to measure column densities of absorption systems, using Voigt Profile Fitting codes, which give a more reliable and complete information on the physical state of the gas that produced the observed absorption.

For comparison with future samples of high resolution data, I decided to compute the covering fraction as a function of the column density, as it can be seen in Fig. 5.22. I divided the covering fractions in different column densities ranges: $0 \leq \mathrm{Log(N_{CIV})} \leq 10$ [cm^{-2}], $10.0 \leq \mathrm{Log(N_{CIV})} \leq 12.0$ [cm^{-2}] , $12.0 \leq \mathrm{Log(N_{CIV})} \leq 14.0$ [cm^{-2}], $14.0 \leq \mathrm{Log(N_{CIV})} \leq 16.0$ [cm^{-2}] and $16.0 \leq \mathrm{Log(N_{CIV})} \leq 18.0$ [cm^{-2}].

I can see that C IV absorption systems with $\mathrm{Log}(N_{\mathrm{CIV}}) > 14.0$ dominate in the halos of galaxies (d < 100 kpc), even if their covering fraction does not drop to zero at greater distances, due to the presence of substructures.
At higher distances, weaker systems start to dominate, with their covering fraction increasing.

Chapter 6

Summary and future perspectives

The main findings of this thesis work can be summarized as follows:

- I analysed the output of high resolution hydro dynamical simulations with SN feedback implemented both in the thermal and kinetic form. No AGN contribution is considered. In particular, two different subresolution models were considered: the MUPPI model and the Effective model, described in Chapter 4. These two sets share the same large scale structure evolution, but they are decoupled in the hydrodynamical part, as they have different star formation and feedback prescriptions. The MUPPI model has succeded in reproducing quite realistic disk galaxies (Murante et al., 2015).

- I performed a state-of-the-art post-processing analysis and produced a set of mock galaxies and mock spectra. Spectra are constructed using an SPH formulation and profiles of different physical quantities can be reproduced along the line of sight. A sample of 40 galaxies with halo mass in the range $[10^{10} - 10^{12}$ $M_{\odot}]$, half of which are from the MUPPI simulation and the other half from the Effective Model box were selected with the following criteria: galaxies had not be on a major merger, they were the main halo of the FOF-group, in order to analyze the same conditions at the same distance and sampled by a sufficient number of particles. I also considered 20 near-filaments environments from the two runs, by visually centering as close as possible to a filament using the software GADGETVIEWER.

- I identified an optimal analysis of mock QSO spectra based on the Apparent

Optical Depth (AOD) method and compared it critically to the results obtained with Voigt Profile fitting methods. With the advent of high-resolution spectroscopy, it has become possible to measure column densities of absorption systems using Voigt Profile Fitting codes, which give a more reliable and complete information on the physical state of the gas clump that produced the absorption. Unfortunately, this procedure is rather delicate and complex to implement in an automatic way when dealing with thousands of spectra from numerical simulations. On the contrary, I can compute column densities directly from the simulation without applying the fit of the line shape. I performed a comparison between column densities derived with the VPFIT code and the ones directly derived from the simulation. I found that the best and fastest method to use on mock QSO spectra when comparing with observational data is the AOD method. With this method, gas peculiar motions are taken into account and, at the same time, a reliable measure of the column density is obtained.

- I performed a full environmental characterization of the CGM and IGM for absorption systems. In particular, I pierced 4000 lines of sight around each selected object in the simulation with impact parameters less than 800 kpc. Using the C IV as a tracer of the metallicity, I constructed the N_{CIV} versus N_{HI} relation in different radial bins from object's center, which I compared with the observational data by Kim et al. (2016). These data represent a state-of-the-art, homogeneous and statistically significant sample of high resolution absorption lines. I found that observational data have the highest probability to be confined in a region up to 3-5 virial radii from galaxies, which correspond at this redshift to a physical distance of $\sim$ 150 - 400 kpc. Near-filaments points are instead confined to a region under the detection limit, suggesting that they have metallicities too low to be probed by present day observations. These results are validated by the fact that I do not recover any strong difference between the MUPPI and the Effective models. They show very similar trends.

- I presented a probabilistic approach to the galaxy/IGM interplay which carefully quantifies the probability to find an absorption system with a given column density at a certain distance from a galaxy. For example, if a system with a N_{CIV} column density of $\sim 10^{15}$ cm^{-2} and N_{HI} column density of $\sim 10^{16}$ cm^{-2} is found, it has a probability five times higher to be located inside the

virial radius of a galaxy of mass $\sim 10^{10-11}$ $M_{\odot}$ than at a distance of 3-5 virial radii from such a galaxy. If such a system is observed at this great distance from a luminous galaxy, it could be actually related to another smaller and less luminous galaxy.

- I quantified the distribution of ionization species around galaxies in terms of covering factors and compared to data taken from the literature. Considering also the 1 σ error, our data are quite in agreement with the observed one, even if they show a lower normalisation. This could be due to a selection bias in the observational sample, probing galaxies with slightly higher masses. Covering fractions are computed as a function of the equivalent width of the absorption system, as measuring the equivalent width of an absorption system is the simplest thing that can be done, especially with low resolution data. When dealing with high- resolution data, Voigt Profile Fitting provides a stronger information on the gas physical state. For this reasons, I constructed covering fractions depending on the column density and not on the equivalent width of the absorption system, which can be used to compare with future data. Higher column density systems ($\mathrm{Log}(N_{\mathrm{CIV}} \geq 14$ cm^{-2}) predominate in a region of size $\sim$ 100 kpc, while lower column density systems become prevalent at higher distances. The contribution of higher column density systems does not drop to zero due to the fact that galaxies are not isolated systems, but they are surrounded by many structures.

- I extended the work also to other two chemical elements, O VI and Si IV. No observational data were available for a comparison with O VI, but this element shows a very similar behaviour as C IV. This is an indication that these two elements trace a similar gas phase, having both the highest probability to be confined up to a few virial radii from galaxies, characterizing a region typical of the circumgalactic medium. Si IV traces, instead, more internal regions, as it has the highest probability to be observed inside the virial radius, as the comparison with data shows.

- The two simulations which I analyzed in my work give quite similar results apart from the comparison in the radial bin 1 $r_{vir} <$ b < 3 r_{vir} for C IV and O VI. The Effective Model has a higher probability to have absorption systems

with smaller values of H I-C IV-O VI column density and this could be due to a less efficient feedback with respect to the MUPPI model, which is not capable to spread metals with the same strength. For Si IV no difference is observed, but as it is confined in a smaller region, the effects of the feedback could be less visible. This is a quite surprising and unexpected result from the simulation point of view, as the two models are significantly different, both in the star formation and feedback prescriptions. It seems to suggest that galactic feedback and different star formation processes are not strongly impacting on the IGM properties investigated here.

In conclusion, in my thesis I have shown that state-of-the-art observational data likely arise in a region around the galactic halo, more typical of a CGM environment than of the IGM. This could be a hint that physical processes that produce metal enrichment did not affect significantly regions at very low density.
This results is validated by the fact that I obtain similar results in both numerical models used to interpret the data sets.
In the future, it would be interesting to better investigate the comparison between the different subresolution models, in order to understand which physical processes affect more deeply the IGM properties.
Moreover, I would like to extend the analysis of the IGM metal enrichment in simulations, tracing back in time the enriched particles in order to understand the epoch and the mechanisms responsible for the pollution.
Finally, from the observational point of view I expect that new facilities that will come online in the next decade will allow us to deepen our comprehension of the enrichment mechanism. The very weak metal absorptions associated with the IGM will be revealed, if present, by the next generation of spectrographs like ESPRESSO at the VLT, which will see the first light in 2017, and even more with the high-resolution spectrograph for the 39 m European ELT telescope. On the other hand, the relation between the level of enrichment of the IGM studied with metal absorbers and the distribution of galaxies in the same field will be better quantified when also the very faint objects will be identified, in particular with the JWST.

List of Figures

List of Tables

Bibliography

K. L. Adelberger, A. E. Shapley, C. C. Steidel, M. Pettini, D. K. Erb, and N. A. Reddy. The Connection between Galaxies and Intergalactic Absorption Lines at Redshift 2<˜z<˜3. *ApJ*, 629:636–653, August 2005. doi: 10.1086/431753.

A. Aguirre, L. Hernquist, J. Schaye, N. Katz, D. H. Weinberg, and J. Gardner. Metal Enrichment of the Intergalactic Medium in Cosmological Simulations. *ApJ*, 561: 521–549, November 2001. doi: 10.1086/323370.

A. Aguirre, J. Schaye, T.-S. Kim, T. Theuns, M. Rauch, and W. L. W. Sargent. Metallicity of the Intergalactic Medium Using Pixel Statistics. III. Silicon. *ApJ*, 602:38–50, February 2004. doi: 10.1086/380961.

A. Aguirre, C. Dow-Hygelund, J. Schaye, and T. Theuns. Metallicity of the Intergalactic Medium Using Pixel Statistics. IV. Oxygen. *ApJ*, 689:851-864, December 2008. doi: 10.1086/592554.

B. Aracil, P. Petitjean, C. Pichon, and J. Bergeron. Metals in the intergalactic medium. *A&A*, 419:811–819, June 2004. doi: 10.1051/0004-6361:20034346.

B. Atwood, J. A. Baldwin, and R. F. Carswell. Redshift evolution of the Lyman-line-absorbing clouds in quasar spectra. *ApJ*, 292:58–71, May 1985. doi: 10.1086/163132.

M. Aumer, S. D. M. White, T. Naab, and C. Scannapieco. Towards a more realistic population of bright spiral galaxies in cosmological simulations. *MNRAS*, 434: 3142–3164, October 2013. doi: 10.1093/mnras/stt1230.

J. N. Bahcall and E. E. Salpeter. On the Interaction of Radiation from Distant Sources with the Intervening Medium. *ApJ*, 142:1677–1680, November 1965. doi: 10.1086/148460.

S. Bajtlik, R. C. Duncan, and J. P. Ostriker. Quasar ionization of Lyman-alpha clouds - The proximity effect, a probe of the ultraviolet background at high redshift. *ApJ*, 327:570–583, April 1988. doi: 10.1086/166217.

P. Barai, P. Monaco, G. Murante, A. Ragagnin, and M. Viel. Galactic outflow and diffuse gas properties at z $\geq$ 1 using different baryonic feedback models. *MNRAS*, 447:266–286, February 2015. doi: 10.1093/mnras/stu2340.

G. D. Becker, M. Rauch, and W. L. W. Sargent. The Evolution of Optical Depth in the Lyα Forest: Evidence Against Reionization at z$\sim$6. *ApJ*, 662:72–93, June 2007. doi: 10.1086/517866.

R. H. Becker, X. Fan, R. L. White, M. A. Strauss, V. K. Narayanan, R. H. Lupton, J. E. Gunn, J. Annis, N. A. Bahcall, J. Brinkmann, A. J. Connolly, I. Csabai, P. C. Czarapata, M. Doi, T. M. Heckman, G. S. Hennessy, Ž. Ivezić, G. R. Knapp, D. Q. Lamb, T. A. McKay, J. A. Munn, T. Nash, R. Nichol, J. R. Pier, G. T. Richards, D. P. Schneider, C. Stoughton, A. S. Szalay, A. R. Thakar, and D. G. York. Evidence for Reionization at z˜6: Detection of a Gunn-Peterson Trough in a z=6.28 Quasar. *AJ*, 122:2850–2857, December 2001. doi: 10.1086/324231.

T. A. M. Berg, S. L. Ellison, J. X. Prochaska, R. Sánchez-Ramírez, S. Lopez, V. D'Odorico, G. Becker, L. Christensen, G. Cupani, K. Denney, and G. Worseck. On the selection of damped Lyman α systems using Mg ii absorption at2. *MNRAS*, 464:L56–L60, January 2017. doi: 10.1093/mnrasl/slw185.

J. Bergeron and S. Herbert-Fort. Highly ionized absorbers at high redshift. *ArXiv Astrophysics e-prints*, June 2005.

J. Bergeron, B. Aracil, P. Petitjean, and C. Pichon. The warm-hot intergalactic medium at z $\sim$ 2.2: Metal enrichment and ionization source. *A&A*, 396:L11–L15, December 2002. doi: 10.1051/0004-6361:20021611.

H. Bi. Lyman-alpha absorption spectrum of the primordial intergalactic medium. *ApJ*, 405:479–490, March 1993. doi: 10.1086/172380.

H. Bi and A. F. Davidsen. Evolution of Structure in the Intergalactic Medium and the Nature of the Lyα Forest. *ApJ*, 479:523–542, April 1997.

H. G. Bi, G. Boerner, and Y. Chu. An alternative model for the Ly-alpha absorption forest. *A&A*, 266:1–5, December 1992.

S. Bianchi, S. Cristiani, and T.-S. Kim. The contribution of galaxies to the UV ionising background and the evolution of the Lyman forest. *A&A*, 376:1–9, September 2001. doi: 10.1051/0004-6361:20010944.

J. H. Black. The physical state of primordial intergalactic clouds. *MNRAS*, 197: 553–563, November 1981. doi: 10.1093/mnras/197.3.553.

L. Blitz and E. Rosolowsky. The Role of Pressure in GMC Formation II: The H_2-Pressure Relation. *ApJ*, 650:933–944, October 2006. doi: 10.1086/505417.

A. Boksenberg and W. L. W. Sargent. Properties of QSO Metal-line Absorption Systems at High Redshifts: Nature and Evolution of the Absorbers and New Evidence on Escape of Ionizing Radiation from Galaxies. *ApJS*, 218:7, May 2015. doi: 10.1088/0067-0049/218/1/7.

J. S. Bolton, M. Viel, T.-S. Kim, M. G. Haehnelt, and R. F. Carswell. Possible evidence for an inverted temperature-density relation in the intergalactic medium from the flux distribution of the Lyα forest. *MNRAS*, 386:1131–1144, May 2008. doi: 10.1111/j.1365-2966.2008.13114.x.

J. R. Bond and J. W. Wadsley. LYα Absorption in the Cosmic Web. In P. Petitjean and S. Charlot, editors, *Structure and Evolution of the Intergalactic Medium from QSO Absorption Line System*, page 143, 1997.

C. M. Booth and J. Schaye. Cosmological simulations of the growth of supermassive black holes and feedback from active galactic nuclei: method and tests. *MNRAS*, 398:53–74, September 2009. doi: 10.1111/j.1365-2966.2009.15043.x.

R. Bordoloi, J. Tumlinson, J. K. Werk, B. D. Oppenheimer, M. S. Peeples, J. X. Prochaska, T. M. Tripp, N. Katz, R. Davé, A. J. Fox, C. Thom, A. B. Ford, D. H. Weinberg, J. N. Burchett, and J. A. Kollmeier. The COS-Dwarfs Survey: The Carbon Reservoir around Sub-L* Galaxies. *ApJ*, 796:136, December 2014. doi: 10.1088/0004-637X/796/2/136.

G. L. Bryan, M. L. Norman, B. W. O'Shea, T. Abel, J. H. Wise, M. J. Turk, D. R. Reynolds, D. C. Collins, P. Wang, S. W. Skillman, B. Smith, R. P. Harkness, J. Bordner, J.-h. Kim, M. Kuhlen, H. Xu, N. Goldbaum, C. Hummels, A. G. Kritsuk, E. Tasker, S. Skory, C. M. Simpson, O. Hahn, J. S. Oishi, G. C. So, F. Zhao, R. Cen, Y. Li, and Enzo Collaboration. ENZO: An Adaptive Mesh Refinement Code for Astrophysics. *ApJS*, 211:19, April 2014. doi: 10.1088/0067-0049/211/2/19.

G. R. Burbidge, M. Burbidge, F. Hoyle, and C. R. Lynds. On the Interpretation of the Line Spectra of Quasi-Stellar Objects. *Nature*, 210:774–778, May 1966. doi: 10.1038/210774a0.

N. G. Busca, T. Delubac, J. Rich, S. Bailey, A. Font-Ribera, D. Kirkby, J.-M. Le Goff, M. M. Pieri, A. Slosar, É. Aubourg, J. E. Bautista, D. Bizyaev, M. Blomqvist, A. S. Bolton, J. Bovy, H. Brewington, A. Borde, J. Brinkmann, B. Carithers, R. A. C. Croft, K. S. Dawson, G. Ebelke, D. J. Eisenstein, J.-C. Hamilton, S. Ho, D. W. Hogg, K. Honscheid, K.-G. Lee, B. Lundgren, E. Malanushenko, V. Malanushenko, D. Margala, C. Maraston, K. Mehta, J. Miralda-Escudé, A. D. Myers, R. C. Nichol, P. Noterdaeme, M. D. Olmstead, D. Oravetz, N. Palanque-Delabrouille, K. Pan, I. Pâris, W. J. Percival, P. Petitjean, N. A. Roe, E. Rollinde, N. P. Ross, G. Rossi, D. J. Schlegel, D. P. Schneider, A. Shelden, E. S. Sheldon, A. Simmons, S. Snedden, J. L. Tinker, M. Viel, B. A. Weaver, D. H. Weinberg, M. White, C. Yèche, and D. G. York. Baryon acoustic oscillations in the Lyα forest of BOSS quasars. *A&A*, 552:A96, April 2013. doi: 10.1051/0004-6361/201220724.

F. Calura, E. Tescari, V. D'Odorico, M. Viel, S. Cristiani, T.-S. Kim, and J. S. Bolton. The Lyman α forest flux probability distribution at z>3. *MNRAS*, 422: 3019–3036, June 2012. doi: 10.1111/j.1365-2966.2012.20811.x.

B. Carswell, J. Schaye, and T.-S. Kim. The Enrichment History of the Intergalactic Medium: O VI in Lyα Forest Systems at Redshift z$\sim$2. *ApJ*, 578:43–59, October 2002. doi: 10.1086/342404.

R. F. Carswell and M. J. Rees. Constraints on voids at high redshifts from Ly-alpha absorbers. *MNRAS*, 224:13P–16P, January 1987. doi: 10.1093/mnras/224.1.13P.

R. F. Carswell and J. K. Webb. VPFIT: Voigt profile fitting program. Astrophysics Source Code Library, August 2014.

R. F. Carswell, J. K. Webb, J. A. Baldwin, and B. Atwood. High-redshift QSO absorbing clouds and the background ionizing source. *ApJ*, 319:709–722, August 1987. doi: 10.1086/165491.

R. F. Carswell, K. M. Lanzetta, H. C. Parnell, and J. K. Webb. High-resolution spectroscopy of Q1100 - 264 again. *ApJ*, 371:36–48, April 1991. doi: 10.1086/169868.

R. Cen and N. E. Chisari. Star Formation Feedback and Metal-enrichment History of the Intergalactic Medium. *ApJ*, 731:11, April 2011. doi: 10.1088/0004-637X/731/1/11.

H. Couchman, F. Pearce, and P. Thomas. Hydra: A Parallel Adaptive Grid Code. Astrophysics Source Code Library, March 2011.

L. L. Cowie and A. Songaila. Heavy-element enrichment in low-density regions of the intergalactic medium. *Nature*, 394:44–46, July 1998. doi: 10.1038/27845.

L. L. Cowie, A. Songaila, T.-S. Kim, and E. M. Hu. The metallicity and internal structure of the Lyman-alpha forest clouds. *AJ*, 109:1522–1530, April 1995. doi: 10.1086/117381.

S. Cristiani, S. D'Odorico, A. Fontana, E. Giallongo, and S. Savaglio. The space distribution of the Lyman alpha clouds in the line of sight to the z=3.66 QSO 0055-269. *MNRAS*, 273:1016–1032, April 1995. doi: 10.1093/mnras/273.4.1016.

S. Cristiani, S. D'Odorico, V. D'Odorico, A. Fontana, E. Giallongo, and S. Savaglio. The clustering properties of the Lyman <e6>alpha</e6> clouds. *MNRAS*, 285: 209–217, February 1997. doi: 10.1093/mnras/285.1.209.

R. A. C. Croft, D. H. Weinberg, N. Katz, and L. Hernquist. Recovery of the Power Spectrum of Mass Fluctuations from Observations of the Lyα Forest. *ApJ*, 495: 44–62, March 1998. doi: 10.1086/305289.

R. A. C. Croft, D. H. Weinberg, M. Bolte, S. Burles, L. Hernquist, N. Katz, D. Kirkman, and D. Tytler. Toward a Precise Measurement of Matter Clustering: Lyα Forest Data at Redshifts 2-4. *ApJ*, 581:20–52, December 2002. doi: 10.1086/344099.

R. Davé, U. Hellsten, L. Hernquist, N. Katz, and D. H. Weinberg. Constraining the Metallicity of the Low-Density Lyα Forest Using O VI Absorption. *ApJ*, 509: 661–677, December 1998. doi: 10.1086/306524.

R. Davé, L. Hernquist, N. Katz, and D. H. Weinberg. The Low-Redshift Lyα Forest in Cold Dark Matter Cosmologies. *ApJ*, 511:521–545, February 1999. doi: 10.1086/306722.

A. De Luca and S. Molendi. The 2-8 keV cosmic X-ray background spectrum as observed with XMM-Newton. *A&A*, 419:837–848, June 2004. doi: 10.1051/0004-6361:20034421.

M. Dessauges-Zavadsky, C. Péroux, T.-S. Kim, S. D'Odorico, and R. G. McMahon. A homogeneous sample of sub-damped Lyman α systems - I. Construction of the sample and chemical abundance measurements. *MNRAS*, 345:447–479, October 2003. doi: 10.1046/j.1365-8711.2003.06949.x.

V. D'Odorico, M. Viel, F. Saitta, S. Cristiani, S. Bianchi, B. Boyle, S. Lopez, J. Maza, and P. Outram. Tomography of the intergalactic medium with Lyα forests in close QSO pairs. *MNRAS*, 372:1333–1344, November 2006. doi: 10.1111/j.1365-2966.2006.10941.x.

V. D'Odorico, F. Calura, S. Cristiani, and M. Viel. The rise of the CIV mass density at z $<$ 2.5. *MNRAS*, 401:2715–2721, February 2010. doi: 10.1111/j.1365-2966.2009.15856.x.

V. D'Odorico, S. Cristiani, E. Pomante, R. F. Carswell, M. Viel, P. Barai, G. D. Becker, F. Calura, G. Cupani, F. Fontanot, M. G. Haehnelt, T.-S. Kim, J. Miralda-Escudé, A. Rorai, E. Tescari, and E. Vanzella. Metals in the z$\sim$ 3 intergalactic medium: results from an ultra-high signal-to-noise ratio UVES quasar spectrum. *MNRAS*, 463:2690–2707, December 2016. doi: 10.1093/mnras/stw2161.

G. Efstathiou. Suppressing the formation of dwarf galaxies via photoionization. *MNRAS*, 256:43P–47P, May 1992. doi: 10.1093/mnras/256.1.43P.

S. L. Ellison, G. F. Lewis, M. Pettini, F. H. Chaffee, and M. J. Irwin. HIRES Spectroscopy of APM 08279+5255: Metal Abundances in the Lyα Forest. *ApJ*, 520:456–468, August 1999. doi: 10.1086/307503.

S. L. Ellison, A. Songaila, J. Schaye, and M. Pettini. The Enrichment History of the Intergalactic Medium-Measuring the C IV/H I Ratio in the Lyα Forest. *AJ*, 120:1175–1191, September 2000. doi: 10.1086/301511.

D. K. Erb, A. E. Shapley, M. Pettini, C. C. Steidel, N. A. Reddy, and K. L. Adelberger. The Mass-Metallicity Relation at z$>\sim$2. *ApJ*, 644:813–828, June 2006. doi: 10.1086/503623.

A. E. Evrard. Formation and evolution of X-ray clusters - A hydrodynamic simulation of the intracluster medium. *ApJ*, 363:349–366, November 1990. doi: 10.1086/169350.

C.-A. Faucher-Giguère, A. Lidz, M. Zaldarriaga, and L. Hernquist. The Line-of-Sight Proximity Effect and the Mass of Quasar Host Halos. *ApJ*, 673:39-61, January 2008. doi: 10.1086/521639.

G. G. Fazio, M. L. N. Ashby, P. Barmby, J. L. Hora, J.-S. Huang, M. A. Pahre, Z. Wang, S. P. Willner, R. G. Arendt, S. H. Moseley, M. Brodwin, P. Eisenhardt, D. Stern, E. V. Tollestrup, and E. L. Wright. Number Counts at 3 μm $< \lambda <$ 10 μm from the Spitzer Space Telescope. *ApJS*, 154:39–43, September 2004. doi: 10.1086/422585.

C. Fechner and P. Richter. The nature of N V absorbers at high redshift. *A&A*, 496:31–44, March 2009. doi: 10.1051/0004-6361/200810421.

G. J. Ferland, R. L. Porter, P. A. M. van Hoof, R. J. R. Williams, N. P. Abel, M. L. Lykins, G. Shaw, W. J. Henney, and P. C. Stancil. The 2013 Release of Cloudy. *Rev. Mex. Astron. Astrofis.*, 49:137–163, April 2013.

A. Fontana and P. Ballester. FITLYMAN: a Midas tool for the analysis of absorption spectra. *The Messenger*, 80:37–41, June 1995.

A. J. Fox, B. D. Savage, and B. P. Wakker. Measurement of Noisy Absorption Lines Using the Apparent Optical Depth Technique. *AJ*, 130:2418–2423, November 2005. doi: 10.1086/491735.

S. Frank, S. Mathur, M. Pieri, and D. G. York. A Survey of Metal Lines at High Redshift. II. SDSS Absorption Line Studies - O VI Line Density, Space Density, and Gas Metallicity at z $_{abs}$ ˜ 3.0. *AJ*, 140:835–843, September 2010. doi: 10.1088/0004-6256/140/3/835.

C. Fransson and R. Epstein. Winds from dwarf galaxies and Lyman-alpha absorption features in quasar spectra. *MNRAS*, 198:1127–1141, March 1982. doi: 10.1093/mnras/198.4.1127.

B. Frye, T. Broadhurst, and N. Benítez. Spectral Evidence for Widespread Galaxy Outflows at z > 4. *ApJ*, 568:558–575, April 2002. doi: 10.1086/338965.

B. Fryxell, K. Olson, P. Ricker, F. X. Timmes, M. Zingale, D. Q. Lamb, P. MacNeice, R. Rosner, J. W. Truran, and H. Tufo. FLASH: An Adaptive Mesh Hydrodynamics Code for Modeling Astrophysical Thermonuclear Flashes. *ApJS*, 131:273–334, November 2000. doi: 10.1086/317361.

I. Georgantopoulos, G. C. Stewart, T. Shanks, B. J. Boyle, and R. E. Griffiths. A deep ROSAT survey - V. The extragalactic populations at faint fluxes. *MNRAS*, 280:276–284, May 1996. doi: 10.1093/mnras/280.1.276.

L. Greggio and A. Renzini. The binary model for type I supernovae - Theoretical rates. *A&A*, 118:217–222, February 1983.

D. E. Gruber, J. L. Matteson, L. E. Peterson, and G. V. Jung. The Spectrum of Diffuse Cosmic Hard X-Rays Measured with HEAO 1. *ApJ*, 520:124–129, July 1999. doi: 10.1086/307450.

J. E. Gunn and B. A. Peterson. On the Density of Neutral Hydrogen in Intergalactic Space. *ApJ*, 142:1633–1641, November 1965. doi: 10.1086/148444.

F. Haardt and P. Madau. Radiative Transfer in a Clumpy Universe. II. The Ultraviolet Extragalactic Background. *ApJ*, 461:20, April 1996. doi: 10.1086/177035.

F. Haardt and P. Madau. Modelling the UV/X-ray cosmic background with CUBA. In D. M. Neumann and J. T. V. Tran, editors, *Clusters of Galaxies and the High Redshift Universe Observed in X-rays*, 2001.

F. Haardt and P. Madau. Radiative Transfer in a Clumpy Universe. IV. New Synthesis Models of the Cosmic UV/X-Ray Background. *ApJ*, 746:125, February 2012. doi: 10.1088/0004-637X/746/2/125.

T. M. Heckman, M. D. Lehnert, D. K. Strickland, and L. Armus. Absorption-Line Probes of Gas and Dust in Galactic Superwinds. *ApJS*, 129:493–516, August 2000. doi: 10.1086/313421.

L. Hernquist, N. Katz, D. H. Weinberg, and J. Miralda-Escudé. The Lyman-Alpha Forest in the Cold Dark Matter Model. *ApJ*, 457:L51, February 1996. doi: 10.1086/309899.

P. F. Hopkins. GIZMO: Multi-method magneto-hydrodynamics+gravity code. Astrophysics Source Code Library, October 2014.

E. M. Hu, T.-S. Kim, L. L. Cowie, A. Songaila, and M. Rauch. The Distribution of Column Densities and B Values in the Lyman-Alpha Forest. *AJ*, 110:1526, October 1995. doi: 10.1086/117625.

W. Hu. Reionization Revisited: Secondary Cosmic Microwave Background Anisotropies and Polarization. *ApJ*, 529:12–25, January 2000. doi: 10.1086/308279.

L. Hui and N. Y. Gnedin. Equation of state of the photoionized intergalactic medium. *MNRAS*, 292:27, November 1997. doi: 10.1093/mnras/292.1.27.

E. Janknecht, D. Reimers, S. Lopez, and D. Tytler. The evolution of Lyman α absorbers in the redshift range $0.5 < z < 1.9$. *A&A*, 458:427–439, November 2006. doi: 10.1051/0004-6361:20065372.

A. Jenkins, C. S. Frenk, F. R. Pearce, P. A. Thomas, J. M. Colberg, S. D. M. White, H. M. P. Couchman, J. A. Peacock, G. Efstathiou, and A. H. Nelson. Evolution of Structure in Cold Dark Matter Universes. *ApJ*, 499:20–40, May 1998. doi: 10.1086/305615.

A. Jenkins, C. S. Frenk, S. D. M. White, J. M. Colberg, S. Cole, A. E. Evrard, H. M. P. Couchman, and N. Yoshida. The mass function of dark matter haloes. *MNRAS*, 321:372–384, February 2001. doi: 10.1046/j.1365-8711.2001.04029.x.

E. B. Jenkins. A Procedure for Correcting the Apparent Optical Depths of Moderately Saturated Interstellar Absorption Lines. *ApJ*, 471:292, November 1996. doi: 10.1086/177969.

E. B. Jenkins and J. P. Ostriker. Lyman-alpha depression of the continuum from high-redshift quasars - A new technique applied in search of the Gunn-Peterson effect. *ApJ*, 376:33–42, July 1991. doi: 10.1086/170252.

G. G. Kacprzak, F. van de Voort, K. Glazebrook, K.-V. H. Tran, T. Yuan, T. Nanayakkara, R. J. Allen, L. Alcorn, M. Cowley, I. Labbé, L. Spitler, C. Straatman, and A. Tomczak. Cold-mode Accretion: Driving the Fundamental Mass-Metallicity Relation at $z \sim 2$. *ApJ*, 826:L11, July 2016. doi: 10.3847/2041-8205/826/1/L11.

N. Katz. Dissipational galaxy formation. II - Effects of star formation. *ApJ*, 391: 502–517, June 1992. doi: 10.1086/171366.

N. Katz, D. H. Weinberg, and L. Hernquist. Cosmological Simulations with TreeSPH. *ApJS*, 105:19, July 1996. doi: 10.1086/192305.

R. C. Kennicutt, Jr. The Global Schmidt Law in Star-forming Galaxies. *ApJ*, 498: 541–552, May 1998. doi: 10.1086/305588.

D. Kereš, N. Katz, D. H. Weinberg, and R. Davé. How do galaxies get their gas? *MNRAS*, 363:2–28, October 2005. doi: 10.1111/j.1365-2966.2005.09451.x.

T.-S. Kim, E. M. Hu, L. L. Cowie, and A. Songaila. The Redshift Evolution of the Ly alpha Forest. *AJ*, 114:1–13, July 1997. doi: 10.1086/118446.

T.-S. Kim, S. Cristiani, and S. D'Odorico. The Lyalpha forest at $1.5 < z < 4$. *A&A*, 373:757–781, July 2001. doi: 10.1051/0004-6361:20010650.

T.-S. Kim, R. F. Carswell, S. Cristiani, S. D'Odorico, and E. Giallongo. The physical properties of the Lyα forest at $z > 1.5$. *MNRAS*, 335:555–573, September 2002a. doi: 10.1046/j.1365-8711.2002.05599.x.

T.-S. Kim, S. Cristiani, and S. D'Odorico. The evolution of the physical state of the IGM. *A&A*, 383:747–754, March 2002b. doi: 10.1051/0004-6361:20011812.

T.-S. Kim, M. Viel, M. G. Haehnelt, R. F. Carswell, and S. Cristiani. The power spectrum of the flux distribution in the Lyman α forest of a large sample of UVES QSO absorption spectra (LUQAS). *MNRAS*, 347:355–366, January 2004. doi: 10.1111/j.1365-2966.2004.07221.x.

T.-S. Kim, J. S. Bolton, M. Viel, M. G. Haehnelt, and R. F. Carswell. An improved measurement of the flux distribution of the Lyα forest in QSO absorption spectra: the effect of continuum fitting, metal contamination and noise properties. *MNRAS*, 382:1657–1674, December 2007. doi: 10.1111/j.1365-2966.2007.12406.x.

T.-S. Kim, A. M. Partl, R. F. Carswell, and V. Müller. The evolution of H I and C IV quasar absorption line systems at $1.9 < z < 3.2$. *A&A*, 552:A77, April 2013. doi: 10.1051/0004-6361/201220042.

T.-S. Kim, R. F. Carswell, C. Mongardi, A. M. Partl, J. P. Muecket, P. Barai, and S. Cristiani. Triple-ionised carbon associated with the low-density neutral hydrogen gas at $1.7 \leq z \leq 3.3$: the integrated N(HI)-N(CIV) relation. *ArXiv e-prints*, January 2016.

R. L. Kinzer, G. V. Jung, D. E. Gruber, J. L. Matteson, Peterson, and L. E. Diffuse Cosmic Gamma Radiation Measured by HEAO 1. *ApJ*, 475:361–372, January 1997.

D. Kirkman and D. Tytler. Intrinsic Properties of the $<z> = 2.7$ Lyα Forest from Keck Spectra of Quasar HS 1946+7658. *ApJ*, 484:672–694, July 1997.

A. V. Kravtsov, A. A. Klypin, and A. M. Khokhlov. Adaptive Refinement Tree: A New High-Resolution N-Body Code for Cosmological Simulations. *ApJS*, 111: 73–94, July 1997. doi: 10.1086/313015.

P. Kroupa, C. A. Tout, and G. Gilmore. The distribution of low-mass stars in the Galactic disc. *MNRAS*, 262:545–587, June 1993. doi: 10.1093/mnras/262.3.545.

M. Landoni, R. Falomo, A. Treves, R. Scarpa, and E. P. Farina. Circumgalactic medium of quasars: C IV absorption systems. *MNRAS*, 457:267–271, March 2016. doi: 10.1093/mnras/stv2964.

K.-G. Lee, J. F. Hennawi, D. N. Spergel, D. H. Weinberg, D. W. Hogg, M. Viel, J. S. Bolton, S. Bailey, M. M. Pieri, W. Carithers, D. J. Schlegel, B. Lundgren, N. Palanque-Delabrouille, N. Suzuki, D. P. Schneider, and C. Yèche. IGM Constraints from the SDSS-III/BOSS DR9 Lyα Forest Transmission Probability Distribution Function. *ApJ*, 799:196, February 2015. doi: 10.1088/0004-637X/799/2/196.

C. J. Liang and H.-W. Chen. Mining circumgalactic baryons in the low-redshift universe. *MNRAS*, 445:2061–2081, December 2014. doi: 10.1093/mnras/stu1901.

L. Lu, W. L. W. Sargent, D. S. Womble, and M. Takada-Hidai. The Lyman-Alpha Forest at Z approximately 4: Keck HIRES Observations of Q0000-26. *ApJ*, 472: 509, December 1996. doi: 10.1086/526756.

L. Lu, W. L. W. Sargent, T. A. Barlow, and M. Rauch. The Metal Contents of Very Low Column Density Lyman-alpha Clouds: Implications for the Origin of Heavy Elements in the Intergalactic Medium. *ArXiv Astrophysics e-prints*, February 1998.

D. H. Lumb, R. S. Warwick, M. Page, and A. De Luca. X-ray background measurements with XMM-Newton EPIC. *A&A*, 389:93–105, July 2002. doi: 10.1051/0004-6361:20020531.

B. Lundgren, Y. AlSayyad, J. Ge, F. W. Hamann, B. Ménard, J. Miralda, A. D. Myers, I. Paris, I. P. i. Rafols, P. Petitjean, M. Pieri, N. Ross, D. P. Schneider, J. Tinker, S. K. Vikas, D. Wake, W. M. Wood-Vasey, D. G. York, G. Zhu, and SDSS-III BOSS Collaboration. The Clustering and Evolution of Mg II and C IV Absorption Systems in the BOSS Quasar Spectra. In *American Astronomical Society Meeting Abstracts #221*, volume 221 of *American Astronomical Society Meeting Abstracts*, page 402.05, January 2013.

B. Lundgren, G. Brammer, Dr., D. G. York, J. P. Chisholm, D. Erb, V. P. Kulkarni, L. Straka, C. A. Tremonti, P. G. Van Dokkum, and D. Wake. Revealing the Properties of Mg II Absorbing Galaxies at z $>$ 1 with HST WFC3/IR. In *American*

Astronomical Society Meeting Abstracts, volume 225 of *American Astronomical Society Meeting Abstracts*, page 314.07, January 2015.

R. Lynds. The Absorption-Line Spectrum of 4c 05.34. *ApJ*, 164:L73, March 1971. doi: 10.1086/180695.

P. Madau and L. Pozzetti. Deep galaxy counts, extragalactic background light and the stellar baryon budget. *MNRAS*, 312:L9–L15, February 2000. doi: 10.1046/j.1365-8711.2000.03268.x.

F. Marinacci, R. Pakmor, and V. Springel. The formation of disc galaxies in high-resolution moving-mesh cosmological simulations. *MNRAS*, 437:1750–1775, January 2014. doi: 10.1093/mnras/stt2003.

C. L. Martin. Properties of Galactic Outflows: Measurements of the Feedback from Star Formation. *ApJ*, 513:156–160, March 1999. doi: 10.1086/306863.

C. L. Martin. Mapping Large-Scale Gaseous Outflows in Ultraluminous Galaxies with Keck II ESI Spectra: Variations in Outflow Velocity with Galactic Mass. *ApJ*, 621:227–245, March 2005. doi: 10.1086/427277.

C. L. Martin, E. Scannapieco, S. L. Ellison, J. F. Hennawi, S. G. Djorgovski, and A. P. Fournier. The Size and Origin of Metal-enriched Regions in the Intergalactic Medium from Spectra of Binary Quasars. *ApJ*, 721:174–192, September 2010. doi: 10.1088/0004-637X/721/1/174.

F. Matteucci and L. Greggio. Relative roles of type I and II supernovae in the chemical enrichment of the interstellar gas. *A&A*, 154:279–287, January 1986.

F. Matteucci and S. Recchi. On the Typical Timescale for the Chemical Enrichment from Type Ia Supernovae in Galaxies. *ApJ*, 558:351–358, September 2001. doi: 10.1086/322472.

P. McDonald, J. Miralda-Escudé, M. Rauch, W. L. W. Sargent, T. A. Barlow, R. Cen, and J. P. Ostriker. The Observed Probability Distribution Function, Power Spectrum, and Correlation Function of the Transmitted Flux in the Lyα Forest. *ApJ*, 543:1–23, November 2000. doi: 10.1086/317079.

P. McDonald, U. Seljak, R. Cen, D. Shih, D. H. Weinberg, S. Burles, D. P. Schneider, D. J. Schlegel, N. A. Bahcall, J. W. Briggs, J. Brinkmann, M. Fukugita, Ž. Ivezić, S. Kent, and D. E. Vanden Berk. The Linear Theory Power Spectrum from the

Lyα Forest in the Sloan Digital Sky Survey. *ApJ*, 635:761–783, December 2005. doi: 10.1086/497563.

C. McGill. The redshift projection. II - Caustics and the Lyman alpha forest. *MNRAS*, 242:544–554, February 1990. doi: 10.1093/mnras/242.4.544.

A. Meiksin. The structure and evolution of Lyman-alpha forest clouds in the mini-halo model. *ApJ*, 431:109–122, August 1994. doi: 10.1086/174471.

A. L. Melott. Quasar L-alpha absorbers - Are precise conclusions possible. *ApJ*, 241:889–893, November 1980. doi: 10.1086/158402.

H. Menon, L. Wesolowski, G. Zheng, P. Jetley, L. Kale, T. Quinn, and F. Governato. Adaptive techniques for clustered N-body cosmological simulations. *Computational Astrophysics and Cosmology*, 2:1, March 2015. doi: 10.1186/s40668-015-0007-9.

P. Monaco, G. Murante, S. Borgani, and K. Dolag. Schmidt-Kennicutt relations in SPH simulations of disc galaxies with effective thermal feedback from supernovae. *MNRAS*, 421:2485–2497, April 2012. doi: 10.1111/j.1365-2966.2012.20482.x.

G. Murante, P. Monaco, M. Giovalli, S. Borgani, and A. Diaferio. A subresolution multiphase interstellar medium model of star formation and supernova energy feedback. *MNRAS*, 405:1491–1512, July 2010. doi: 10.1111/j.1365-2966.2010.16567.x.

G. Murante, P. Monaco, S. Borgani, L. Tornatore, K. Dolag, and D. Goz. Simulating realistic disc galaxies with a novel sub-resolution ISM model. *MNRAS*, 447:178–201, February 2015. doi: 10.1093/mnras/stu2400.

J. F. Navarro, C. S. Frenk, and S. D. M. White. The Structure of Cold Dark Matter Halos. *ApJ*, 462:563, May 1996. doi: 10.1086/177173.

D. B. Nestor, S. Rao, D. Turnshek, and E. Furst. Strong MgII Absorption Systems in QSOs from the Sloan Digital Sky Survey Early Data Release. In J. L. Rosenberg and M. E. Putman, editors, *The IGM/Galaxy Connection. The Distribution of Baryons at z=0*, volume 281 of *Astrophysics and Space Science Library*, page 133, April 2003.

A. Oemler, Jr. and C. R. Lynds. The absorption spectrum of 4C 25.05. *ApJ*, 199: 558–564, August 1975. doi: 10.1086/153724.

B. D. Oppenheimer and R. Davé. Cosmological simulations of intergalactic medium enrichment from galactic outflows. *MNRAS*, 373:1265–1292, December 2006. doi: 10.1111/j.1365-2966.2006.10989.x.

B. D. Oppenheimer and R. Davé. Mass, metal, and energy feedback in cosmological simulations. *MNRAS*, 387:577–600, June 2008. doi: 10.1111/j.1365-2966.2008.13280.x.

J. P. Ostriker and E. T. Vishniac. Generation of microwave background fluctuations from nonlinear perturbations at the ERA of galaxy formation. *ApJ*, 306:L51–L54, July 1986. doi: 10.1086/184704.

P. Padovani and F. Matteucci. Stellar Mass Loss in Elliptical Galaxies and the Fueling of Active Galactic Nuclei. *ApJ*, 416:26, October 1993. doi: 10.1086/173212.

A. A. Penzias and R. W. Wilson. A Measurement of Excess Antenna Temperature at 4080 Mc/s. *ApJ*, 142:419–421, July 1965. doi: 10.1086/148307.

C. Péroux, M. Dessauges-Zavadsky, S. D'Odorico, T.-S. Kim, and R. G. McMahon. A homogeneous sample of sub-damped Lyman α systems - II. Statistical, kinematic and chemical properties. *MNRAS*, 345:480–496, October 2003. doi: 10.1046/j.1365-8711.2003.06952.x.

P. Petitjean. QSO Absorption Line Systems. *ArXiv Astrophysics e-prints*, October 1998.

P. Petitjean, J. Bergeron, R. F. Carswell, and J. L. Puget. Detailed structure of expanding photoionized Ly-alpha clouds. *MNRAS*, 260:67–76, January 1993. doi: 10.1093/mnras/260.1.67.

M. Pettini, A. E. Shapley, C. C. Steidel, J.-G. Cuby, M. Dickinson, A. F. M. Moorwood, K. L. Adelberger, and M. Giavalisco. The Rest-Frame Optical Spectra of Lyman Break Galaxies: Star Formation, Extinction, Abundances, and Kinematics. *ApJ*, 554:981–1000, June 2001. doi: 10.1086/321403.

M. M. Pieri, J. Schaye, and A. Aguirre. The Spatial Distribution of Metals in the Intergalactic Medium. *ApJ*, 638:45–51, February 2006. doi: 10.1086/498738.

C. Porciani and P. Madau. The Origin of Intergalactic Metals around Lyman Break Galaxies. *ApJ*, 625:L43–L46, May 2005. doi: 10.1086/430779.

J. R. Pritchard, S. R. Furlanetto, and M. Kamionkowski. Galaxy surveys, inhomogeneous re-ionization and dark energy. *MNRAS*, 374:159–167, January 2007. doi: 10.1111/j.1365-2966.2006.11131.x.

J. X. Prochaska and A. M. Wolfe. On the Kinematics of the Damped Lyman-α Protogalaxies. *ApJ*, 487:73–95, September 1997.

J. X. Prochaska, S. Herbert-Fort, and A. M. Wolfe. The SDSS Damped Lyα Survey: Data Release 3. *ApJ*, 635:123–142, December 2005. doi: 10.1086/497287.

J. X. Prochaska, J. M. O'Meara, S. Herbert-Fort, S. Burles, G. E. Prochter, and R. A. Bernstein. Supersolar Super-Lyman Limit Systems. *ApJ*, 648:L97–L100, September 2006. doi: 10.1086/507867.

J. X. Prochaska, B. Weiner, H.-W. Chen, J. Mulchaey, and K. Cooksey. Probing the Intergalactic Medium/Galaxy Connection. V. On the Origin of Lyα and O VI Absorption at z $<$ 0.2. *ApJ*, 740:91, October 2011. doi: 10.1088/0004-637X/740/2/91.

J. X. Prochaska, M. W. Lau, and J. F. Hennawi. Quasars Probing Quasars. VII. The Pinnacle of the Cool Circumgalactic Medium Surrounds Massive z ˜ 2 Galaxies. *ApJ*, 796:140, December 2014. doi: 10.1088/0004-637X/796/2/140.

A. Rahmati, A. H. Pawlik, M. Raičević, and J. Schaye. On the evolution of the H I column density distribution in cosmological simulations. *MNRAS*, 430:2427–2445, April 2013. doi: 10.1093/mnras/stt066.

M. Rauch, R. F. Carswell, F. H. Chaffee, C. B. Foltz, J. K. Webb, R. J. Weymann, J. Bechtold, and R. F. Green. The Lyman forest of 0014 + 813. *ApJ*, 390:387–404, May 1992. doi: 10.1086/171290.

M. Rauch, W. L. W. Sargent, D. S. Womble, and T. A. Barlow. Temperature and Kinematics of C IV Absorption Systems. *ApJ*, 467:L5, August 1996. doi: 10.1086/310187.

M. Rauch, J. Miralda-Escudé, W. L. W. Sargent, T. A. Barlow, D. H. Weinberg, L. Hernquist, N. Katz, R. Cen, and J. P. Ostriker. The Opacity of the Lyα Forest and Implications for Ω_b and the Ionizing Background. *ApJ*, 489:7–20, November 1997. doi: 10.1086/304765.

M. Rauch, G. D. Becker, M. Viel, W. L. W. Sargent, A. Smette, R. A. Simcoe, T. A. Barlow, and M. G. Haehnelt. Expansion and Collapse in the Cosmic Web. *ApJ*, 632:58–80, October 2005. doi: 10.1086/432904.

M. J. Rees. Lyman absorption lines in quasar spectra - Evidence for gravitationally-confined gas in dark minihaloes. *MNRAS*, 218:25P–30P, January 1986. doi: 10.1093/mnras/218.1.25P.

M. Revnivtsev, M. Gilfanov, R. Sunyaev, K. Jahoda, and C. Markwardt. The spectrum of the cosmic X-ray background observed by RTXE/PCA. *A&A*, 411: 329–334, December 2003. doi: 10.1051/0004-6361:20031386.

K. H. R. Rubin, J. F. Hennawi, J. X. Prochaska, R. A. Simcoe, A. Myers, and M. W. Lau. Dissecting the Gaseous Halos of z $\sim$ Damped Lyα Systems with Close Quasar Pairs. *ApJ*, 808:38, July 2015. doi: 10.1088/0004-637X/808/1/38.

D. S. Rupke, S. Veilleux, and D. B. Sanders. Outflows in Infrared-Luminous Starbursts at z $<$ 0.5. I. Sample, Na I D Spectra, and Profile Fitting. *ApJS*, 160: 87–114, September 2005. doi: 10.1086/432886.

W. L. W. Sargent, P. J. Young, A. Boksenberg, and D. Tytler. The distribution of Lyman-alpha absorption lines in the spectra of six QSOs - Evidence for an intergalactic origin. *ApJS*, 42:41–81, January 1980. doi: 10.1086/190644.

B. D. Savage and K. R. Sembach. The analysis of apparent optical depth profiles for interstellar absorption lines. *ApJ*, 379:245–259, September 1991. doi: 10.1086/170498.

C. Scannapieco, M. Wadepuhl, O. H. Parry, J. F. Navarro, A. Jenkins, V. Springel, R. Teyssier, E. Carlson, H. M. P. Couchman, R. A. Crain, C. Dalla Vecchia, C. S. Frenk, C. Kobayashi, P. Monaco, G. Murante, T. Okamoto, T. Quinn, J. Schaye, G. S. Stinson, T. Theuns, J. Wadsley, S. D. M. White, and R. Woods. The Aquila comparison project: the effects of feedback and numerical methods on simulations of galaxy formation. *MNRAS*, 423:1726–1749, June 2012. doi: 10.1111/j.1365-2966.2012.20993.x.

E. Scannapieco, C. Pichon, B. Aracil, P. Petitjean, R. J. Thacker, D. Pogosyan, J. Bergeron, and H. M. P. Couchman. The sources of intergalactic metals. *MNRAS*, 365:615–637, January 2006. doi: 10.1111/j.1365-2966.2005.09753.x.

J. Schaye. Model-independent Insights into the Nature of the Lyα Forest and the Distribution of Matter in the Universe. *ApJ*, 559:507–515, October 2001. doi: 10.1086/322421.

J. Schaye, T. Theuns, A. Leonard, and G. Efstathiou. Measuring the equation of state of the intergalactic medium. *MNRAS*, 310:57–70, November 1999. doi: 10.1046/j.1365-8711.1999.02956.x.

J. Schaye, M. Rauch, W. L. W. Sargent, and T.-S. Kim. The Detection of Oxygen in the Low-Density Intergalactic Medium. *ApJ*, 541:L1–L4, September 2000. doi: 10.1086/312892.

J. Schaye, A. Aguirre, T.-S. Kim, T. Theuns, M. Rauch, and W. L. W. Sargent. Metallicity of the Intergalactic Medium Using Pixel Statistics. II. The Distribution of Metals as Traced by C IV. *ApJ*, 596:768–796, October 2003. doi: 10.1086/378044.

J. Schaye, C. Dalla Vecchia, C. M. Booth, R. P. C. Wiersma, T. Theuns, M. R. Haas, S. Bertone, A. R. Duffy, I. G. McCarthy, and F. van de Voort. The physics driving the cosmic star formation history. *MNRAS*, 402:1536–1560, March 2010. doi: 10.1111/j.1365-2966.2009.16029.x.

M. Schmidt. The Rate of Star Formation. *ApJ*, 129:243, March 1959. doi: 10.1086/146614.

M. Schmidt. Large Redshifts of Five Quasi-Stellar Sources. *ApJ*, 141:1295, April 1965. doi: 10.1086/148217.

U. Seljak, A. Makarov, P. McDonald, S. F. Anderson, N. A. Bahcall, J. Brinkmann, S. Burles, R. Cen, M. Doi, J. E. Gunn, Ž. Ivezić, S. Kent, J. Loveday, R. H. Lupton, J. A. Munn, R. C. Nichol, J. P. Ostriker, D. J. Schlegel, D. P. Schneider, M. Tegmark, D. E. Berk, D. H. Weinberg, and D. G. York. Cosmological parameter analysis including SDSS Lyα forest and galaxy bias: Constraints on the primordial spectrum of fluctuations, neutrino mass, and dark energy. *Phys. Rev. D*, 71(10):103515, May 2005. doi: 10.1103/PhysRevD.71.103515.

K. R. Sembach and B. D. Savage. Observations of highly ionized gas in the Galactic halo. *ApJS*, 83:147–201, November 1992. doi: 10.1086/191734.

A. E. Shapley, C. C. Steidel, M. Pettini, and K. L. Adelberger. Rest-Frame Ultraviolet Spectra of z$\sim$3 Lyman Break Galaxies. *ApJ*, 588:65–89, May 2003. doi: 10.1086/373922.

D. Sijacki and V. Springel. Hydrodynamical simulations of cluster formation with central AGN heating. *MNRAS*, 366:397–416, February 2006. doi: 10.1111/j.1365-2966.2005.09860.x.

R. A. Simcoe, W. L. W. Sargent, and M. Rauch. The Distribution of Metallicity in the Intergalactic Medium at z∼2.5: O VI and C IV Absorption in the Spectra of Seven QSOs. *ApJ*, 606:92–115, May 2004. doi: 10.1086/382777.

A. Slosar, V. Iršič, D. Kirkby, S. Bailey, N. G. Busca, T. Delubac, J. Rich, É. Aubourg, J. E. Bautista, V. Bhardwaj, M. Blomqvist, A. S. Bolton, J. Bovy, J. Brownstein, B. Carithers, R. A. C. Croft, K. S. Dawson, A. Font-Ribera, J.-M. Le Goff, S. Ho, K. Honscheid, K.-G. Lee, D. Margala, P. McDonald, B. Medolin, J. Miralda-Escudé, A. D. Myers, R. C. Nichol, P. Noterdaeme, N. Palanque-Delabrouille, I. Pâris, P. Petitjean, M. M. Pieri, Y. Piškur, N. A. Roe, N. P. Ross, G. Rossi, D. J. Schlegel, D. P. Schneider, N. Suzuki, E. S. Sheldon, U. Seljak, M. Viel, D. H. Weinberg, and C. Yèche. Measurement of baryon acoustic oscillations in the Lyman-α forest fluctuations in BOSS data release 9. *J. Cosmology Astropart. Phys.*, 4:026, April 2013. doi: 10.1088/1475-7516/2013/04/026.

A. Songaila. The Redshift Evolution of the Metagalactic Ionizing Flux Inferred from Metal Line Ratios in the Lyman Forest. *AJ*, 115:2184–2205, June 1998. doi: 10.1086/300387.

V. Springel. The cosmological simulation code GADGET-2. *MNRAS*, 364:1105–1134, December 2005. doi: 10.1111/j.1365-2966.2005.09655.x.

V. Springel. E pur si muove: Galilean-invariant cosmological hydrodynamical simulations on a moving mesh. *MNRAS*, 401:791–851, January 2010. doi: 10.1111/j.1365-2966.2009.15715.x.

V. Springel and L. Hernquist. Cosmological smoothed particle hydrodynamics simulations: a hybrid multiphase model for star formation. *MNRAS*, 339:289–311, February 2003. doi: 10.1046/j.1365-8711.2003.06206.x.

V. Springel, S. D. M. White, G. Tormen, and G. Kauffmann. Populating a cluster of galaxies - I. Results at [formmu2]z=0. *MNRAS*, 328:726–750, December 2001. doi: 10.1046/j.1365-8711.2001.04912.x.

V. Springel, T. Di Matteo, and L. Hernquist. Black Holes in Galaxy Mergers: The Formation of Red Elliptical Galaxies. *ApJ*, 620:L79–L82, February 2005. doi: 10.1086/428772.

V. Springel, J. Wang, M. Vogelsberger, A. Ludlow, A. Jenkins, A. Helmi, J. F. Navarro, C. S. Frenk, and S. D. M. White. The Aquarius Project: the subhaloes of galactic haloes. *MNRAS*, 391:1685–1711, December 2008. doi: 10.1111/j.1365-2966.2008.14066.x.

C. C. Steidel and M. Dickinson. The unusual field of the quasar 3C 336 - Identification of three foreground MG II absorbing galaxies. *ApJ*, 394:81–86, July 1992. doi: 10.1086/171560.

C. C. Steidel, D. K. Erb, A. E. Shapley, M. Pettini, N. Reddy, M. Bogosavljević, G. C. Rudie, and O. Rakic. The Structure and Kinematics of the Circumgalactic Medium from Far-ultraviolet Spectra of z ˜= 2-3 Galaxies. *ApJ*, 717:289–322, July 2010. doi: 10.1088/0004-637X/717/1/289.

R. Teyssier. RAMSES: A new N-body and hydrodynamical code. Astrophysics Source Code Library, November 2010.

R. Teyssier, B. Moore, D. Martizzi, Y. Dubois, and L. Mayer. Mass distribution in galaxy clusters: the role of Active Galactic Nuclei feedback. *MNRAS*, 414: 195–208, June 2011. doi: 10.1111/j.1365-2966.2011.18399.x.

T. Theuns, A. Leonard, G. Efstathiou, F. R. Pearce, and P. A. Thomas. Pˆ3M-SPH simulations of the Lyalpha forest. *MNRAS*, 301:478–502, December 1998. doi: 10.1046/j.1365-8711.1998.02040.x.

T. Theuns, A. Chalk, M. Schaller, and P. Gonnet. SWIFT: task-based hydrodynamics and gravity for cosmological simulations. *ArXiv e-prints*, August 2015.

F.-K. Thielemann, D. Argast, F. Brachwitz, W. R. Hix, P. Höflich, M. Liebendörfer, G. Martinez-Pinedo, A. Mezzacappa, I. Panov, and T. Rauscher. Nuclear cross sections, nuclear structure and stellar nucleosynthesis. *Nuclear Physics A*, 718: 139–146, May 2003. doi: 10.1016/S0375-9474(03)00704-8.

A. A. Thoul and D. H. Weinberg. Hydrodynamic Simulations of Galaxy Formation. II. Photoionization and the Formation of Low-Mass Galaxies. *ApJ*, 465:608, July 1996. doi: 10.1086/177446.

G. Tormen. The rise and fall of satellites in galaxy clusters. *MNRAS*, 290:411–421, September 1997. doi: 10.1093/mnras/290.3.411.

L. Tornatore, S. Borgani, K. Dolag, and F. Matteucci. Chemical enrichment of galaxy clusters from hydrodynamical simulations. *MNRAS*, 382:1050–1072, December 2007. doi: 10.1111/j.1365-2966.2007.12070.x.

C. A. Tremonti, T. M. Heckman, G. Kauffmann, J. Brinchmann, S. Charlot, S. D. M. White, M. Seibert, E. W. Peng, D. J. Schlegel, A. Uomoto, M. Fukugita, and J. Brinkmann. The Origin of the Mass-Metallicity Relation: Insights from 53,000 Star-forming Galaxies in the Sloan Digital Sky Survey. *ApJ*, 613:898–913, October 2004. doi: 10.1086/423264.

J. Tumlinson, C. Thom, J. K. Werk, J. X. Prochaska, T. M. Tripp, D. H. Weinberg, M. S. Peeples, J. M. O'Meara, B. D. Oppenheimer, J. D. Meiring, N. S. Katz, R. Davé, A. B. Ford, and K. R. Sembach. The Large, Oxygen-Rich Halos of Star-Forming Galaxies Are a Major Reservoir of Galactic Metals. *Science*, 334: 948, November 2011. doi: 10.1126/science.1209840.

M. L. Turner, J. Schaye, C. C. Steidel, G. C. Rudie, and A. L. Strom. Metal-line absorption around z $\approx$ 2.4 star-forming galaxies in the Keck Baryonic Structure Survey. *MNRAS*, 445:794–822, November 2014. doi: 10.1093/mnras/stu1801.

D. Tytler. The distribution of QSO absorption system column densities - Evidence for a single population. *ApJ*, 321:49–68, October 1987. doi: 10.1086/165615.

D. Tytler, X.-M. Fan, S. Burles, L. Cottrell, C. Davis, D. Kirkman, and L. Zuo. Ionization and Abundances of Intergalactic Gas. In G. Meylan, editor, *QSO Absorption Lines*, page 289, 1995.

L. B. van den Hoek and M. A. T. Groenewegen. New theoretical yields of intermediate mass stars. *A&AS*, 123, June 1997. doi: 10.1051/aas:1997162.

A. Vecchi, S. Molendi, M. Guainazzi, F. Fiore, and A. N. Parmar. The BeppoSAX 1-8 keV cosmic background spectrum. *A&A*, 349:L73–L76, September 1999.

M. Viel, J. Lesgourgues, M. G. Haehnelt, S. Matarrese, and A. Riotto. Constraining warm dark matter candidates including sterile neutrinos and light gravitinos with WMAP and the Lyman-α forest. *Phys. Rev. D*, 71(6):063534, March 2005. doi: 10.1103/PhysRevD.71.063534.

M. Viel, J. S. Bolton, and M. G. Haehnelt. Cosmological and astrophysical constraints from the Lyman α forest flux probability distribution function. *MNRAS*, 399:L39–L43, October 2009. doi: 10.1111/j.1745-3933.2009.00720.x.

M. Viel, G. D. Becker, J. S. Bolton, and M. G. Haehnelt. Warm dark matter as a solution to the small scale crisis: New constraints from high redshift Lyman-α forest data. *Phys. Rev. D*, 88(4):043502, August 2013. doi: 10.1103/PhysRevD.88.043502.

J. W. Wadsley, J. Stadel, and T. Quinn. Gasoline: a flexible, parallel implementation of TreeSPH. *New Astron.*, 9:137–158, February 2004. doi: 10.1016/j.newast.2003.08.004.

B. Wang. Ly-alpha forests and cooling outflow from dwarf galaxies. *ApJ*, 444: L17–L20, May 1995. doi: 10.1086/187849.

R. S. Warwick and T. P. Roberts. The extragalactic X-ray background at 0.25 keV. *Astronomische Nachrichten*, 319:59, 1998. doi: 10.1002/asna.2123190126.

J. K. Webb. Clustering of LYα Absorbing Clouds at High Redshift /. In A. Hewitt, G. Burbidge, and L. Z. Fang, editors, *Observational Cosmology*, volume 124 of *IAU Symposium*, page 803, 1987.

J. C. Weisheit. On the use of line shapes in the analysis of QSO absorption spectra. *ApJ*, 219:829–835, February 1978. doi: 10.1086/155844.

J. K. Werk, J. X. Prochaska, C. Thom, J. Tumlinson, T. M. Tripp, J. M. O'Meara, and M. S. Peeples. The COS-Halos Survey: An Empirical Description of Metal-line Absorption in the Low-redshift Circumgalactic Medium. *ApJS*, 204:17, February 2013. doi: 10.1088/0067-0049/204/2/17.

M. Wetzstein, A. F. Nelson, T. Naab, and A. Burkert. Vine - A Numerical Code for Simulating Astrophysical Systems Using Particles. I. Description of the Physics and the Numerical Methods. *ApJS*, 184:298–325, October 2009. doi: 10.1088/0067-0049/184/2/298.

R. J. Weymann, R. F. Carswell, and M. G. Smith. Absorption lines in the spectra of quasistellar objects. *ARA&A*, 19:41–76, 1981. doi: 10.1146/annurev.aa.19.090181.000353.

R. J. Weymann, B. T. Jannuzi, L. Lu, J. N. Bahcall, J. Bergeron, A. Boksenberg, G. F. Hartig, S. Kirhakos, W. L. W. Sargent, B. D. Savage, D. P. Schneider, D. A. Turnshek, and A. M. Wolfe. The Hubble Space Telescope Quasar Absorption Line Key Project. XIV. The Evolution of Lyα Absorption Lines in the Redshift Interval z = 0-1.5. *ApJ*, 506:1–18, October 1998. doi: 10.1086/306233.

R. P. C. Wiersma, J. Schaye, T. Theuns, C. Dalla Vecchia, and L. Tornatore. Chemical enrichment in cosmological, smoothed particle hydrodynamics simulations. *MNRAS*, 399:574–600, October 2009. doi: 10.1111/j.1365-2966.2009.15331.x.

G. M. Williger, R. F. Carswell, R. J. Weymann, E. B. Jenkins, K. R. Sembach, T. M. Tripp, R. Davé, L. Haberzettl, and S. R. Heap. The low-redshift Lyα forest towards 3C 273. *MNRAS*, 405:1736–1758, July 2010. doi: 10.1111/j.1365-2966.2010.16519.x.

A. M. Wolfe, D. A. Turnshek, H. E. Smith, and R. D. Cohen. Damped Lyman-alpha absorption by disk galaxies with large redshifts. I - The Lick survey. *ApJS*, 61: 249–304, June 1986. doi: 10.1086/191114.

S. E. Woosley and T. A. Weaver. The Evolution and Explosion of Massive Stars. II. Explosive Hydrodynamics and Nucleosynthesis. *ApJS*, 101:181, November 1995. doi: 10.1086/192237.

J. S. B. Wyithe and M. Dijkstra. Non-gravitational contributions to the clustering of Lyα selected galaxies: implications for cosmological surveys. *MNRAS*, 415: 3929–3950, August 2011. doi: 10.1111/j.1365-2966.2011.19007.x.

P. J. Young, W. L. W. Sargent, A. Boksenberg, R. F. Carswell, and J. A. J. Whelan. A high-resolution study of the absorption spectrum of PKS 2126-158. *ApJ*, 229: 891–908, May 1979. doi: 10.1086/157024.

J. Zavala, T. Okamoto, and C. S. Frenk. Bulges versus discs: the evolution of angular momentum in cosmological simulations of galaxy formation. *MNRAS*, 387:364–370, June 2008. doi: 10.1111/j.1365-2966.2008.13243.x.